1-1-2011

Synthesis and characterization of metal chalcogenide nanostructured materials for thermoelectric applications

Shreyashi Ganguly
Wayne State University,

SYNTHESIS AND CHARACTERIZATION OF METAL CHALCOGENIDE NANOSTRUCTURED MATERIALS FOR THERMOELECTRIC APPLICATIONS

by

SHREYASHI GANGULY

DISSERTATION

Submitted to the Graduate School

of Wayne State University,

Detroit, Michigan

in partial fulfillment of the requirements

for the degree of

DOCTOR OF PHILOSOPHY

2012

MAJOR: CHEMISTRY (Inorganic)

Approved by:

_____ _____

Advisor Date

_____

_____

_____

_____

DEDICATION

To my beloved parents and my family

ACKNOWLEDGEMENTS

First, I would like to thank my advisor Prof. Stephanie L. Brock for her immense support and encouragement throughout my graduate studies. I feel proud to be a part of her research group, and have learnt a lot working under her guidance. Her "never give up" attitude and excellent time management skill inspire me and has left a huge impression in my mind. She has always given me valuable advice, not only on scientific front but also on my future career prospects. I would like to thank her for patiently reading my documents over the years and for her training to improve my writing skills. I would also like to thank her for all the birthday cakes, Christmas gifts, group outings and parties. I cannot express my gratitude towards her in words as I respect her a lot and look up to her for many things. At the end, I would like to say just a big "THANK YOU" for everything.

I take this opportunity to thank my committee members Dr. Claudio N. Verani, Dr. Louis J. Romano and Dr. Guangzhao Mao for their valuable time and suggestions. They have always been very helpful, and have carved out time for me whenever I needed it the most.

I would like to thank my collaborators Dr. Donald Morelli, and Dr. Jeff Sakamoto from Michigan State University and Dr. Ctirad Uher from University of Michigan, for their valuable discussions throughout my graduate studies. They are friendly and kind hearted people who have listened to me patiently and respected my suggestions. I would like to thank them for giving me an opportunity to work in their lab and use their instruments during my graduate studies. I would like to specially thank Dr. Chen (Kevin) Zhou, student of Dr. Morelli, for being such a nice and helpful person. Irrespective of the time, he was always there to answer my queries and help me out in each and every way possible. I would also like to thank Sarah and Guo, students of Dr. Uher for their help and support.

I would like to thank the central instrumentation facility (CIF) staff members of Wayne State University, Dr. Yi Liu and Dr. Zhi Mei (Mike) for their constant help with TEM, and Dr. Mary Jane Heeg for her help with powder X-ray diffraction experiments. Without their help and support my graduate study would not have been complete.

I would like to thank the official staff of the Chemistry department, Sharon Kelly, Melissa Barton, Mary Wood, Diane Klimas, Erin Bachert, Debbie McCreless and Bernie Meisik. They are the most efficient and sweetest staff members I have ever come across. I would also like to thank Nestor, technical staff member, a computer expert in our department for being such a help.

I want to thank Dr. Kennedy K. Kalebaila, who trained me initially and made me comfortable in the lab. I would like to thank Dr. Keerthi Senevirathne for his valuable discussions on science and life in general. I would also like to thank Dr. Susanthri C. Perera, Dr. Jaya L. Mohanan and Dr. Indika Arachchige, previous Brock group members for helping me out in various occasions. I also had great fun in the lab with Dr. Elayaraja Muthuswamy and Dr. Qinghong Yao. I had a great time with Irina Pala. She has a very lively personality, and I will cherish all the moments we have spent together, and hopefully more to come.

I had a great time working with all my labmates- Layan Savithra, Yanhua Zhang, Lasantha Korala, Asha Bandara, Derak James and Roshini Pimmachcharige. The funny discussions in the lab always bring a smile on my face. Thank you Asha for everything and you are a very sweet and helpful girl and I have enjoyed talking with you a lot. All of you guys are brilliant chemists and I wish each one of you all the best for your future endeavors. Thank you for everything. I would also like to welcome the new members of the Brock group Ruchira and Jessica. This is the place to be.

I would like to take this opportunity to thank all my friends at Wayne State who have made my stay in Detroit enjoyable especially Dr. Madhura Chakrabarti for being the friend you always be, Dr. Sandhya Muralidharan for all the good food and enjoyment, Myriame, Selma, Dr. Indrajeet, Dr. Kashinath, Dr. Sardar, Dr. Sujit, Dr. Pragna, Dr. Bibhuti, Dr. Sangeeta and Raj for all your time. In addition, I would also like to thank all the Indian community people, my singing and choreography group for making my stress go away. I would also like to thank Verani group members, for being such a help whenever I needed.

Finally, I would like to thank my parents and my family for their immense trust on me. Despite their challenges, they have always helped and supported me to achieve my dreams. Ma, Baba, Jethun, Mani, my brothers and Jiju for all your prayers and blessings. A big thanks to my sister Sulagna Ganguly, for sending me here for my higher studies. Words are not sufficient to thank them, so I simply bow my head in front of them. I would like to thank Jai Prakash, for his love and support over the years. He is my friend, philosopher and guide, my pillar of strength and has always been by my side through the tough times and constantly encouraged me to do my best in any situation, whether it is related to academic or extracurricular activities. Last but most importantly, I would like thank the almighty god for giving me good health and blessings throughout the graduate life.

TABLE OF CONTENTS

LIST OF TABLES

LIST OF FIGURES

List of Abbreviations

PGEC	Phonon glass electron crystal concept
RTG	Radioisotope thermoelectric generators
VB	Valence band
CB	Conduction band
LUMO	Lowest unoccupied molecular orbital
HOMO	Highest occupied molecular orbital
ZT	Figure of merit
MBE	Molecular beam epitaxy
LED	Light emitting diodes
AOT	Sodium bis (2-ethylhexyl) sulfosuccinate
PXRD	Powder x-ray diffraction
TEM	Transmission electron microscopy
HRTEM	High resolution transmission electron microscopy
IR	Infrared spectroscopy
EDS	Energy dispersive spectroscopy
TGA	Thermogravimetric analysis
DSC	Differential scanning Calorimetry
CPD	Critical point dryer
ICDD	International center for diffraction database
PDF	Powder diffraction files
SAED	Selected area electron diffraction
STP	Standard temperature and pressure
BET	Brunauer Emmett and Teller
BJH	Barett Joyner and Halenda

OA	Oleic acid
ODE	1-Octadecene
$Pb(OAc)_2$	Lead acetate
4-FPhSH	4-Flurothiophenol
1-DDT	1-Dodecanethiol
TNM	Tetranitromethane
TOP	Trioctylphosphine
TOPTe	Trioctylphosphine telluride
TEA	Triethylamine
AC	Alternating current
DC	Direct current
S	Seebeck coefficient
σ	Electrical conductivity
κ	Total thermal conductivity
κ_e	Electronic thermal conductivity
κ_l	Lattice thermal conductivity
T	Absolute temperature
ZT	Figure of merit
n	Carrier concentration
e	Electronic charge
E_g	Band gap
E_f	Energy of Fermi level
L	Lorenz number

Chapter 1

Introduction

The revolutionary idea of exploiting quantum confinement effects by attenuating the size of bulk materials to nanoscale dimensions has led to a new era of materials for applications such as photovoltaics, sensing, light emitting diodes (LEDs) and thermoelectrics. However, efficient ways of assembling nanoparticles into functional devices remains an unfulfilled need. One important area where the development of nanostructures has become important is in the creation of improved thermoelectric materials. Accordingly, the goal of this dissertation study is to create nanostructures of materials that in bulk form are good thermoelectric materials, with the help of sol-gel assembly as well as nanocomposite formation, and evaluate their thermoelectric properties. This Chapter will describe background information on thermoelectrics; and the advantages of semiconductor nanocrystals for such applications, followed by a summary of nanoparticle assembly methods with an emphasis on sol-gel methodology. The properties of thermoelectrically-relevant lead and bismuth chalcogenide nanoparticles, especially PbTe and Bi_2Te_3, along with their synthesis and applications will be covered. Finally, the thesis statement and an outline of the dissertation will be presented.

1.1 Thermoelectrics

As the world population increases, the demand for energy increases. It is predicted that our regular sources of energy, fossil fuels, natural gas and coal, are going to be exhausted in the next few generations.[1, 2] Moreover, these energy sources are detrimental to our environment. Thus, the need for renewable and greener energy sources has become a matter of urgency. One of the greener technologies that has received considerable attention over the past ten years is

thermoelectric energy conversion. Thermoelectric materials (TE) are those that can convert heat into electricity and vice versa.[2]

1.1.1 Seebeck and Peltier Effects

The Seebeck and Peltier effects are the central concepts behind thermoelectrics. When two dissimilar materials are joined in a circuit and their points of contact are at different temperatures, a voltage difference develops across the junction. The ratio of the voltage difference (ΔV) to the temperature difference (ΔT) is called the Seebeck coefficient, S or the thermopower, as given by equation (1.1).[3, 4]

$$S = \frac{\Delta V}{\Delta T} \qquad (1.1)$$

This effect was observed by Thomas Johann Seebeck in the early 1800's and hence was termed the Seebeck effect. The sign of S (negative or positive) reflects the majority charge carriers in the system. If S is negative, the majority charge carriers are electrons, characteristic of n-type doped materials; whereas if S is positive, the majority charge carriers are holes, characteristic of p-type doped materials. The value of S is an intrinsic property of a material. Generally, semiconductors show high Seebeck coefficients relative to metals. In semiconductors, both the concentration of free charge carriers and their kinetic energies are dependent on temperature. When a temperature gradient is applied across a semiconductor, the carrier concentration as well as the velocity of charge carriers at the hot end becomes higher relative to the cold end. This results in diffusion of charge carriers from the hot end to the cold end, leading to build up of potential difference across the two ends of the semiconductor. The value of S in semiconductors can be in hundreds of μV/degree. However for metals, the concentration and kinetic energy of free charge carriers remain constant over a broad range of temperature, leading

to minimal diffusion of charge carriers across the metals on application of a temperature gradient. This causes negligible build up of potential difference and hence low values of S, typically a few μV/degree.[3]

Around 1834, Jean Peltier, a watchmaker, found that when a current (I) is passed through two dissimilar materials at a constant temperature, heat is either generated or absorbed (depending upon the direction of flow of I), at the junction of the materials. This effect is called Peltier effect and is given by equation (1.2).[3]

$$Q = \Pi \times I \qquad (1.2)$$

where, Q is the rate of flow of heat and Π is the Peltier coefficient. The Peltier and Seebeck coefficients are related to each other by equation (1.3).[3]

$$\Pi = S \times T \qquad (1.3)$$

where, T is the absolute temperature.

1.1.2 Applications and Efficiency of TE Materials

Compared to traditional cooling and power generation systems, TE devices have several advantages. They are highly reliable, with a long lifetime; they are noise free, causing no noise pollution; they require no moving mechanical parts as they use electrons and holes as charge carriers for their performance; and most importantly, they are environmental friendly as they use no toxic gases.[2, 5] **Figure 1.1** shows a TE module consisting of both p- and n- doped semiconductor material connected through wires. The same module is used for both power generation and refrigeration.[1] When a current is passed through the TE module, a temperature gradient develops and heat is absorbed onto the cold side and rejected at the heat sink; achieving

refrigeration mode; whereas, when temperature gradient is applied across the same TE module, a voltage develops, which generates current across the device and thus directly converts heat into electricity. TE devices are being utilized in several applications, such as radioisotope thermoelectric generators (RTGs) for space probes, where heat generated from radioisotope decay (usually plutonium-238) is converted into electricity via a TE generator. Considerable effort has been employed by the automotive industry to convert heat dissipated from vehicles into useful electrical energy via TE generators, but these studies are still in their infancy. TE devices have been used for heating and cooling the seats of cars.[1, 6] Despite several advantages of TE devices, they have only been applied to niche applications and are not widespread. The problem lies in the fact that the efficiency of the TE devices is relatively low as compared to the commercially available refrigerators and power generators.[2]

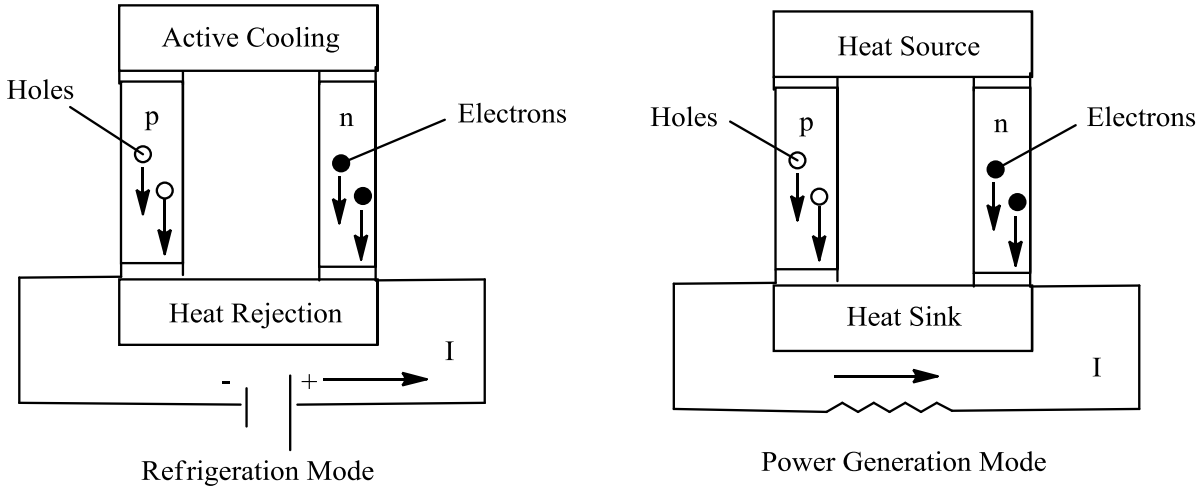

Figure 1.1 Diagram of p- and n- doped material joined in circuit. The same material could be used for both power generation and also for refrigeration, adapted from literature.[1]

The efficiency of a thermoelectric material is given by its *figure of merit* ZT, a dimensionless unit. ZT depends on several factors (equation (1.4)) Seebeck coefficient S, electrical conductivity σ, thermal conductivity κ and the absolute temperature T.[4]

$$ZT = \frac{S^2\sigma}{\kappa}T \qquad (1.4)$$

In order to have high ZT, the $S^2\sigma$ term, also called the power factor, should be high, and at the same time, the κ term should be low. However, the parameters S, σ and κ are highly correlated and it is a challenge to individually alter one parameter without impacting the others. The Seebeck coefficient, S, depends on the carrier concentration of the material, n, which in turn is associated with electrical conductivity, σ, as depicted in equations 1.5 and 1.6,[5] where, K_B = Boltzmann constant, e = electronic charge, h = Planck's constant, m* = effective mass of the carrier, T = absolute temperature, n = carrier concentration and μ = carrier mobility. On the other hand, the total thermal conductivity (κ) term in equation 1.4 consists of the electronic contribution, κ_e, as well as the lattice contribution, κ_l, giving $\kappa = \kappa_e + \kappa_l$. The electronic thermal conductivity, κ_e, is associated with the heat conduction through electrons whereas the lattice thermal conductivity, κ_l, is associated with heat conduction through quantized lattice vibrations, called phonons.

$$S = \frac{8\pi^2 K_B^2}{3eh^2}\, m^* T\left(\frac{\pi}{3n}\right)^{\frac{2}{3}} \qquad (1.5)$$

$$\sigma = ne\mu \qquad (1.6)$$

The efficiency, η, of a power generator operating at two different temperatures, T_h and T_c (hot and cold side, respectively), depends on the figure of merit, ZT, as shown in equation (1.7),[1] where T_m is equal to $(T_h + T_c)/2$.

$$\eta = \frac{\Delta T}{T_h}\left[\frac{\sqrt{1+ZT_m}-1}{\sqrt{1+ZT_m}+\frac{T_c}{T_h}}\right] \qquad (1.7)$$

Thus, η is proportional to $(1+ZT_m)^{1/2}$, and only if ZT has a very high value, can it approach the efficiency of Carnot engines, which is $\Delta T/T_h$. As mentioned before it is a challenge to individually alter the parameters (S, σ and κ), thus the materials of choice for TE are limited. Metals have high σ but also have high κ, whereas glasses have low κ but also have low σ. Up until now, the best TE materials have been found to be doped semiconductors with high charge carrier concentrations (the optimized value of n lies between 10^{19} to 10^{21} carriers/cm^3).[5] These materials show enhanced σ due to the presence of high carrier concentrations, and at the same time low κ_l due to scattering of heat carrying phonons by the dopants (discussed in detail in later sections), enhancing the overall ZT of the material. Additionally, κ_l can be further reduced by using high atomic weight elements like Bi, Te, Pb, which cause reduced lattice vibrations.[7] In my dissertation research, PbTe and Bi_2Te_3 phases were specifically targeted as they show excellent ZT values in the bulk form and find use in a range of devices for niche products.[1] For example, bulk Bi_2Te_3 achieves ZT ≈ 1 at 320 K (S = 225 μV/K, ρ = 1 mΩ·m and κ = 1.5 W/ (m·K)) for an optimized carrier concentration of n = 10^{19} cm^{-3},[8] and bulk PbTe acheives a ZT of 0.4 at 300 K (S = 265 μV/K, ρ = 0.0037 mΩ·m and κ = 2.0 W/ (m·K)) for n = 10^{19} cm^{-3}. However, in order to use TE materials as cost-effective alternative energy sources, ZT should be close to or higher than 3.[9]

1.1.3 Principles Underlying Enhancement of ZT for Materials

There are several approaches that have been suggested for enhancing the ZT of a material. As discussed in the previous section, metals and glasses are not ideal choices for TE applications but each had aspects that are ideal. Glen Slack,[10] came up with a new concept for materials that can

be used in TE, termed as the phonon glass-electron crystal concept (PGEC), which suggests that the lattice thermal conductivity of a material could be reduced if the material acts like glass (amorphous), resulting in large phonon scattering, and at the same time, acts like a crystal, minimizing the electron scattering and thus leading to enhanced electrical conductivity.

The effect of electron and phonon scattering on ZT can be explained by taking into account the wavelength (λ) and mean free path length (l) associated with the transport of electrons (or holes) and phonons.[3, 7] Though both electrons and phonons are scattered by all lattice distortions in the crystal, they scatter to different extents. This difference in the degree of scattering for electrons and phonons arises due to the difference in their wavelengths. Electrons have longer wavelengths whereas phonons consists of a spectrum of wavelengths varying from short to mid to long.[3] Due to the longer wavelength of electrons relative to the phonons, the electrons are scattered to a very small degree on defects due to distortions of atomic distances whereas short wavelength phonons are easily scattered by all such lattice distortions. The mid to long wavelength phonons are scattered only when λ_{ph}, the phonon mean free path, is between $1 \leq \lambda_{ph} \leq 100$ nm.[3] The scattering of heat carrying phonons leads to reduction in κ_l, whereas the lower degree of scattering of electrons enables large electrical conductivities, which in turn increase the power factor in PGEC materials. Examples of PGEC materials includes those having crystalline cage-like structures or voids that can be partially or completely filled by guest atoms, also called "rattlers", that act as phonon scattering centers leading to enhanced ZT.[1, 11] These include the skutterudites ($CoAs_3$-type), which have a linked octahedron cage-like structures with vacancies that can be completely or partially filled with atoms.[11] Sales et al., have reported ZT of 1.0 at 800 K for filled skutterudite materials like $CeFe_{4-x}Co_xSb_{12}$ and $LaFe_{4-x}Co_xSb_{12}$, and predicted that with proper optimization of carrier concentration, the ZT of these materials could reach a value

of 1.4.[12] Subramanian and coworkers[13] have prepared $CoSb_3$ partially filled with indium, where they have observed a ZT of 1.2 at 525 K. Another class of materials that exploits the PGEC model are the clatharates, which are periodic solids of tetrahedrally bonded atoms (like Ge, Si or Sn) forming cage like structures that again allows filling with "rattlers" leading to reduction in κ_l.[1] For example, Saramat and coworkers[14] have observed a record high ZT value of ~ 1.35 at 900 K for crystals of $Ba_8Ga_{16}Ge_{30}$ (as compared to other clatharates in the literature),[15] due to low values of lattice thermal conductivity (0.12 W/(cm·K) at 900 K) attributed to Ba^{2+} rattlers, but without much alteration in electronic properties. Unfortunately, the PGEC model is unlikely to produce ZT's greater than 3.

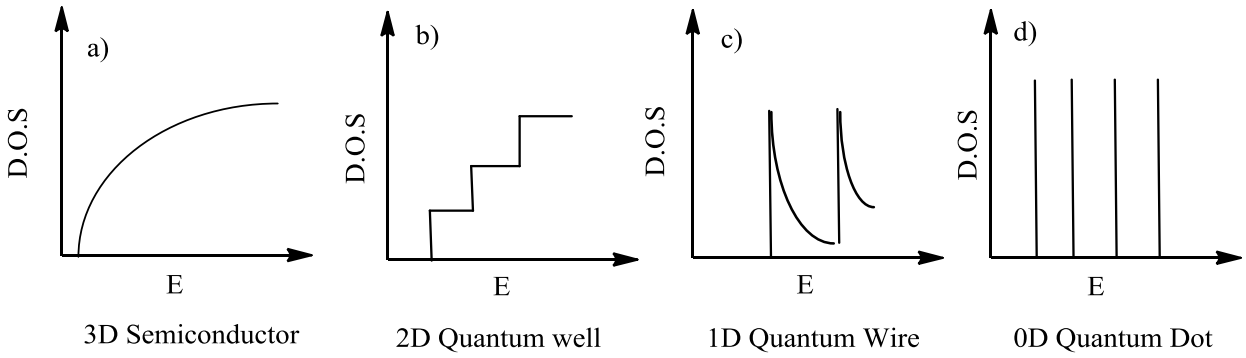

Figure 1.2 Electronic density of states versus energy plot depicting a) 3D semiconductors, b) 2D quantum well, c) 1D quantum wire, and d) 0D quantum dot; adapted from the literature.[2]

A major breakthrough came when Dresselhaus and coworkers suggested that the ZT of a material could be improved by nanostructuring.[2] There are two contributing factors that help improve ZT in nanostructures. First, quantum confinement effects (discussed in section 1.2) in nanostructured materials leads to the formation of discrete energy levels (**Figure 1.2**), resulting in increased density of states (DOS) at the Fermi level. The increased DOS near the Fermi level implies more energy states available for electrons to reside near the Fermi level, hence

facilitating the carrier transport for conduction and resulting in increased thermoelectric power factor, ($S^2\sigma$), and thus ZT of the material. Secondly, the presence of interfaces in the nanostructures can serve as scattering centers for heat carrying phonons, decreasing the thermal conductivity of the system, resulting in enhanced ZT.[2, 16, 17]

1.2 Semiconductor Nanocrystals

As mentioned previously, the materials used thus far that show enhanced ZT are semiconductors because they possess unique properties. In a bulk semiconductor, the energy levels form a continuum or "band" due to the overlap of orbitals from the large number of constituent atoms. The higher energy levels occupied by electrons are represented as the valence band (VB) whereas the empty, or lowest unoccupied, energy levels are denoted as the conduction band (CB). The energy difference between the top of the VB and the bottom of the CB is called the band gap energy (E_g) as shown in **Figure 1.3**.[18] This E_g can be considered conceptually similar to the HOMO (highest occupied molecular orbital) and LUMO (lowest unoccupied molecular orbital) gap of individual molecules. At absolute zero (0 K), the highest filled energy level is known as the Fermi level and the energy associated with it is called the Fermi energy, E_f.[19] In metals, the VB and CB overlap, resulting in no energy gap. At temperatures above 0 K, the electrons occupying energy levels near E_f have sufficient thermal energy to move to the empty energy levels above E_f. As a result, some energy levels above E_f are occupied while some below E_f are vacant. This enables the electrons near E_f to move freely and hence, show high electrical conductivity. On the other hand, for the case of insulators, the VB is full but is separated from the CB by a large band gap (E_g = 4 eV to 12 eV).[19] This huge energy barrier makes it difficult to thermally or optically excite electrons from the VB to the CB, and hence results in low electrical conductivity. The band structure of a semiconductor lies in between that of a metal and an insulator, giving it unique properties. The band structure is actually similar to

that of an insulator but the E_g is smaller (~ 0.5 to 3.8 eV).[19] Thus, it is easier to promote electrons from the VB (or near E_f) to the CB, leading to activated electrical conductivity.

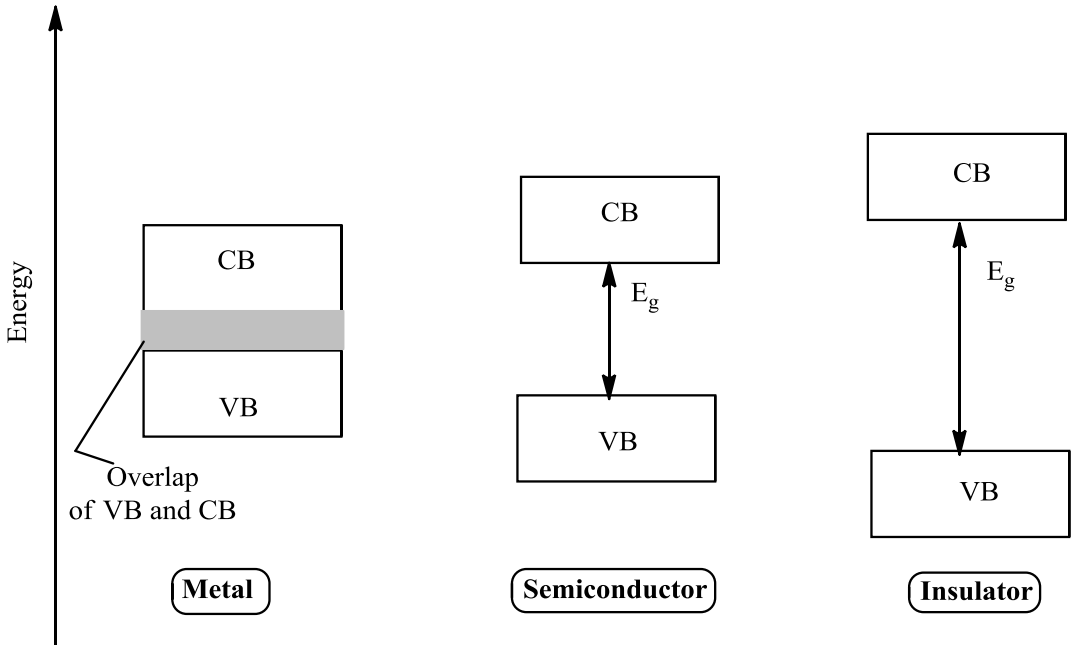

Figure 1.3 Band diagram of metals, semiconductors and insulators, showing the position of conduction band (CB) and valence band (VB), separated by band gap energy (E_g).

When stimulated by heat or light of sufficient energy (usually greater than E_g), the electrons in a semiconductor can be excited from the VB to the CB, leaving behind a hole in the VB. This leads to the formation of an electron-hole pair, called an *exciton*. The average distance between the electron and hole is termed as the *bulk exciton Bohr radius*. This electron and hole are attracted to each other by Columbic forces but on the application of external electric field, can be used to generate current in a device as they move in opposite directions in the CB and the VB, respectively.[18] The Bohr radius is intrinsic to a material. For example, CdS has a Bohr radius of 5.8 nm while PbTe has a Bohr radius of 50 nm.[20, 21] As the size of the bulk semiconductor decreases below that of the natural Bohr radius of the exciton, the material is said to be in a quantum confined state (**Figure 1.4**). This occurs due to the splitting of the continuum of energy

levels or bands (VB and CB) into discrete energy levels as the number of atoms (atomic orbitals) decreases from that present in the bulk material. The result is an increase in band gap with decreasing particle size. As a result, the energy required to promote an electron from the ground state to the first excited state also increases in nanocrystals as the size decreases. This change can be seen as a blue shift in the absorption spectra for nanocrystals with respect to the bulk material.[18] Because the band gap in nanocrystals can be changed by varying their size, their optical properties are size tunable.

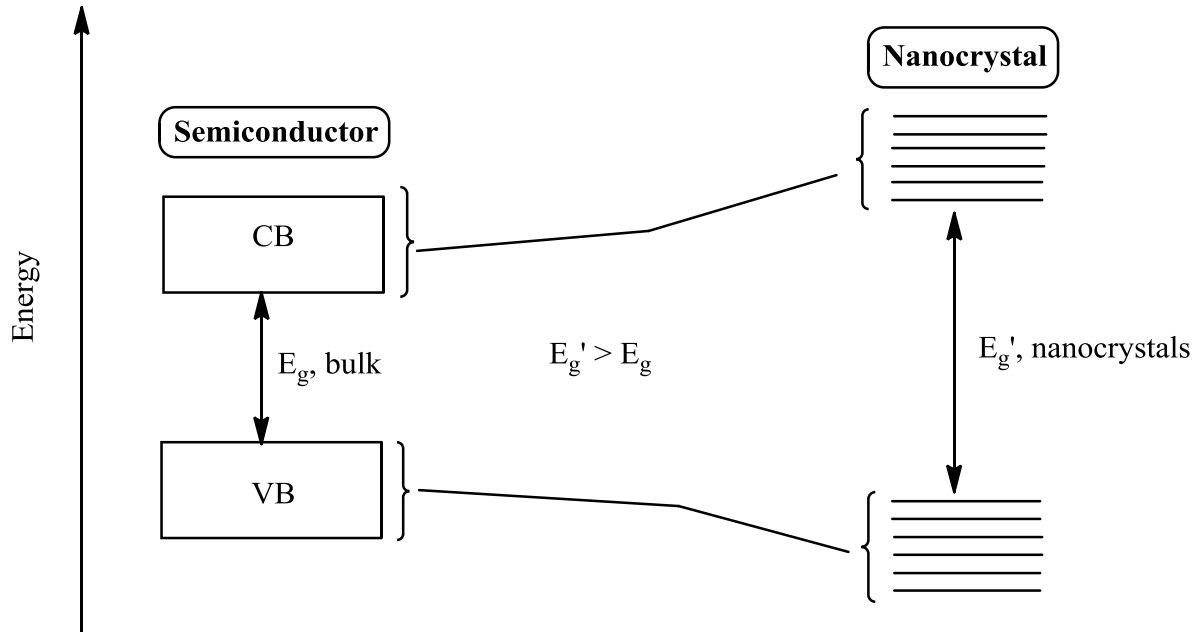

Figure 1.4 Band diagram of a semiconductor and corresponding semiconductor nanocrystals showing discrete energy levels and increased band gap.

1.3 Nanostructures for Enhancing ZT

Recently, several researchers have tried to enhance the ZT of a material via nanostructuring. For example, proof of principle experiments in PbTe quantum well structures,[16] $PbSe_{0.98}Te_{0.02}$/ PbTe quantum dot superlattices and Si/Ge superlattices[22] (superlattices are periodic structure of

materials forming layers of several nm thickness) demonstrated that a ZT > 1 is possible. In the first two cases, the operable mechanism is the quantum confinement effect, which increases the density of states near the Fermi level and enhances the ZT, whereas in the case of the Si/Ge superlattices, the operable mechanism is the decrease in thermal conductivity due to acoustic (coherent lattice vibration) mismatch between the constituent components, which again enhances the overall ZT of the system. Researchers have also tried to improve ZT by effectively incorporating nanomaterials into bulk matrices with a size and spacing range of $1 \leq \lambda_{ph} \leq 100$ nm. Here λ_{ph} is the phonon mean free path. These nanoinclusions are much more effective in scattering the mid- to long wavelength phonons that are not scattered by atomic substitutions. Examples include superlattices of PbSe nanodots embedded inside a PbTe bulk matrix, leading to an enhanced ZT of ~ 1.7 at 300 K as compared to the ZT of 1 for bulk PbTe.[23]

Another approach to nanostructuring is an *in situ* synthesis in which nanophases are created by exploiting an inherent phase segregation or decomposition in the alloy or the compound system under investigation. For example, the $AgPb_mSbTe_{m+2}$ (LAST-m) family of compounds exhibit a ZT >1.5 due to inhomogeneities on the nanoscale.[24] Recently, Kanatzidis and coworkers have shown that by endotaxially placing SrTe in an Na_2Te-doped PbTe matrix, the thermal conductivity could be reduced and the power factor could be enhanced, achieving a ZT of 1.7 at 800 K.[25] All these findings marked the start of the nanostructure era of TE research.

1.3.1 Techniques Employed for Engineering Nanostructures for Thermoelectrics

Low dimensional materials like nanocrystals, nanowires and superlattices achieve enhanced ZTs via optimization of electronic as well as phonon properties, as mentioned in the previous section. On the one hand, the classical quantum confinement effect enhances the power factor by enhancing the density of states near the Fermi level and the additional interfaces and grain

boundaries decrease κ_l and thus enhance the overall ZT of the material. Researchers have employed various techniques to engineer nanostructures, including molecular beam epitaxy (MBE), matrix encapsulation and ball milling. In MBE, the elements or compound to be deposited are heated to high temperatures in order to produce gaseous atoms or vapors. These are then targeted in the form of beams (molecular beams) under high vacuum conditions onto a heated substrate where they diffuse and slowly condense to form uniform films. High vacuum conditions are crucial to maintain high purity of the growing films, which takes place slowly as this ensures uniform and epitaxial growth.[26] This technique has been extensively used by the TE community in order to achieve enhanced ZT nanostructures. For example, Majumdar and coworkers have used MBE to incorporate ErAs nanoparticle layers epitaxially inside a $In_{0.53}Ga_{0.47}As$ bulk matrix deposited on a semi-insulating InP substrate.[27] They have observed significant reduction in thermal conductivity relative to the bulk matrix, leading to enhancement of ZT. This method produces uniform superlattice layers but it is slow, expensive and not practical for large scale production.

Another prominent technique, the matrix encapsulation method, uses phase segregation, in which one material (the minor phase) is encapsulated inside another material (the major phase) by the process of melting and cooling. Kanatzidis and coworkers have used this method to include nanometer sized Sb, Bi and InSb into a bulk PbTe matrix and observed a reduction in lattice thermal conductivity with respect to the pure bulk matrix.[28] This method produces materials on a large scale, but enables very little control on the inclusion size and is also limited by the solubility of the component chemical constituents.

Ball milling is another method used by researchers to enhance ZT, where the material to be crushed is put into a ball mill (grinder) along with grinding medium (ceramic or stainless steel

balls). When the ball mill rotates, the materials are ground into fine particles by a series of crushing events from the grinding media. For example, Morelli and coworkers have prepared nanogranular samples of p-doped PbTe and finely grained samples of PbTe with EuTe inclusion (the EuTe inclusion was obtained by adding $Pb_{0.92}Eu_{0.08}Te$ with the bulk PbTe) via ball milling leading to enhanced thermopower for both the samples relative to the bulk PbTe materials.[29] In this process, controlling the grain boundary size remains a challenge. Moreover, this high energy process produces strain in the crystallites, which could change the intrinsic properties of the materials.

A number of groups have turned to nanoparticle assembly methods for generating nanostructures as these methods are less tedious and more cost effective. For example, self organization of colloidal nanocrystals can form periodic long range ordered structures (superlattices) via a solution based approach. Various nanocrystals have been assembled via this method, including the thermoelectrically relevant phases PbSe and PbTe. Murray and coworkers have used solution based deposition of ligand-capped PbSe nanodots for forming superlattices. Unfortunately, the electrical conductivity of the films was poor due to the presence of ligands at the nanoparticle–nanoparticle interface. An enhancement in electrical conductivity was achieved by treatment with hydrazine, resulting in replacement of the bulky insulating capping ligands (oleate groups) with hydrazine, reducing the interparticle spacing and hence increasing the overall charge transport of the material.[30] In 2009, Talapin and coworkers showed that replacing the insulating capping ligands with molecular metal chalcogenides (MCCs) and further decomposing the MCC's with gentle heat treatment led to increased electrical conductivity over that achieved by hydrazine treatment.[31] Recently, the same group has shown the synthesis of colloidal lead and bismuth chalcogenide nanoparticles capped with antimony-chalcogenide

molecular complexes which could potentially be used as TE materials. The nanostructured thin films of p-type $(Bi,Sb)_2Te_3$ and n-type $(Bi,Sb)_2(Te_{0.9}Se_{0.1})_3$ exhibited very high Seebeck coefficients and electrical conductivities of ± 200-250 μV/K and 450 S/cm, respectively. Thus, a power factor of 20.4 $\mu W/(cm.K^2)$ and a ZT of 0.7 was achieved.[32] An alternative method to potentially improve the electrical conductivity in solution-derived nanostructures is to assemble particles so that the interfaces are composed of the same chemical constituents as the interior of the particle. This can be achieved via sol-gel methods.

1.4 Sol-Gel Methodology

The sol-gel method, as the name suggests, comprises formation of a sol followed by generation of a gel network. In this process, the nanoparticles (sol) are connected in a 3-dimensional fashion leading to an interconnected network with minimal or no organic ligands at the interface (gel), potentially leading to enhanced electron transport and greater thermal stability. The sol-gel method has been extensively studied for the synthesis of metal oxide gels such as SiO_2 and TiO_2. The typical sol-gel process, as applied to metal oxides, consists of hydrolysis and condensation steps. In the hydrolysis step, the metal oxide precursors, such as $M(OR)_n$ (where M = Si, Ti and OR = alkoxy group) are hydrolyzed to form hydroxylated metal centers with alcohols as the byproduct (equation 1.8). The hydroxylated metal centers are then condensed to generate polymers with the release of water and alcohol as byproducts (in the condensation step) by connecting the nanoscale particles through oxygen bridging (equation 1.9). The sol-gel process is catalyzed by acids or bases. When an acid is used as catalyst, the condensation step governs the rate of reaction (rate determining step), and thus the hydrolysis step is favored (accelerated). This results in the formation of a large number of hydroxylated species that eventually form a polymeric gel network with small pores. On the other hand, when

a base is used as catalyst, the hydrolysis is the rate determining step and condensation is favored, resulting in an interconnected network of particles that leads to larger pores.

Hydrolysis Step:

$$M(OR)_n + H_2O \longrightarrow [M(OR)_{n-1}(OH)] + R\text{-}OH \quad (1.8)$$

Condensation Step

$$M\text{-}OH + M\text{-}OX \longrightarrow M\text{-}O\text{-}M + XOH \ (X= H \text{ or } R) \quad (1.9)$$

The wet gel can be dried in a number of ways. In 1932, Kistler observed that when a wet gel was allowed to dry under ambient conditions, the gel would shrink considerably from its original size. This is because of the surface tension exerted by the liquid-vapor interface of the evaporating liquid, which leads to pore collapse and formation of a xerogel network (**Figure 1.5**). On the other hand, when the same wet gel was subjected to supercritical drying where the liquid entrapped in the pore walls was brought to a supercritical state with no liquid-vapor interface, and hence no surface tension, it leads to an aerogel network where the original pore structure of the wet gel is retained.[33]

The aerogel and the xerogel are inorganic polymers composed of nanoscale building blocks. Aerogels have a large number of pores (voids) occupying ~ 90 % of the volume, and hence are less dense and have higher surface area than the xerogels. Also, aerogels consist of a broad range of pore sizes including micropores (< 2 nm), mesopores (2-50 nm) and even macropores (> 50 nm) whereas the xerogels have a narrow pore range, consisting of only the micro and mesopores.[33-35] Due to the open structure in the aerogels and the xerogels, they have been utilized in various applications such as catalysis, sensing and thermal insulation.[33, 35]

With respect to thermal insulation, the thermal conductivity of the aerogel is very low when composed of insulating oxide, relative to the corresponding xerogels. As thermal insulators, these materials can be used to prevent parasitic heat loss in TE devices.[36] They are used in IR detectors as a shield for blocking the heat generated from the substrates. They can also be used as coating for solar cells owing to their low refractive indexes.[35]

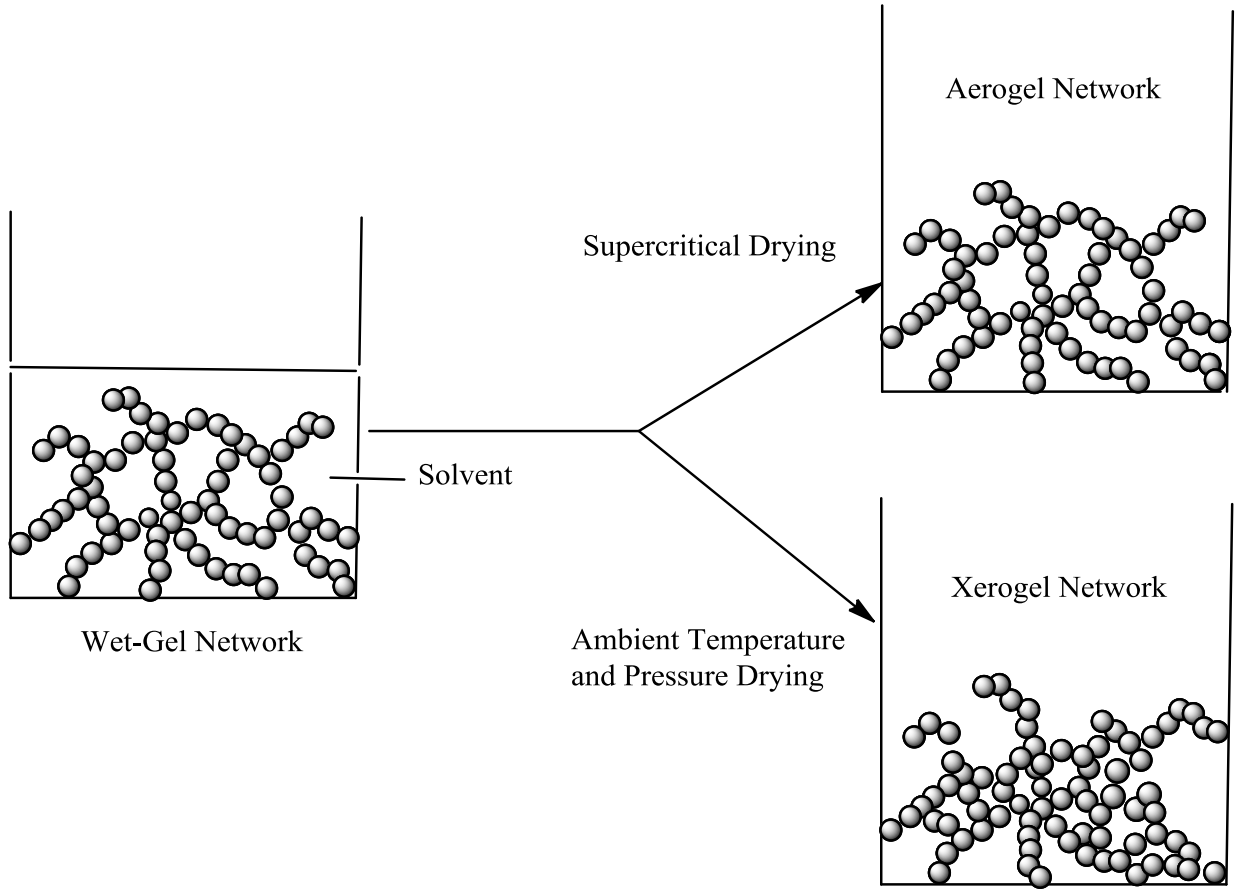

Figure 1.5 Pictorial representation of a wet gel network, an aerogel network formed after supercritical drying showing retention of the initial pore structure, and a xerogel network formed after ambient temperature and pressure drying showing pore collapse.

Application of the sol-gel approach to the heavier group 16 elements chalcogenides is of interest due to the quantum confined properties exhibited by the semi-conducting nanoparticles. For example, materials such as lead chalcogenides PbS, PbSe and PbTe exhibit optoelectronic properties in the infrared region and can be used for applications in infrared photovoltaic devices and thermoelectrics.[37] Additionally, materials such as $CuInS_2$ and $CuInSe_2$ exhibit optoelectronic properties in the visible region and can be useful in devices like light emitting diodes (LEDs) and photovoltaics. Thus, exploiting the sol-gel chemistry of metal chalcogenides could open new ventures in the wide range of applications associated with chalcogenide materials.

1.4.1 Sol-Gel Synthesis of Metal Chalcogenides

In order to prepare the metal chalcogenide gels and aerogels, three basic approaches have been used: a) thiolysis reactions,[38] b) condensation reactions of anionic clusters with metal cations[39] and c) condensation of discrete metal chalcogenide nanoparticles.[40, 41] The thiolysis process is similar to the hydrolysis step in the traditional sol-gel reaction, but it uses gaseous H_2S instead of water, giving rise to metal sulfide gels upon condensation. For example, germanium sulfide gels were synthesized by Brock and coworkers via a thiolysis and condensation reaction.[38] The disadvantage of this process is that it is limited only to metal sulfides, and also the products obtained are usually amorphous. The second approach, the condensation of anionic clusters with metal cations, has been extensively studied by Kanatzidis and coworkers. In this route, the chalcogenide gels (chalcogels) are obtained via a metathesis reaction between Zintl anionic clusters (like the $[Ge_4S_{10}]^{4-}$ anion) and Pt^{2+} and Ni^{2+} cations. The same group has synthesized aerogel materials of Co(Ni)-Mo-(W)-S networks by reaction between $(MoS_4)^{2-}$ and $(WS_4)^{-}$ with Co^{2+} and Ni^{2+} salts.[42] They have also shown that these chalcogel networks have higher activity for hydrodesulfurization of thiophene than conventional Co-Mo/Al_2O_3 catalysts.

Another approach for chalcogenide aerogel formation (the third approach) is a two step process whereby the first step would consist of synthesizing discrete metal chalcogenide nanoparticles followed by oxidative condensation of the nanoparticles to give a gel network. In 1997, Gacoin and coworkers applied this route to obtain wet gels of CdS materials.[41] In brief, they used an inverse micellar approach to synthesize CdS nanoparticles, capped them with 4-fluorothiophenolate surface ligands and then oxidized the thiolate capped nanoparticles with an oxidizing agent, H_2O_2, to get the wet gels. In our group, extensive work has been done on extending the sol-gel strategy and synthesizing aerogels of CdS, ZnS, PbS and CdSe, among others.[43-46]

Recently, researchers have started to focus on the heavier chalcogenides (tellurides) rather than sulfides and selenides, as the tellurides show unique optoelectronic properties. Among the tellurides, there have been several reports in the literature regarding the assembly of CdTe nanoparticles.[47, 48] Brock and coworkers have shown that the sol-gel assembly can be extended to CdTe discrete nanoparticles, and the oxidative assembly occurs irrespective of the surface capping group (thiolate or trioctylphosphine oxide). Gaponik and coworkers have also synthesized aerogels of CdTe by condensation of thioglycolic acid-capped CdTe nanocrystals. Here they have used photochemical as well as chemical oxidation to induce gelation.[48]

While there is precedent for CdTe aerogel network formation in the literature prior to the dissertation research, no report exists for the synthesis of PbTe and Bi_2Te_3 aerogel networks. These materials are important as they are potential candidates for thermoelectric applications, and it is expected that the interconnected network of nanoparticles (aerogel and xerogel) and the absence of intervening surface organic ligands would lead to enhanced electrical conductivity relative to ligand-capped nanoparticle superlattices.[49] In addition, the pore-matter interface in the

gel network is expected to assist in scattering the heat carrying phonons, thereby decreasing κ_l and leading to an increase in ZT of the system.

1.5 Methods to Synthesize Lead and Bismuth Telluride Nanoparticles

Various methods have been used to prepare PbTe and Bi_2Te_3 nanoparticles. These include hydro (solvo) thermal, sonochemical and arrested precipitation methods, as detailed below.

Hydrothermal processes (where the precursor solution is aqueous) and solvothermal approaches (where the precursor solution is nonaqueous) have been used to make discrete PbTe and Bi_2Te_3 nanoparticles. In these techniques, substances are prepared at high temperature and pressure in an autoclave to produce highly crystalline nanoparticles. For example, PbTe nanoboxes of thickness ~ 200 nm were prepared by Ren and coworkers following the solvothermal approach[50, 51] and Li and coworkers have synthesized PbTe nanowires hydrothermally.[52] In another study, Kumbhar and coworkers have prepared 100 nm sized discrete cubic PbTe nanoparticles and 30 nm irregular Bi_2Te_3 flakes (aggregated) both solvothermally as well as hydrothermally.[53] In most of the above cases, elemental precursors or their respective salts were used along with hydrazine or sodium borohydride as reducing agents. More complex ternary and quaternary phases like $Bi_{0.5}Sb_{1.5}Te_3$[54] and $AgPb_{18}SbTe_{20}$[55] have also been prepared using these methods.

The sonochemical method is another way of preparing PbTe and Bi_2Te_3 nanostructures and alloys. It uses ultrasonic vibrations to perform chemical reactions. In this technique the chemical reaction occurs due to acoustic cavitation, which is the formation, growth and implosive collapse of bubbles in a solvent, giving intense local heating and a pressure sufficient for any chemical reactions to occur.[56] For example, Li and coworkers have prepared 20-40 nm flakes of Bi_2Te_3 nanocrystals, which are in aggregated form, and 60-80 nm irregular shaped particles of Bi_2Se_2Te

and Bi_2SeTe_2 nanomaterials using this technique.[57] Qian and coworkers have also used sonochemical methods for preparing irregular shaped PbTe nanoparticles.[56]

Although hydrothermal, solvothermal and sonochemical methods produce highly crystalline nanoparticles and alloys, they also possess several disadvantages. They do not enable control of the size of the nanoparticles obtained. The samples are usually polydisperse, and for the sonochemical method, the reaction products are highly sensitive to the frequency and intensity of ultrasound, thus bulk production is inhibited.[51]

In order to control the size and shape of material, and to obtain highly crystalline nanomaterials of PbTe and Bi_2Te_3, another synthetic approach known as ligand based synthesis or arrested precipitation is used. Highly monodisperse nanocrystals that are organically passivated are produced by this route. In the arrested precipitation approach, depending upon the choice of organic ligands, reaction temperature, time and concentration of precursors used, the size and shape of the nanoparticles can be controlled. For example, Murphy and coworkers have synthesized highly crystalline PbTe nanoparticles using oleic acid as the surfactant (binding ligand) and octadecene as the solvent. The size of the nanoparticles obtained by varying the concentration of precursors and the ligands was from 3-8 nm.[37] Urban and coworkers have synthesized monodispersed PbTe nanoparticles using squalene instead of octadecene as the solvent and oleic acid as the surfactant, giving nanoparticles with diameter from 4-10 nm by varying the surfactant/solvent ratio as well as the growth time of the reaction mixture.[58]

Bi_2Te_3 nanoparticles have also been synthesized by ligand assisted arrested precipitation methods. Dirmyer et al., have synthesized Bi_2Te_3 nanoparticles (in sizes ranging from 17 nm to 90 nm) using various alkane thiols of different chain length including 1-dodecanethiol or octanethiol as ligands and diphenylether as solvent.[59] In another study, Bi_2Te_3 nanoparticles were

synthesized via low temperature micelle formation. The procedure includes formation of two separate microemulsions, one of orthotelluric acid in sodium bis (2-ethylhexyl) sulfosuccinate (AOT) and the other of bismuth salt in AOT plus thioglycolic acid (leading to bismuth ion ligation with thioglycolic acid). Mixing of the two microemulsions and reduction with hydrazine monohydrate leads to the formation of 2.5 to 10.4 nm sized nanoparticles. The size of the nanoparticle obtained depends upon the water/AOT ratio.[60] Scheele and coworkers[61] have also reported synthesis of Bi_2Te_3 nanoparticles (10 nm) where Bi nanoparticles were first formed using oleylamine as the reducing agent, followed by reaction with the anion Te precursor leading to alloy formation, which eventually lead to crystalline Bi_2Te_3 nanoparticles upon annealing. Recently, the same group has synthesized 15-20 nm sized $Bi_{2-x}Sb_xTe_3$ nanoparticles by the same approach; the only difference being that antimony precursors are used along with the bismuth precursor to achieve the targeted composition.[62]

1.6 Thesis Statement

While remarkable progress has been achieved in the synthesis of discrete nanoparticles for TE applications, the major challenge lies in assembling these nanoparticles into functional devices. Though methods like molecular beam epitaxy,[63] matrix encapsulation[28] and self assembly generate nanostructures, they suffer from various drawbacks. For example, in case of superlattices formed by self assembly, the individual particles are covered with a sheath of organic ligands that acts as an insulator and hampers electrical conductivity in the system. In composite materials, the optimal size and spacing of inclusions, as well as the effects of their interfacial characteristics and native electronic properties on ZT, remains unexplored in large part because of the challenges faced in controlling size and shape and placement of inclusions. An alternate approach to generating inclusions *in situ*, where size and placement cannot be

controlled, is to generate them *ex situ* and then introduce them to a bulk matrix. One solution-based approach is the *sol-gel assembly* method developed in our lab for assembling discrete nanoparticles of lighter sulfides and selenides into nanostructures,[40, 41, 45] eliminating intervening organic ligands that could act as trap centers for charge carriers,[30] thus providing better electrical conductivity to the system, and control of the size and shape of individual building blocks. My dissertation project is mainly focused on the synthesis and characterization of chalcogenide nanostructures, prepared by sol-gel or incipient wetness techniques, of Bi and Pb for potential thermoelectric applications.

In the first part of the dissertation research, we explore the possibility of extending the sol-gel assembly method to tellurides, such as PbTe, that are established TE materials in bulk form.[1] The synthesis and characterization of PbTe nanoparticles and gel systems, including both aerogels and xerogels, will be described. In addition, the thermal stability comparison of the aerogel with PbTe discrete nanoparticles will also be evaluated, as elevated temperature operation is a requirement for efficient thermoelectric power generators.

In addition to PbTe, Bi_2Te_3 alloys are state-of-the-art thermoelectric materials for operation near room temperature.[1, 11] To explore the thermoelectric properties of Bi_2Te_3 nanostructures, we focused on extending our sol-gel methodology to the synthesis of these materials. The intent of this part of the dissertation research was to synthesize Bi_2Te_3 nanoparticles and aerogels on a large scale, enabling assessment of the thermoelectric properties. Additionally, we will also evaluate the effect of Sb inclusion in Bi_2Te_3 (for controlling the dopant concentration) on the thermoelectric properties and then compare the results obtained with those for the undoped Bi_2Te_3 aerogel samples.

In the final part of the dissertation research, we exploit the concept of heterostructured nanocomposites by inclusion of discrete PbTe nanoparticles in a bulk Bi_2Te_3 matrix (which is either n- or p- doped) via an incipient wetness impregnation method. The effect of impregnating different concentrations of PbTe nanoparticles in the bulk matrix as well as the native doping of the bulk matrix on the thermoelectric properties of the heterostructures will be presented.

Overall, my dissertation consists of Chapters 1 and 2 entailing an overall introduction and description of the experimental techniques, respectively. Chapter 3 will describe the synthesis and characterization of PbTe nanoparticles and aerogels via a sol-gel methodology along with their physical characteristics. Chapter 4 describes the extension of the sol-gel methodology to Bi_2Te_3 nanoparticles and aerogels, and measurement of their transport properties; the synthesis and characterization of Bi_2Te_3 nanoparticles doped with antimony (Sb), and resultant aerogels, will also be described. Chapter 5 will present the synthesis and characterization of heterostructured nanocomposite materials via incorporation of PbTe nanoparticles (in different wt %) inside a Bi_2Te_3 matrix (n- or p- doped) by the incipient wetness method and the thermoelectric properties of the composites. Finally, Chapter 6 will provide overall conclusions for the dissertation research and also a prospectus for future studies.

Chapter 2

Experimental Methods and Characterization Techniques

This chapter focuses on the experimental methods and characterization techniques used for the synthesis and analysis of the materials in this dissertation study. The materials used or synthesized were sensitive to air/moisture, so handling of these materials in inert gas atmosphere, and glove box techniques will be discussed. Moreover, the drying techniques for wet gels to yield aerogel and xerogel will be covered. Characterization techniques including Powder X-ray diffraction (PXRD), transmission electron microscopy (TEM), energy dispersive spectroscopy (EDS), thermogravimetric analysis (TGA), differential scanning calorimetry (DSC), porosimetry (surface area analysis) and infrared spectroscopy (IR), will be described. This chapter also entails a brief introduction of the techniques used to measure thermoelectric properties: Seebeck coefficient (S), electrical resistivity (ρ), thermal conductivity (κ) and carrier concentration measurements (n).

2.1 Experimental Methods

2.1.1 Inert-Atmosphere Glove Box

The inert atmosphere glove box provides a simple way of handling and storing air/moisture sensitive materials. A glove box consists of a large gas-tight box with a window, gloves and a gas tight door for transferring materials. The window has one or more pair of gloves, used for working inside the box. The glove boxes are usually kept at a higher pressure than the surrounding atmosphere so that in case of leaks, inert gases (like argon) can escape out instead of air getting inside the box. In order to work inside the glove box, the internal pressure is reduced and is maintained at an optimal level.[64] To sustain the air and moisture free environment inside the glove box, an inert gas (argon, as used in the dissertation research) is continuously circulated

through a copper catalyst and molecular sieves. To keep the catalyst's surface fresh, it is periodically regenerated by heating the catalyst under a mixture of H_2 and N_2 gases. The oxygen adsorbed on the catalyst's surface reacts with H_2 to give water, which is flushed out of the box along with water during the final evacuation step of regeneration process. The glove box used for this dissertation research is an HE-493 vacuum atmosphere, equipped with a large and a small antechamber and one refrigerator.

2.1.2 Schlenk Line Technique

Schlenk line techniques are another way of operating in an oxygen free atmosphere. A Schlenk line consists of several different ports that enable several reactions to be run simultaneously. One manifold is connected to the vacuum while the other is connected to an inert gas supply (argon gas was used in the dissertation research).[64] A two way stopcock on each port enables switching between vacuum and inert gas atmosphere. The glassware used for the reaction, Schlenk flasks, are designed with a special sidearm to which rubber tubing is connected, which in turn is connected to the Schlenk line. Thus the flask can be either evacuated or filled with an inert gas. A bubbler is also provided (which is usually connected by a needle) to control the excess pressure build up in the reaction flask and prevent back flow of air.

2.1.3 Gel Drying (Supercritical and Ambient) Techniques

Supercritical drying of wet gels yield aerogels while benchtop drying yields xerogels.[34, 35] In supercritical drying, the solvent (acetone, used in this dissertation research) trapped within the pores of the wet gels is exchanged with the supercritical fluid (CO_2, used in the dissertation research), in its normal liquid state, in a closed container. The liquid is then heated to its critical temperature and pressure, resulting in formation of a supercritical fluid. **Figure 2.1** shows the phase diagram of CO_2. When the temperature of the sealed container is increased beyond 31 °C, the pressure also increases beyond 7.3 MPa. At this temperature and pressure, CO_2 adopts the

supercritical state, which ensures minimal surface tension and capillary pressure leading to minimal collapse of pore walls and giving the pore structure of the starting wet gel upon slow release of pressure (CO_2 evolution), producing an aerogel. For xerogel formation, the solvent trapped in the pores of the wet gels is evaporated at ambient temperature and pressure. The presence of a liquid-vapor meniscus leads to surface tension, collapsing pore walls and reducing porosity.[35]

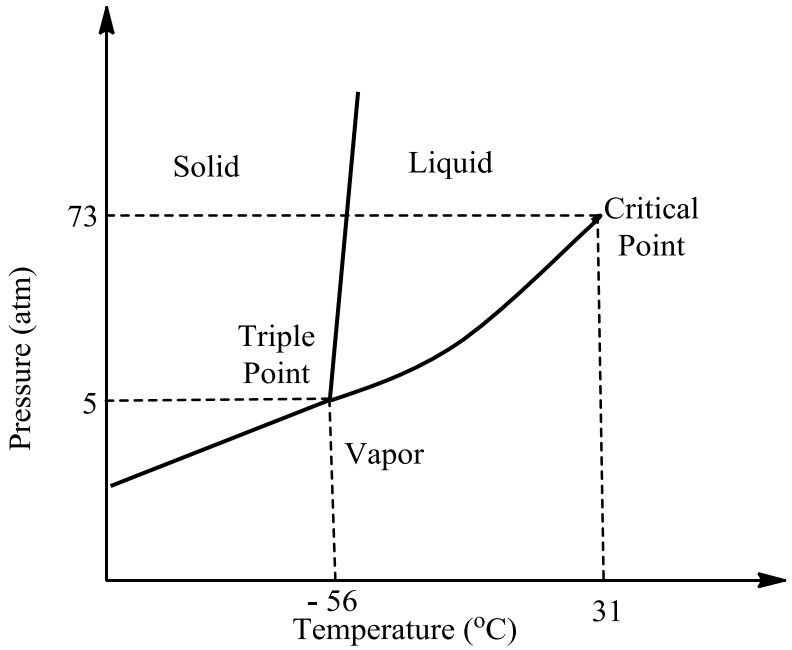

Figure 2.1 Phase diagram of CO_2 showing triple and critical points, as adapted from Pierre and Pajonk.[35]

The details for the supercritical drying procedure for aerogel formation used in this dissertation study are as follows: the wet gels were immersed in acetone and then transferred to either porous capsules or glass vials. The capsules were loaded onto a boat which in turn was loaded in the critical point dryer (CPD), a SPI-DRY model, whereas the glass vials were loaded directly in the dryer. The CPD is connected to a liquid CO_2 tank and an ISOTEMP 1006S model water heater/cooler that is used to control the temperature of the CPD. Once the capsule or the

vials were loaded into the dryer, it was filled with liquid CO_2 and the temperature of the CPD chamber was set to 19 °C and the pressure rose to 900-1000 psi. After 1 h, the liquid CO_2 was drained off and fresh liquid CO_2 was refilled. This exchange was followed twice more and then the temperature of the chamber was increased to 39 °C and the pressure rose to 1400-1500 psi producing supercritical CO_2. This state was maintained for 30 min, followed by venting of the fluid, releasing the pressure and eventually forming the aerogel. For the xerogel formation, the wet gels were transferred to a fresh glass vial and the solvent entrapped in the pore walls (acetone) was dried on the bench top at ambient temperature and pressure.

2.2 Characterization Techniques

2.2.1 Powder X-ray Diffraction (PXRD)

Powder X-ray Diffraction is one of the most powerful techniques used to identify the structure of materials. This technique provides additional information on crystallite size, crystallographic phase, lattice parameters and purity of the material. It uses high energy X-rays, which are electromagnetic radiation of wavelength ~ 1 Å (10^{-10} m) that are produced when highly charged particles, like electrons, collide with matter.[19] The schematic diagram for X-ray production is shown in **Figure 2.2**. When a beam of electrons from a heated tungsten filament is allowed to strike a metal target (Cu or Mo), the electrons from the K shell (1s) of the metal are knocked out, creating vacancies as shown in **Figure 2.3**. These vacancies are immediately filled by electrons from a higher level i.e., L or M shell, by dropping down to the K shell. Energy is released during this process and it appears as X-ray radiation. Usually, a series of transitions occurs during this process; for example in Cu, the two transitions: 2p → 1s, called Kα and having wavelength λ = 1.5418 Å and 3p → 1s, called Kβ and having λ = 1.3922 Å, are the most intense. For this dissertation study, Kα radiation (which consists of doublet $K\alpha_1$, λ = 1.54051 Å and $K\alpha_2$, λ =

1.54433 Å) from a Cu target is used. Nickel foil filters are used to filter out the Kβ and Bremsstrahlung radiation.

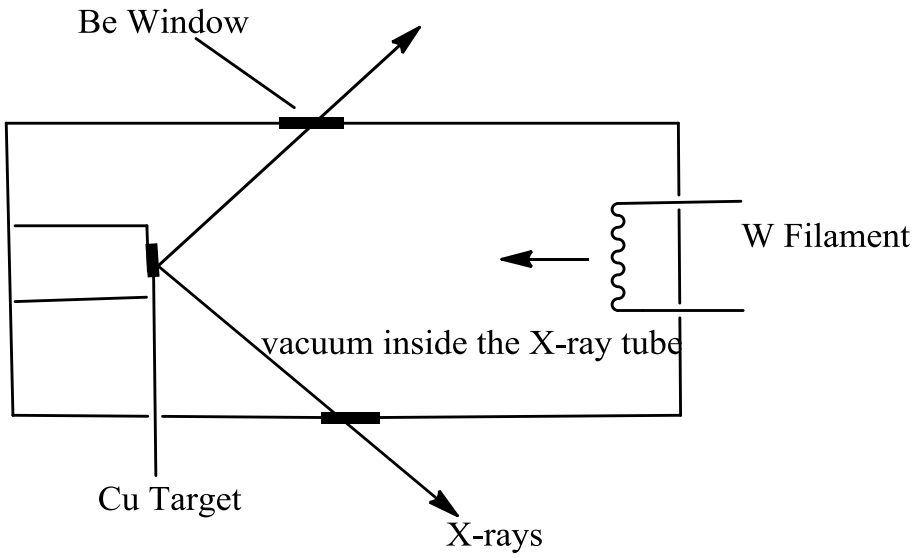

Figure 2.2 Schematic diagram of production of X-rays from a tube with a Cu source, adapted from West.[19]

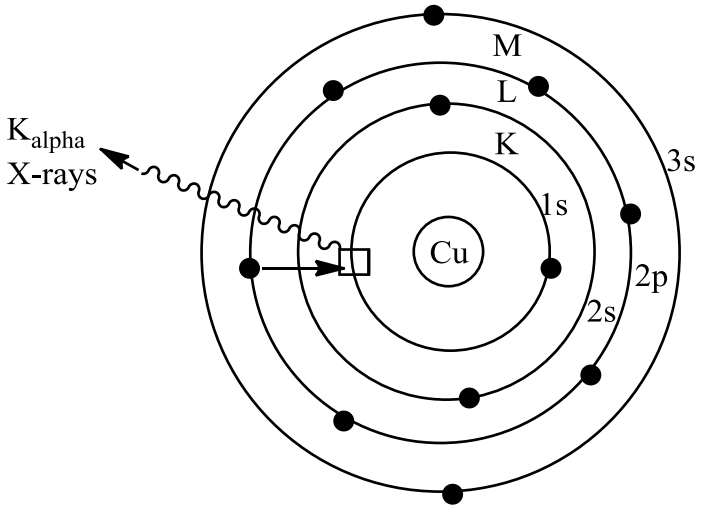

Figure 2.3 Schematic diagram of shells depicting X-ray production, adapted from West.[19]

Bragg's law is applied to the scattering of X-rays in order to relate scattering to crystal structure. In Bragg's approach, the crystals are regarded as layers or planes of atoms arranged in

a periodic fashion. When X-rays are incident, some rays are transmitted through the planes whereas some are scattered. For bulk crystalline materials, which contain a large number of crystal planes that diffract X-rays, only those diffracted beams that interfere constructively account for the peaks in PXRD.

The derivation of Bragg's laws is as follows: When two incident rays, M and N strike the crystal planes separated by a distance, d, with an angle of incidence, θ, they are reflected with the same angle, θ as M' and N', as shown in **Figure 2.4.** In order to have constructive interference (a peak), the path difference between the two rays should be an integral multiple of wavelength (λ) of the incoming rays. The path difference (Δx) between the two rays is given in equation 2.1, relations to λ and d in equations 2.2 and 2.3, and finally Bragg's law is given by equation 2.4.[19]

$$\Delta x = y + z \qquad (2.1)$$

$$y + z = n\lambda \qquad (2.2)$$

$$d\sin\theta + d\sin\theta = n\lambda \qquad (2.3)$$

Bragg's law $$2d\sin\theta = n\lambda \qquad (2.4)$$

In nanocrystals, which consist of a fewer number of crystal planes than a bulk crystalline solid, partial interference not satisfying Bragg's law can be observed due to an insufficient number of crystalline planes for perfect cancellation. Thus, for nanocrystals, the diffracted peaks are much broader than for larger crystallites. The broader the peak, the smaller is the coherence length of the material. The crystallite thickness (D) of the material can thus be derived from the broadening using the Scherrer formula (equation 2.5).

$$D = 0.9\,\lambda/\beta\cos\theta \qquad (2.5)$$

In equation 2.5, β is the full width at half maximum (FWHM, in radians) of the reflection, θ is the Bragg angle and λ is the wavelength of the source (which is 1.54051 Å for Cu $K\alpha_1$).

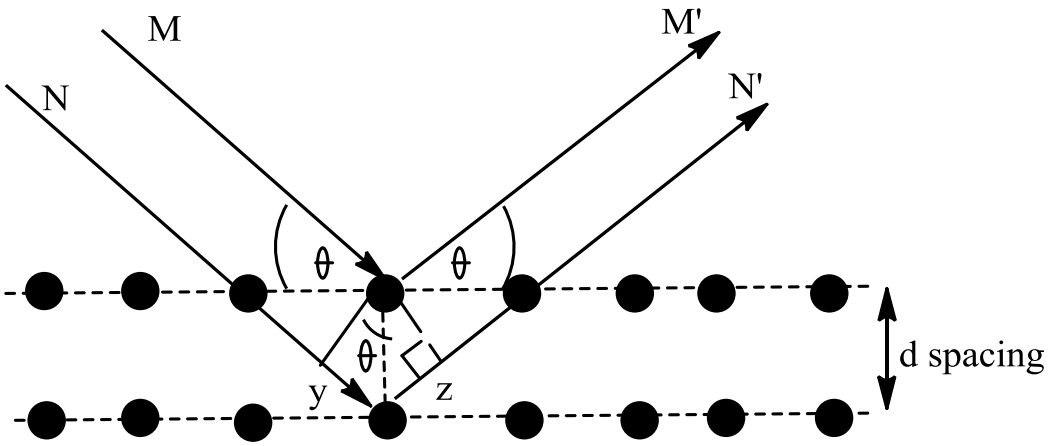

Figure 2.4 Pictorial representation of diffraction of rays from parallel crystal planes, adapted from West.[19]

In this dissertation study, a RIGAKU RU 200B diffractometer with a rotating Cu anode source is used. The powdered samples of the nanoparticles, nanocomposites, aerogels and xerogels were deposited on a quartz low background holder coated with a thin layer of grease. The data were collected in the 2θ range 20-70° with a step size of 1.2°, at 40 kV voltage and 150 mA current. The PXRD data obtained were processed using the JADE 5.0 software and compared to powder diffraction files (PDFs) from the International Center for Diffraction Data database (ICDD). The crystallite sizes were determined using the Scherrer equation (in JADE 5.0 software) after correcting the peak broadening by stripping $K\alpha_2$, using the FWHM of the peak under consideration. Unit cell refinement was done on data collected (in the same 2θ range and step size as mentioned above) by mixing the samples with an internal Si standard. The 2θ values were then corrected against the Si peaks using JADE 5.0 software. The corrected 2θ values were then used for cell refinement with the program CELREF V3 using least-squares methods.

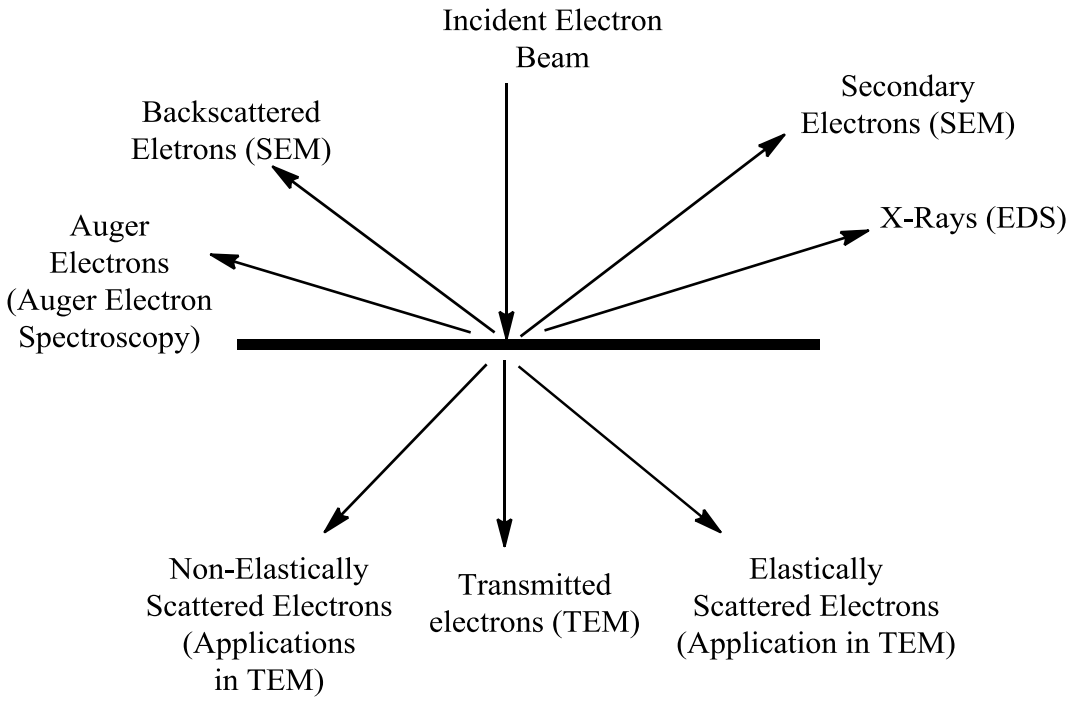

Figure 2.5 Schematic representation of the encounter of an incident electron beam and subsequent fate of the beam on interaction with the sample. TEM and EDS are discussed in this Chapter.

2.2.2 Electron Microscopy (EM)

Electron Microscopy is a common tool used for the routine characterization of nanomaterials, providing both structural and morphological information on the materials. This technique uses a highly energetic beam of electrons to examine materials on an atomic scale. The basic principle used in this technique is the same as optical microscopy, the only difference being that the latter uses light for imaging while the former uses electrons. EM exploits the wave-particle dual characteristics of electrons; the wave-like property of electrons is used for imaging while the particle-like character is used for determination of chemical information for the specimen. When high energy electrons are incident on a material, it leads to various interactions. Some of these

interactions are shown in **Figure 2.5**. The transmitted electrons from the source are used for the imaging mode in *transmission electron microscopy (TEM)*. The TEM often comes with an instrument that analyzes the energy of the emitted X-rays from the sample to provide information on its chemical components using a technique called *energy dispersive spectroscopy (EDS)*.

2.2.2.1 Transmission Electron Microscopy

The TEM instrument has a source for producing electron beams, called the electron gun. The most commonly used electron gun is the thermionic electron gun, in which the electrons are emitted from a heated filament thermionically and a divergent beam of electrons is produced (LaB_6 source). Another type of electron gun is the field emission gun, which uses a strong electric field for extracting electrons from the electron gun (often a tungsten (W) filament). The electrons can be emitted from the W filament at a high voltage between 50 kV and 400 kV. The relation between the wavelength of the electrons emitted and the accelerating voltage is given by equation 2.6.[19]

$$\lambda = \frac{h}{\sqrt{2meV}} \qquad (2.6)$$

In equation 2.6, m and e are the mass and charge of an electron, respectively; h is Planck's constant, V is the operating voltage and λ is the wavelength of electrons. Modifications to this equation occurs if operated beyond 100 kV as relativistic effects comes into factor when electron velocities becomes greater than half the speed of light.

The electron beam is focused using several condenser and objective lenses to make them strike the sample. The material under investigation should be thinner than ~ 2000 Å, as electrons are completely absorbed by thick specimens.[19] Likewise, the electron gun and lenses all operate under high vacuum to prevent scattering or absorption of electrons. The image obtained can be captured by film or digital camera.[65] A schematic for a TEM is shown in **Figure 2.6.**

The images in the TEM can be obtained via mass-thickness contrast and diffraction contrast. The mass-thickness contrast depends on the atomic number (Z) of the elements present in the sample, and also on the thickness of the sample under investigation. The dark areas obtained in the image are usually due to the presence of thicker sample areas with high atomic number and the brighter areas are due to regions which have no sample or have sample with lower contrast (thinner or lower atomic number). There are two basic modes of viewing samples based on diffraction contrast, called bright field imaging mode and dark field imaging mode. In the bright field mode only transmitted beams are used for imaging (**Figure 2.7**). The bright field mode provides information regarding morphology and thickness. In the dark field imaging mode, only the diffracted beams are selected for imaging. Here the crystalline portion appears bright whereas the amorphous regions, including the background, appear dark. The dark field mode provides information regarding the crystallinity and defects of the specimen (**Figure 2.7**).[65]

Selected area electron diffraction (SAED) is a technique associated with TEM by which crystallographic information can be obtained by imaging the diffraction of the sample. In this technique, the intermediate lens is focused on the back focal plane (containing the diffraction pattern) rather than image plane (containing the image of sample) of the objective lens. First, a point of interest on the specimen is selected in the bright field imaging mode.[65] An intermediate aperture is introduced and the microscope is switched to diffraction mode which confines the diffraction pattern of a selected area from the sample and shows rings of dots on the screen. Each dot in the sample corresponds to diffraction satisfying Bragg's law from the crystal planes of the sample, the only difference being here the electron beam is used instead of X-rays. The d-spacing can be calculated from the distance between the rings formed from the dots. This d-

spacing in turn gives information on the crystal structure and crystal orientation of the material. The ray diagram for SAED is depicted in **Figure 2.8**.

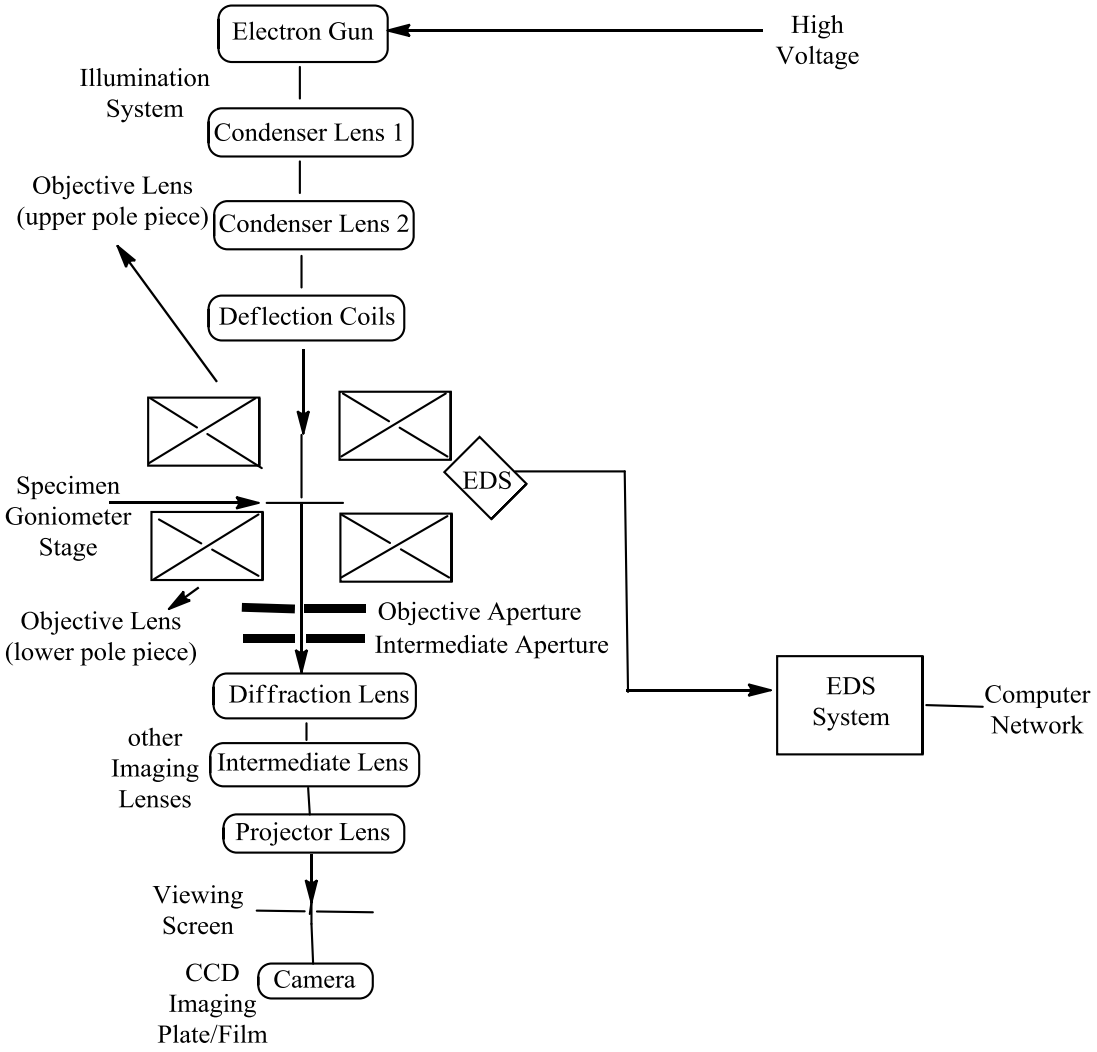

Figure 2.6 Pictorial representation of the parts in a TEM instrument, adapted from Fultz.[65]

In this dissertation study, a JEOL 2010 transmission electron microscope operated at a voltage of 200 kV and a current of 106-108 mA was used. Images obtained from TEM measurements were analyzed by Amtv600 software (Advanced Microscopy Techniques Corporation). Samples for TEM were prepared by dispersing nanoparticles and nanocomposites in hexane, or aerogels and xerogels in acetone, followed by sonication for 5 min, and then

deposition of a drop from each solution on a carbon-coated 200 mesh Cu grid (obtained from SPI) followed by air drying for 1 day. The imaging modes used for the dissertation are bright field and selected area diffraction modes.

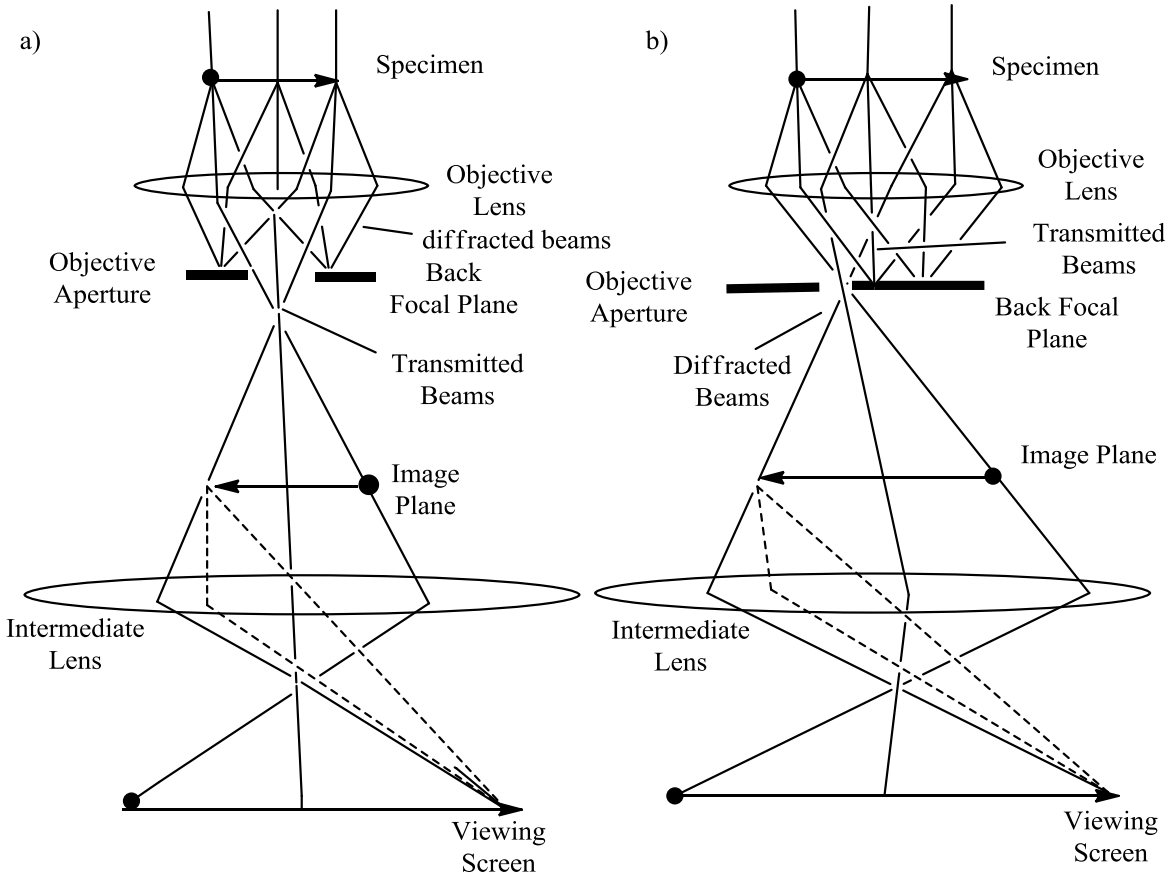

Figure 2.7 a) Bright Field imaging mode where transmitted electrons are used, b) Dark field imaging mode where only diffracted electrons are used, adapted from Fultz.[65]

In addition to routine imaging of specimens, the TEM can also be used for in-situ heating experiments using a Gatan model 652 double-tilt hot stage. The samples, as deposited on the carbon coated Cu grid, were loaded onto the Gatan heating stage and mounted in the TEM. The heating rate (10 °C/min) and temperature were controlled precisely using a Model 901 Smartset Hot Stage Controller made by Gatan Inc.

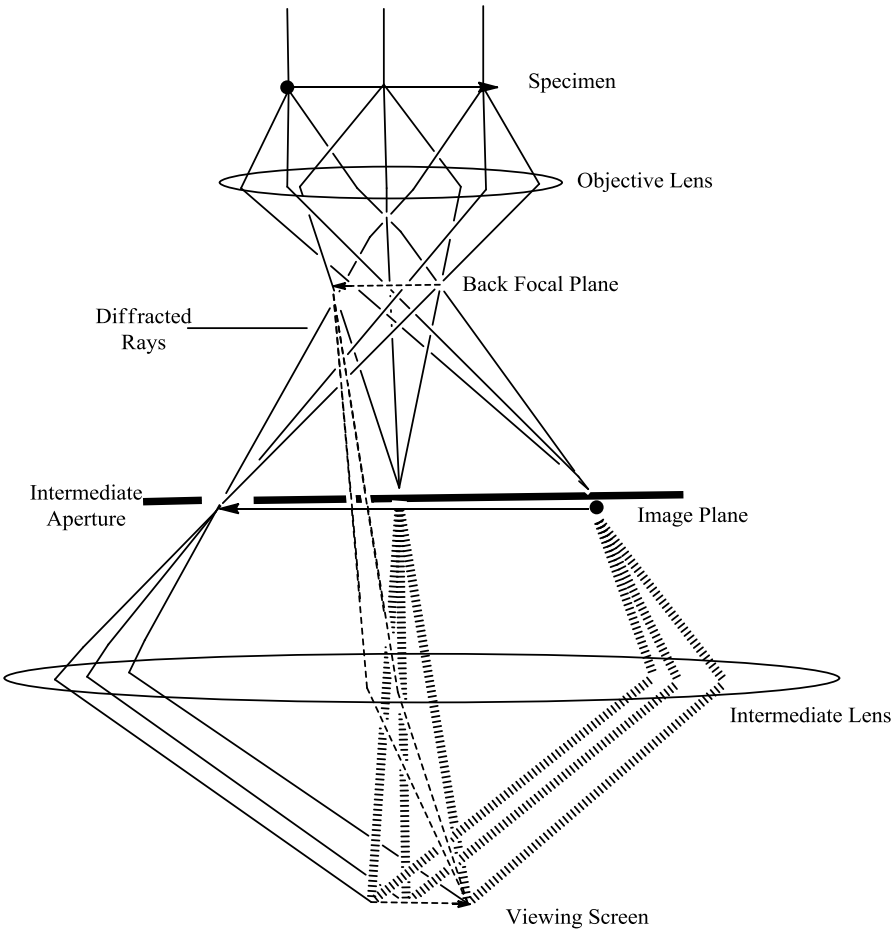

Figure 2.8 Ray diagram of selected area diffraction mode, adapted from Fultz.[65] The dashed lines represent the actual direction of diffracted and transmitted rays if they were not blocked by the intermediate aperture. The dotted line shows artificial rays that define the final image plane of the diffraction patterns from the back focal plane of the objective lens.

2.2.2.2 Energy Dispersive Spectroscopy (EDS)

An EDS detector on a TEM enables the chemical analysis of an imaged sample. The EDS technique utilizes the fact that, when a beam of electrons strikes a sample, X-rays characteristic of the constituent elements in the sample under investigation are produced, as shown in **Figure 2.5**. In brief, X-rays are generated via ionization of electrons from the inner shell of atoms

followed by a transition of an electron from an outer shell to the hole generated in the inner shell, just as is used in an X-ray source for PXRD. These electronic transitions are associated with specific energies, depending on the atom, giving rise to X-rays of characteristic wavelength. Thus, the energy of the X-rays emitted gives information about the elemental composition of the sample under investigation and the intensities of the X-rays generated as a function of energy provides information about the relative amount of each element in the sample. The X-rays generated from the sample are collected via a solid-state semiconductor detector. Electron-hole pairs are generated when the X-ray photons hit the detector, which are then converted to a charge pulse and finally to a voltage pulse with the help of a charge-to-voltage converter.[65]

In this dissertation study, EDS is obtained in a JEOL 2010 transmission electron microscope with a coupled EDS detector (EDAX Inc). EDAX genesis software 1.0 was used as the analysis software in order to detect the relative atomic percentages of elements present in the sample.

2.2.3. Thermogravimetric Analysis (TGA) and Differential Scanning Calorimetry (DSC)

Thermogravimetric analysis is a technique that records changes in weight of a sample as a function of temperature. This technique is useful for investigating the thermal stability (decomposition/desorption of species, oxidation) of a material. The process involves placing 5-20 mg of sample in a pan made of alumina or platinum, attached to a hanger, which in turn is suspended from a microbalance. A furnace (inbuilt) is placed close to the pan and heats the sample. The furnace is usually covered by a glass cover and its temperature is regulated by software, which also provides the weight change versus temperature plot. A wide range of gases can be used during the analysis, including inert gases (Ar/N_2), oxidizing gas (air or O_2) or reducing gas (H_2) depending upon the experimental requirement.

Differential Scanning Calorimetry (DSC) is another thermoanalytical technique. DSC measures the amount of heat absorbed or released from a material as a function of temperature. This measurement also provides information on the physical and chemical changes that occur as the material is heated. In this technique, along with the desired sample, a blank crucible is run to provide a baseline. Both the sample and reference pan are placed in either a platinum or alumina crucible and then the furnace is placed close to the pan, as in TGA. The temperature is regulated with the help of software.

In my dissertation study, TGA was performed using a Perkin Elmer, Pyris 1 TGA. Samples were heated under nitrogen flow from 25 to 700 °C in a ceramic crucible with a temperature ramp rate of 10 °C/min. DSC was performed using a DSC 404 C from NETZSCH. The samples were heated under a nitrogen atmosphere from 20 to 1000 °C with a ramp rate of 10 °C/min in a ceramic boat fitted with a lid.

2.2.4. Surface Area Analysis and Pore Size Distribution

It has long been known that porous solids intake large volumes of condensable gases. In 1777, Fontana observed that freshly calcined charcoal adsorbs various gases in quantities several times more than its own volume; but the volume of gas adsorbed varies from one charcoal sample to other, depending upon the area exposed.[66] Thus, measurements on adsorption of gases provide useful information regarding the surface area of a material.

The term “adsorption” implies condensation of gases on exposed solid surfaces whereas “absorption” is a process where gases penetrate into the solid. In adsorption, the force developed at the surface of the solid (adsorbent) attracts the adsorbate (usually gas or vapor) and these forces of attraction between the adsorbate and the adsorbent are either physical or chemical in

nature. In physical adsorption (physisorption), the force of attraction is mainly Van der Waals in nature, whereas in chemical adsorption (chemisorption), it is covalent.[34, 67]

In a surface area analysis experiment, the sample under investigation is placed in a special tube and heated under vacuum or under nitrogen flow for several hours to remove adsorbed contaminants or moisture from the surface and pores of the sample. After the heating step, the sample is cooled to room temperature. The next step is the analysis step, where the sample tube is transferred to an analysis port, and cooled down to liquid nitrogen temperature (77.2 K). An inert gas like N_2 or He is used as an adsorbate, which is then introduced in the sample tube in small quantities. The adsorbate is introduced continuously until the pressure in the tube reaches equilibrium. Meanwhile, the change in the pressure of the gas is also recorded. The quantity of gas adsorbed can be calculated by employing the basic gas laws, knowing the volume of the tube and mass of the sample. A plot of the volume of gas adsorbed (in cm^3/g, STP) versus the relative pressure, P/P_o (where P = actual pressure and P_o = saturation pressure) is called an adsorption isotherm, and is usually conducted isothermally (77.2 K).

An isotherm curve consists of two parts: adsorption and desorption curves. The adsorption curve is acquired when the adsorbate (inert gas molecules) adsorbs onto the surface of the adsorbent leading initially to monolayer formation of gas molecules. At somewhat higher pressure several layers deposit leading to multilayer formation of gas molecules and then at relatively high pressures capillary condensation occurs. The desorption curve occurs when the inert gas molecules are removed from the surface by evacuation and a hysteresis loop is observed when the desorption curve fails to follow the adsorption curve path. Both the isotherm curve as well as the hysteresis loop provides useful information; the former gives information about the surface area and porosity while the latter gives information about the pore structure and

geometry. In general, the isotherms are grouped into six classes (**Figure 2.9**).[66] Type I is indicative of the presence of small pores, micropores (< 2 nm), Types II and IV are curves consistent with large pores, mesopores (2-50 nm) and macropores (> 50 nm). Types III and V occur when the adsorbate has greater attraction for itself over the solid surface. Finally, the Type VI isotherm is indicative of layer by layer adsorption on a highly uniform surface.

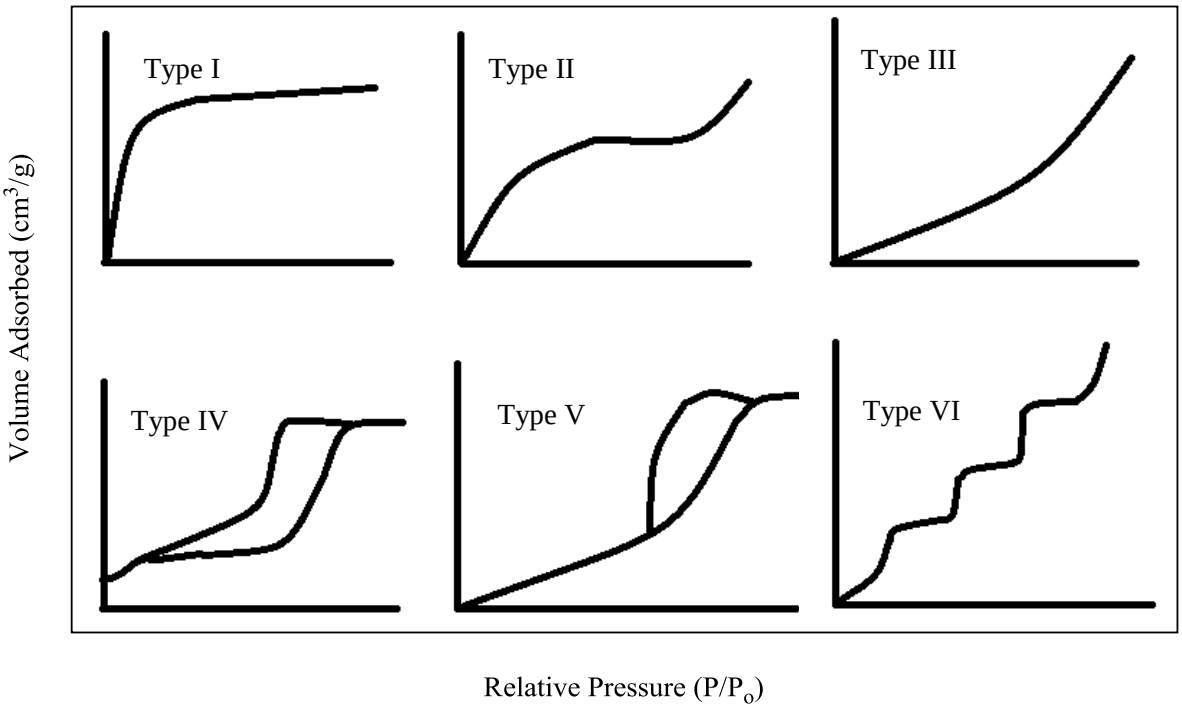

Figure 2.9: Six basic types of adsorption isotherm, adapted from Webb and Orr.[66]

The surface area and pore size distribution are obtained using theoretical models, such as the Langmuir, and the Brunauer, Emmett and Teller (BET) models. The Langmuir model usually applies to chemisorption phenomenon, assuming one monolayer of adsorbate on an adsorbent, whereas BET theory assumes multilayer adsorption of adsorbate.[66, 67] The BET method presumes that the adsorption on the solid surface occurs via physisorption and that there is no interaction among the adsorbed layers. The linear expression of the BET theory is shown in equation 2.7[66, 67]

$$\frac{P}{V_a(P_o - P)} = \frac{1}{V_m C} + \frac{C-1}{V_m C}\left(\frac{P}{P_o}\right) \qquad (2.7)$$

In equation 2.7, P/P_o = relative pressure, V_a = volume of adsorbed gas at a given relative pressure, V_m = volume of gas required for monolayer coverage and C = constant.

Barett, Joyner and Halenda developed a method (BJH) to determine the pore structure, pore size and pore volume of a sample. It is a modified Kelvin equation where, as the pressure is decreased, the condensed adsorptive is desorbed in a stepwise manner. This removal signifies a volume of pores being emptied. It also assumes that all the pores are cylindrical in nature. For computing the BJH pore size distribution in a sample, equation 2.8 is used.[66, 67]

$$\ln\frac{P^*}{P_o} = \frac{2\gamma v cos\theta}{RTr_m} \qquad (2.8)$$

In equation 2.8, P* = critical pressure condensation, P_o = saturation pressure, γ = liquid surface tension, ν = molar volume of condensed gas, θ = contact angle between condensed adsorptive and solid surface, R = gas constant, T = absolute temperature and r_m = mean radius of curvature of the liquid meniscus.

In this dissertation study, for the measurement of surface area and pore structure of aerogels and xerogels, an ASAP 2010 porosimeter and TRISTAR II 3020 from Micromeritics was used with nitrogen as the probe gas. The samples were degassed at 150 °C for 24 h before analysis under 500 mm Hg vacuum for ASAP 2010 and for TRISTAR, the samples were purged with nitrogen gas for 24 h at 150 °C. The surface area was evaluated using the BET method, whereas the pore size was calculated by the BJH adsorption method.

2.2.5. Infrared Spectroscopy (IR)

IR spectroscopy is a widely used technique for probing the presence of organic functional groups. This technique involves passing infrared radiation of increasing wavelength through a

sample so that the radiation characteristic of functional group(s) in the sample is absorbed while the non-characteristic radiation is transmitted. The absorbed radiation corresponds to the fundamental vibration frequency of the atoms in the molecule. But only those absorptions that cause a change in the dipole moment of the molecule show peaks in the IR spectrum. Most organic functional group absorbs IR radiation in the region 4000-600 cm^{-1}.

In my dissertation study, a Varian FTS 3000 MX FTIR spectrometer was used to probe surface organic groups on sample surfaces. Powdered samples were ground with KBr and pressed into a transparent pellet in a 13 mm die with 2000 psi pressure from a Carver Hydraulic pellet press.

2.2.6 Thermoelectric Property Measurements

All measurements consisting of the Seebeck coefficient (S), the electrical resistivity (ρ), the thermal conductivity (κ) and Hall coefficient were performed at Michigan State University. A brief description is included here for completeness.

2.2.6.1 Seebeck Coefficient

The Seebeck coefficient (S), as mentioned in Chapter 1, is the ratio of the voltage difference (ΔV) that develops as a function of a temperature difference (ΔT) across a sample (equation 2.9).

$$S = \frac{\Delta V}{\Delta T} \qquad (2.9)$$

The technique used for the measurement of S is called the Steady State technique.[68] For this dissertation study, S is measured in the low temperature region from 80 K to room temperature, in a continuous flow cryostat under vacuum. Liquid N_2 is used as a refrigerant. The set up used for measuring S is shown in **Figure 2.10.** The samples were first, hot pressed between 350 °C and 380 °C under a pressure of 60MPa for 15min to form a dense pellet. After hot pressing, a

rectangular parallelepiped of the sample with dimensions approximately 2.4 mm × 2.4 mm × 8 mm is cut out of the pellet. The sample is then attached to a copper base using conducting silver epoxy. A resistor of 800 Ω wrapped in a copper foil, which acts as a mini-heater, was attached to the top of the sample. This generates the temperature gradient for measurement of S. To the middle of the sample, two copper-constantan thermocouples were attached in order to measure the temperature difference. The copper leads of the thermocouples simultaneously measure the difference in voltage (V^+ (S) and V^- (S)).

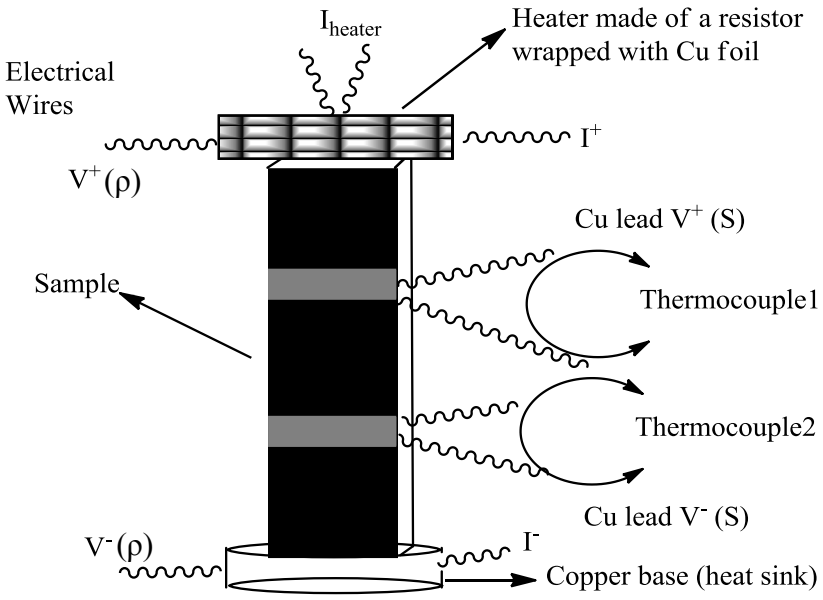

Figure 2.10 Pictorial representation of the set-up used for Seebeck coefficient, electrical resistivity and thermal conductivity measurements (done at MSU) adapted from reference 5.[68] The measurements were done over a temperature range of 80-380 K under vacuum using a steady state technique in a continuous flow cryostat with liquid nitrogen as a refrigerant.

2.2.6.2 Electrical Resistivity Measurements

The standard four-point method is used to measure the electrical resistivity (ρ) of the sample.[68] The measurement can be carried out in parallel along with the S measurement with the

use of the same set up in the cryostat. Briefly, after switching off the mini-heater, current is applied from one set of leads (I^+ and I^-) and voltage is measured from another set of leads (V^+ (ρ) and V^- (ρ)). Finally, Ohm's law is applied to calculate the electrical resistivity as shown in equation 2.10 and 2.11.

$$R = \frac{V}{I} \qquad (2.10)$$

$$\rho = \frac{RA}{l} \qquad (2.11)$$

In equations 2.10 and 2.11, A is the cross sectional area of the sample and *l* is the length of the sample. There are several factors that must be kept in mind while doing the measurement of ρ. Usually, large S values are observed for TE materials, therefore the total voltage measured across the sample is the sum of Seebeck voltage, $\Delta V = S\Delta T$, and resistive voltage, V_{IR}, as shown in equation 2.12.

$$V_{total} = V_{IR} + S\Delta T \qquad (2.12)$$

Due to the large contribution from the Seebeck voltage, often ΔV becomes similar to V_{IR} ($\Delta V \sim V_{IR}$). In order to reduce the effect of Seebeck induced voltage, measurements should be completed in a very short time (less than five seconds). Also, it is usually better to use current acquired in both negative and positive directions (AC resistance bridge or DC current) in order to subtract the Seebeck voltage contribution, as shown in equation 2.13:

$$V_{IR} = \frac{V(I^+) + S\Delta T - [V(I^-) + S\Delta T]}{2} \qquad (2.13)$$

2.2.6.3 Thermal Conductivity Measurements

The same setup in **Figure 2.10** was used for measuring thermal conductivity. The mini-heater was used to generate heat, which passes through the sample. A constant power is

maintained from the heater. The temperature was recorded with the help of the thermocouples separated by a distance (*l*). The thermal conductivity can be calculated by using equation 2.14.[68]

$$\kappa = \frac{\mathrm{VI} \times l}{\Delta \mathrm{T} \times \mathrm{A}} \qquad (2.14)$$

VI is the heater power, *l* is the probe separation between the two thermocouples, ΔT is the temperature difference between the thermocouple and A is the cross-sectional area.

2.2.6.4 Hall Coefficient Measurement

The electrical conductivity, σ, is the inverse of the resistivity, ρ and depends on the carrier concentration, n of a material as shown in equation 2.15, where e is the electronic charge (1.602×10^{-19} C) and μ is the carrier mobility. Optimized carrier concentrations are essential for maximizing σ and also impact S as shown in equation 2.16, where K_B = Boltzmann constant, h = Planck's constant, m* = effective mass of the carrier and T = absolute temperature.[68]

$$\sigma = \mathrm{ne}\mu \qquad (2.15)$$

$$\mathrm{S} = \frac{8\pi^2 \mathrm{K_B^2}}{3\mathrm{eh}^2}\ \mathrm{m}^*\mathrm{T}\left(\frac{\pi}{3\mathrm{n}}\right)^{\frac{2}{3}} \qquad (2.16)$$

The set up for the measurement of Hall coefficient (R_H) is shown in **Figure 2.11.** In this experiment, a thin slab of sample, approximately 1 mm in thickness, cut from the hot pressed sample, was used. A series of voltage and current leads are used to measure the Hall resistance (R_{xy}), shown in **Figure 2.11**.

When a magnetic field is applied perpendicular (z axis) to the direction of current (x axis), moving charge carriers experience a force called the Lorenz force, given by F=QVB, where Q is the charge on moving particles, V is the velocity of moving particles and B is the applied magnetic field. This leads charge carriers to accumulate across opposite faces of the

parallelepiped sample. This charge separation generates the electric field and hence the voltage difference across the opposite faces of the sample (y axis). The carrier concentration in the sample is thus measured by using equation (2.17).

$$R_H = \frac{E_y}{j_x B_z} = \frac{V_y\, t}{I_x B_z} = \frac{R_{xy}\, t}{B_Z} = -\frac{1}{ne} \qquad (2.17)$$

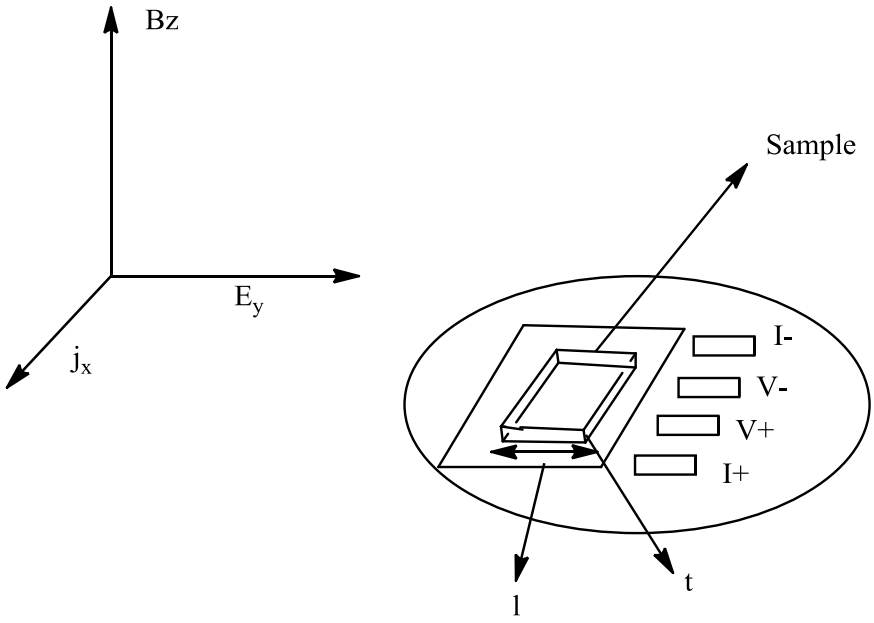

Figure 2.11 Pictorial representation of the set up and wiring for the Hall coefficient measurements.

In equation 2.17, B_z is the magnetic field along the z axis; j_x is current density along the x axis which is equal to I_x/A (where I_x is the current along the x axis and A is the area of the slab, given by $A = l \times t$, where l is length and t is thickness of the slab); E_y is the induced electric field along the y axis where $E_y = V_y/l$ (where V_y is the voltage along the y axis and l is the length of the slab); and e is the electronic charge (1.602×10^{-19} C). For this dissertation study, the Hall coefficient was measured in the same temperature range (60 K to 400 K) using AC current in a

varying magnetic field from -3 T to 3T in the Quantum Design Versalab system. In order to eliminate complications from anisotropy, all transport properties were measured in the direction perpendicular to the pressing axis.

Chapter 3

Toward nanostructured thermoelectrics: Synthesis and characterization of lead telluride gels and aerogels

3.1 Introduction

As mentioned in Chapter 1, nanoscale lead chalcogenides (PbS, PbSe and PbTe) have gained considerable attention from the scientific community due to their high degree of quantum confinement and specifically for their application in thermal energy conversion devices.[69] This Chapter is focused on the extension of the sol–gel method developed in our lab for lighter sulfides and selenides to tellurides;[45, 47] specifically, synthesis of PbTe aerogels (by supercritical fluid drying) and xerogels (by bench top drying) with nanostructured features of potential benefit for enhanced thermoelectrics. The effect of particle size and shape as well as the chemical oxidant on the gelation process, and the consequent morphology and surface area characteristics, will be discussed. Because these materials are potential candidates for thermoelectrics, the thermal stability of the gels relative to the precursor nanoparticles, as probed by in situ TEM and DSC, and the desorption temperature of the surface organic ligands as determined by TGA, will also be presented. This work has been published as a full paper in the *Journal of Materials Chemistry, 2011*.[70]

3.2 Experimental

3.2.1 Materials

Lead acetate trihydrate ($Pb(OAc)_2 \cdot 3H_2O$) was obtained from Baker Chemicals; tellurium powder (Te, 200 mesh, 99.8 %), 4-fluorothiophenol (4-FPhSH, 98 %), 1-octadecene (ODE, technical grade 90 %) and tetranitromethane (TNM) were obtained from Aldrich; trioctylphosphine (TOP, technical grade 97 %) was obtained from Strem chemicals;

triethylamine (TEA, reagent grade), oleic acid (OA, technical grade, 90 %), and 3 % aqueous H_2O_2 were obtained from Fisher.

3.2.2 Synthesis of PbTe Oleate-Capped Nanoparticles

PbTe nanoparticles were prepared by combining $Pb(OAc)_2 \cdot 3H_2O$ (1.317 g, 3 mmol) with OA (3 mL, 6 mmol) and ODE (6 mL, 18 mmol) and heating this mixture under inert atmosphere on a Schlenk line at 170 °C for 30 min to obtain a colorless solution. The temperature of the solution was then reduced to 150 °C followed by rapid injection of 3 mmol of 1 M TOPTe. The resultant solution was left at 150 °C for 3 or 5 min of growth time and then the reaction was quenched by plunging the flask into a cold-water bath. In order to obtain larger size nanoparticles, the growth time was increased to 10-15 min. The resultant nanoparticles were precipitated by adding hexane as the solvent and acetone as the antisolvent and isolated by centrifugation.

3.2.3 Synthesis of PbTe Thiolate-Capped Nanoparticles and Gelation

For generation of thiolate-capped nanoparticles, 4-FPhSH (1.2 mL, 15 mmol) and TEA (2.4 mL, 15 mmol) were quickly injected to the oleate-capped lead telluride nanoparticles generated at 150 °C just prior to quenching. The 4-FPhS^- capped lead telluride nanoparticles were precipitated by addition of toluene, followed by centrifugation. The obtained black product was further washed with additional toluene. The thoroughly-washed thiolate-capped nanoparticles were then dispersed in 15 mL of methanol for gelation.

Gelation was induced by addition of 0.1 mL of 3 % TNM in methanol (v/v), or 3% aqueous H_2O_2, into 5 mL aliquots ($[Pb^{2+}]$ = 0.2 M) of thiolate-capped PbTe sol. The concentration was calculated based on the moles of precursor lead acetate. The solution was shaken and gelation was observed within 1 h. The wet gels were aged for 4-5 days under ambient conditions and then were exchanged with acetone twice a day for another 2 days. A portion of the wet gel was

transferred to porous capsules and supercritically dried, as described in Chapter 2, to produce an aerogel; a second portion of the wet gel was bench-top dried at ambient temperature and pressure to give a xerogel.

3.3 Characterization Techniques

PXRD, TEM, IR, BET surface area and BJH and pore size distribution, TGA and DSC were used to characterize the materials. For more details on the measurement techniques, refer to Chapter 2.

3.4 Results and Discussion

3.4.1 Synthesis of PbTe Nanoparticles, Aerogels and Xerogels

The synthesis of the PbTe nanoparticles employed in the sol–gel assembly was adapted from Murphy and coworkers[37] with minor variations in the ratios of precursors used and also in the temperature of reaction. The method involves the injection of TOPTe, which is the anion monomer, into a mixture of lead acetate trihydrate, OA and ODE maintained at high temperature. A growth time of 3 min and 5 min was employed, followed by quenching of the reaction and isolation using hexane as the solvent and acetone as the precipitating antisolvent and subsequent centrifugation. Thiolate capping was achieved by adding 4-FPhSH and TEA to the 150 °C PbTe reaction mixture immediately after the 3 or 5 min reaction times, followed by quenching of the reaction with a water bath. The nanoparticles obtained were further washed with toluene twice. The resultant nanoparticles obtained were black in color.

Gelation was achieved by dispersing the thiolate-capped nanoparticles in methanol followed by addition of oxidizing agent, 0.1 mL of 3 % TNM to oxidize, and hence remove, the surface bound thiolate groups, yielding wet gels within 1 h. The wet gels were aged for 4-5 days under ambient conditions and then exchanged with acetone to remove the byproducts of gelation. Gels

were transferred carefully to porous capsules and supercritically dried using CO_2 to give an aerogel (as mentioned in Chapter 2), or left in vials and bench top dried under ambient temperature and pressure to give a xerogel. The resultant gels were black in color, like the nanoparticles from which they originated, and were obtained as powders.

3.4.2 Characterization: Oleate-Capped PbTe Nanoparticles

Representative PXRD patterns of PbTe oleate-capped nanoparticles obtained after a growth time of 3 and 5 min are shown in **Figure 3.1**. In both cases, the patterns match with the Altaite phase (thermodynamically stable cubic phase) of PbTe, with the shorter growth time resulting in broader peaks. Application of the Scherrer equation yields values of 8.4 nm and 15 nm, based on the breadth of the (200) reflection, for 3 and 5 min growth time, respectively. TEM was employed to verify size and determine the morphology and polydispersity of PbTe nanoparticles. As shown in **Figure 3.2a**, the nanoparticles obtained after a growth time of 3 min were found to be spherical in shape with an average particle size of 9.01 ± 0.36 nm, whereas nanoparticles obtained after a growth time of 5 min (**Figure 3.3a**) were found to be cubic in shape with an average size of 15.8 ± 2.4 nm, measured from the face diagonal. From the results obtained above, it can be concluded that this synthetic route in general can be used to synthesize various nanoparticles with different sizes and shapes. The sizes of the nanoparticles obtained by imaging in the TEM were similar to the crystallite sizes obtained from the Scherrer equation. This observation, along with the observation of lattice fringes in HRTEM images, (**Figure 3.2b** and **Figure 3.3b**), is indicative of the formation of highly crystalline PbTe nanoparticles. Also the transition from spherical to cubic morphology is thermodynamically driven as the size increases, favoring the growth of the (100) facets (lowest total surface energy) leading to the cubic morphology.[37]

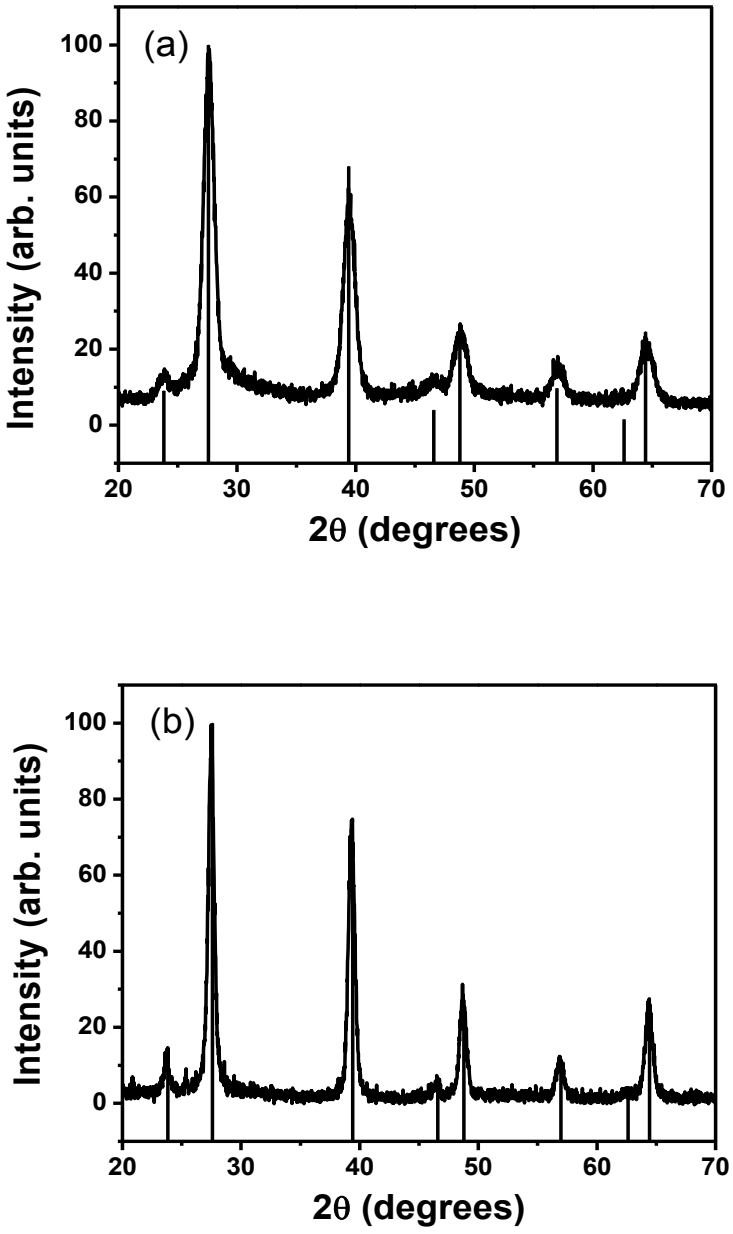

Figure 3.1 PXRD of PbTe nanoparticles obtained after a growth time of (a) 3 min and (b) 5 min. The vertical lines correspond to the ICDD-PDF # 38-1435 of cubic PbTe (Altaite).

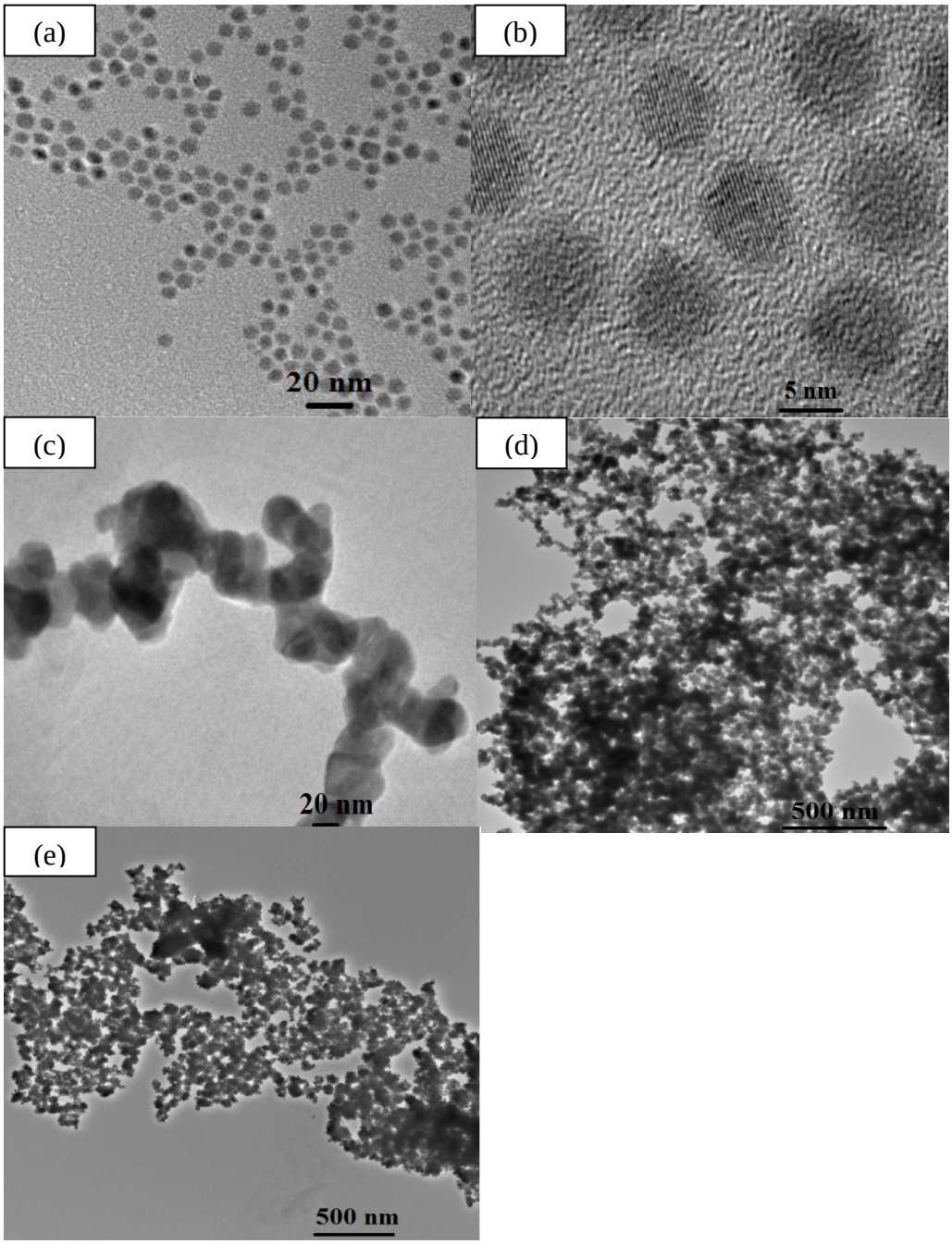

Figure 3.2 TEM images of PbTe nanoparticles prepared after a growth time of 3 min showing (a) oleate-capped nanoparticles, (b) HRTEM showing lattice fringes on oleate-capped nanoparticles (c) thiolate-capped nanoparticles, (d) aerogel and (e) xerogel materials.

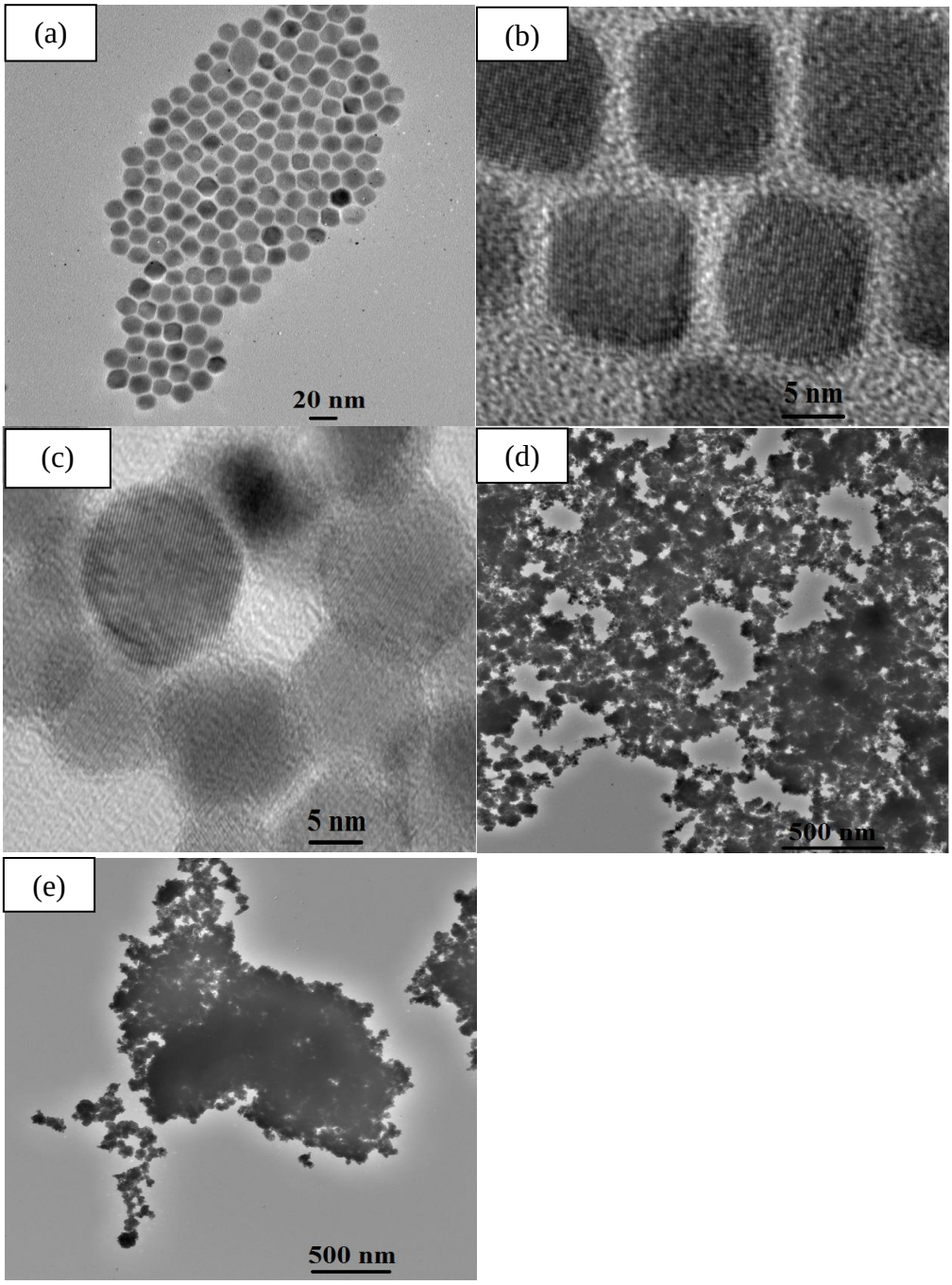

Figure 3.3 TEM images of PbTe nanoparticles prepared after a growth time of 5 min showing (a) oleate-capped nanoparticles, (b) HRTEM showing lattice fringes on oleate-capped nanoparticles, (c) thiolate-capped nanoparticles, (d) aerogel and (e) xerogel materials.

Semiquantitative Energy Dispersive Spectroscopy (EDS) conducted in the TEM suggests the Pb:Te ratio for spherical- and cube-shaped particles, is close to the ideal value of the expected composition (Pb:Te = 1:1) (**Table 3.1**).

Table 3.1 Elemental composition of spherical and cubic shaped PbTe nanoparticles and resultant gels: oleate-capped, thiolate-capped, aerogel and xerogel samples.

Sample	Elemental Composition		Atomic Ratio Pb:Te
	Pb (%)	Te (%)	
PbTe nanoparticles oleate-capped (spheres)	49.9	50.1	1:1
PbTe nanoparticles thiolate-capped (spheres)	47.9	52.1	0.9:1
PbTe aerogels (spheres)	47.1	52.9	0.89:1
PbTe xerogels (spheres)	48.8	51.2	0.95:1
PbTe nanoparticles oleate-capped (cubes)	48.0	52.0	0.92:1
PbTe nanoparticles thiolate-capped (cubes)	47.9	52.1	0.92:1
PbTe aerogels (cubes)	49.8	50.2	0.99:1
PbTe xerogels (cubes)	49.9	50.1	1:1

3.4.3 Characterization: Thiolate-Capped PbTe Nanoparticles

The PXRD pattern obtained for the thiolate-capped nanoparticles was similar to that of oleate-capped nanoparticles (**Figure 3.4**), inferring no change in the phase or crystallite size of the PbTe thiolate-capped nanoparticles. However, TEM revealed the thiolate-capped nanoparticles to be significantly aggregated, in contrast to the oleate-capped particles (**Figure 3.2c** and **Figure 3.3c**). This is a reflection of the pre-disposition of thiolate-capped PbTe toward

gelation, as spontaneous assembly seems to occur even when no oxidant is intentionally added (adventitious oxygen).

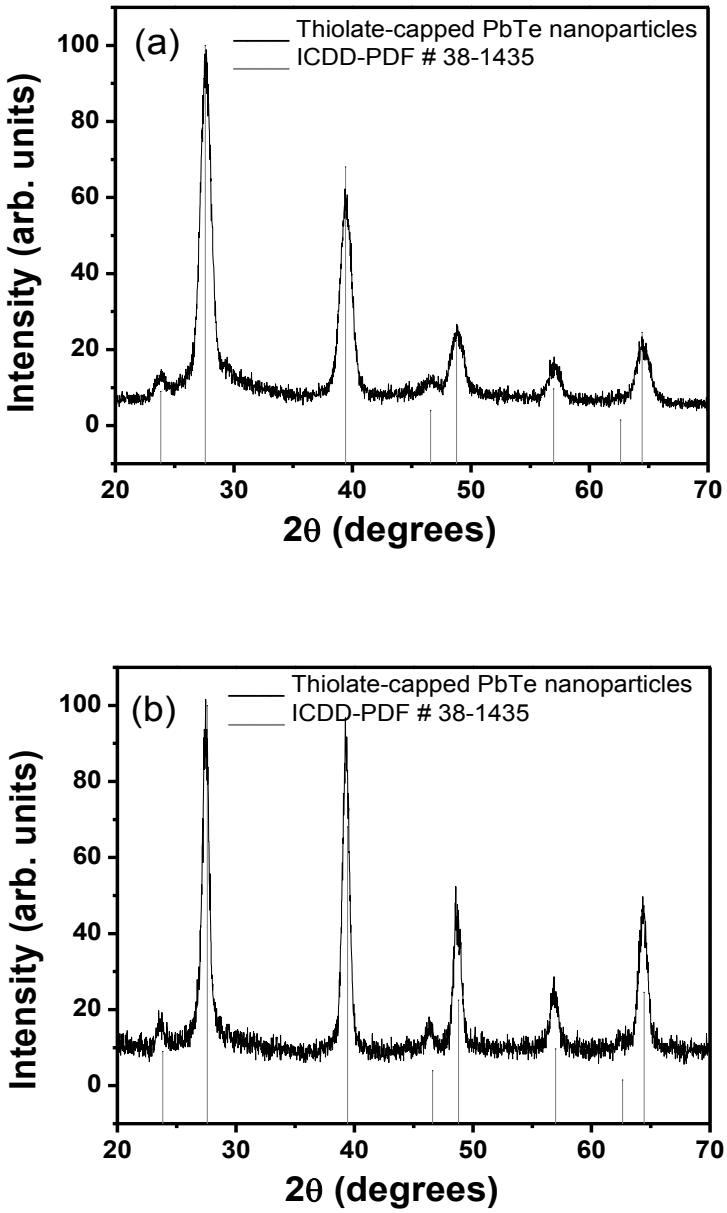

Figure 3.4 PXRD of thiolate-capped PbTe nanoparticles obtained from ligand exchange of nanoparticles prepared using a growth time of (a) 3 min and (b) 5 min. The vertical lines correspond to the ICDD-PDF # 38-1435 of cubic PbTe.

3.4.4 Characterization: PbTe Aerogels and Xerogels

Figure 3.5 shows the PXRD patterns of the aerogel and xerogel samples produced from spherical- and cube-shaped PbTe nanoparticles. These are essentially identical to the patterns obtained from the precursor nanoparticles demonstrating that the crystallite size (**Table 3.2**) and structure are maintained in the gelation process. From TEM (**Figure 3.2d** and **Figure 3.3d**), the aerogels are found to exhibit a colloidal morphology consisting of an interconnected network of nanoparticles and pores. In contrast, the xerogels consisted of dense regions with significant fragmentation (**Figure 3.2e** and **Figure 3.3e**). This is attributed to the collapse of the network from the surface tension that arises in the ambient temperature drying. EDS data is consistent with the expected 1:1 formulation for Pb: Te in PbTe (**Table 3.1**).

Despite apparent differences in the TEM, the surface area/porosimetry characteristics are fairly similar for aerogels and xerogels. The nitrogen adsorption/desorption isotherms (**Figure 3.6** and **Figure 3.7**) illustrate that the aerogels and xerogels display type IV isotherm curves that are characteristic of a mesoporous material (2-50 nm pore diameter) with a sharp upturn in the high relative pressure region indicating condensation of liquid associated with the presence of macropores >50 nm.[71] The hysteresis loops of the adsorption/desorption isotherms of both the aerogels and xerogels display H1 character corresponding to cylindrical pore geometry in the material.[67] The BJH pore size distribution (**Figure 3.6** and **Figure 3.7** insets) is broad, extending to the macropore region (> 100 nm), suggesting similar pore characteristics for the aerogels and xerogels. However, clear differences are observed when comparing gel materials prepared from spheres vs. cubes (**Table 3.2**); Specifically, the smaller spherical nanoparticles give rise to gels with higher surface areas than the cubes (by a factor of 2-3).

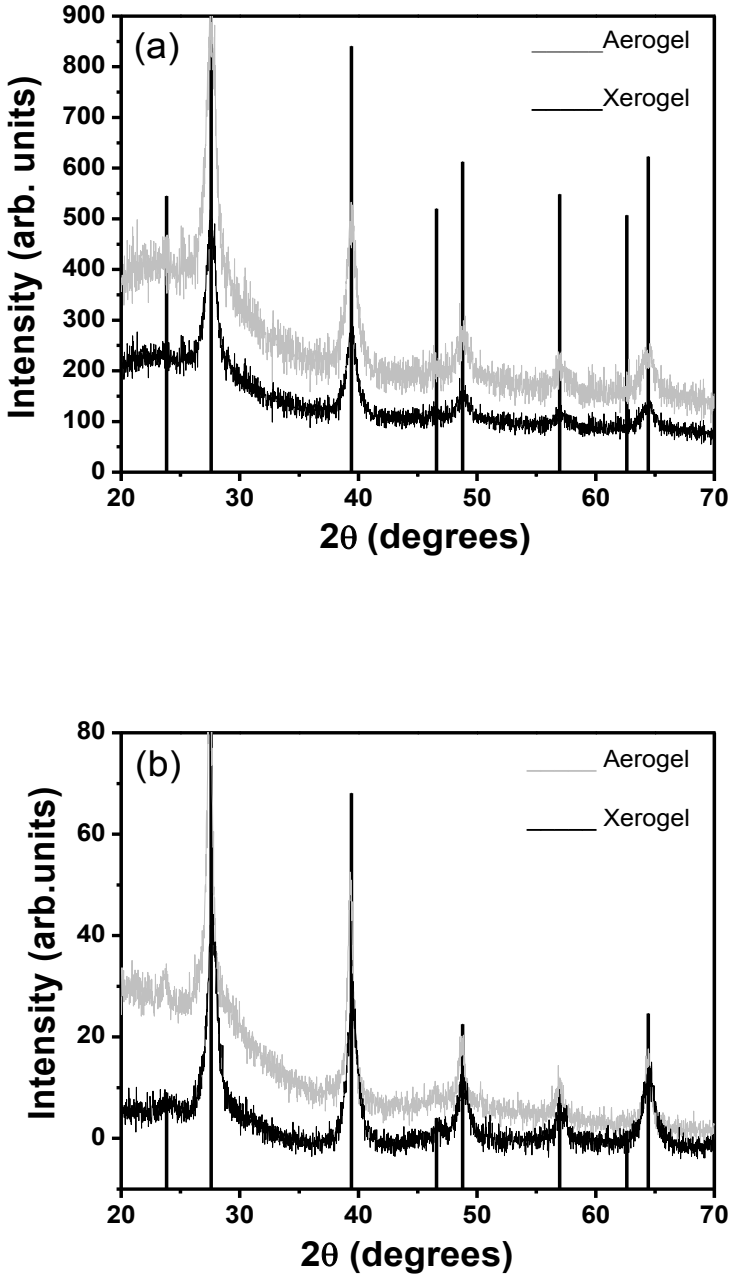

Figure 3.5 Powder X-ray diffraction patterns of PbTe aerogels and xerogels prepared from (a) spherically-shaped, and (b) cube-shaped nanoparticles. The vertical lines correspond to the cubic PbTe phase (ICDD- PDF # 38-1435).

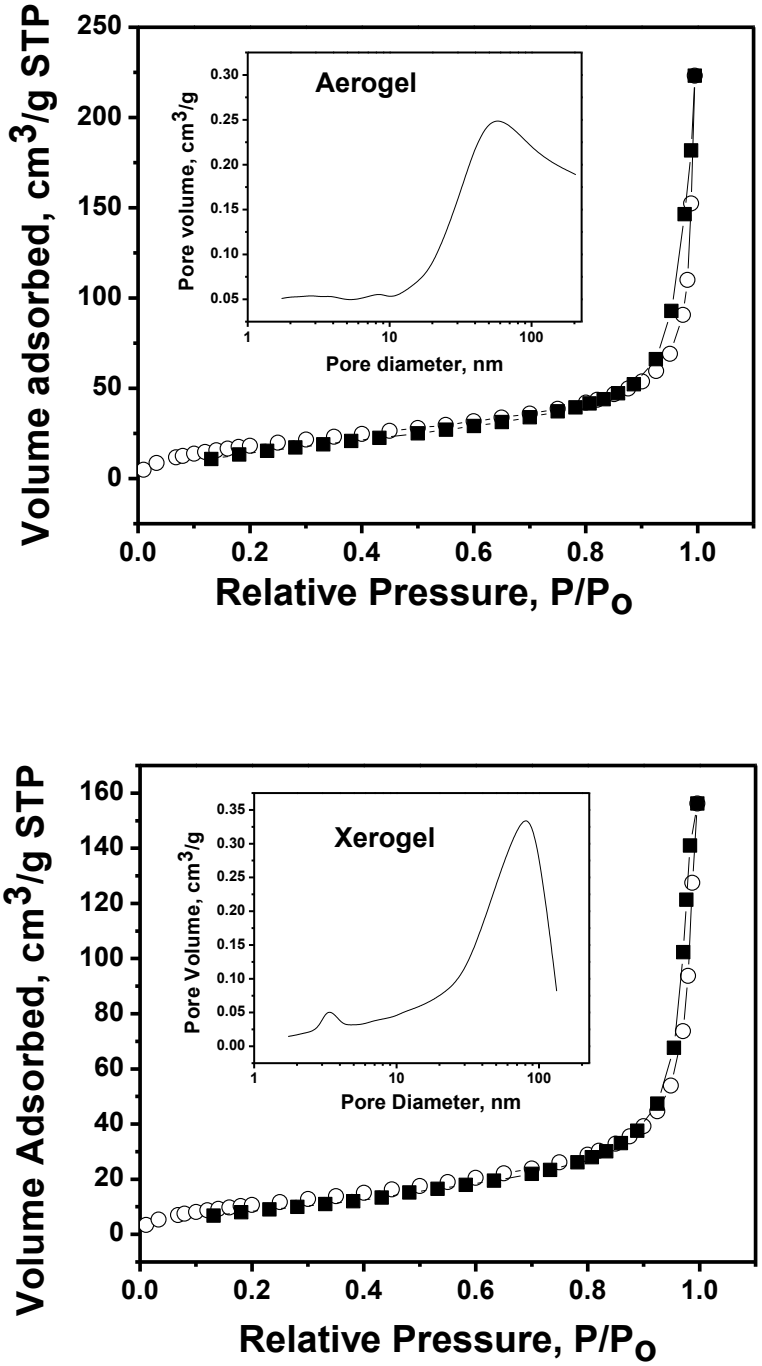

Figure 3.6 N_2 adsorption (○)/desorption (■) isotherms of PbTe aerogels and xerogels assembled from spherical-shaped PbTe nanoparticles; the insets show the corresponding BJH pore size distributions.

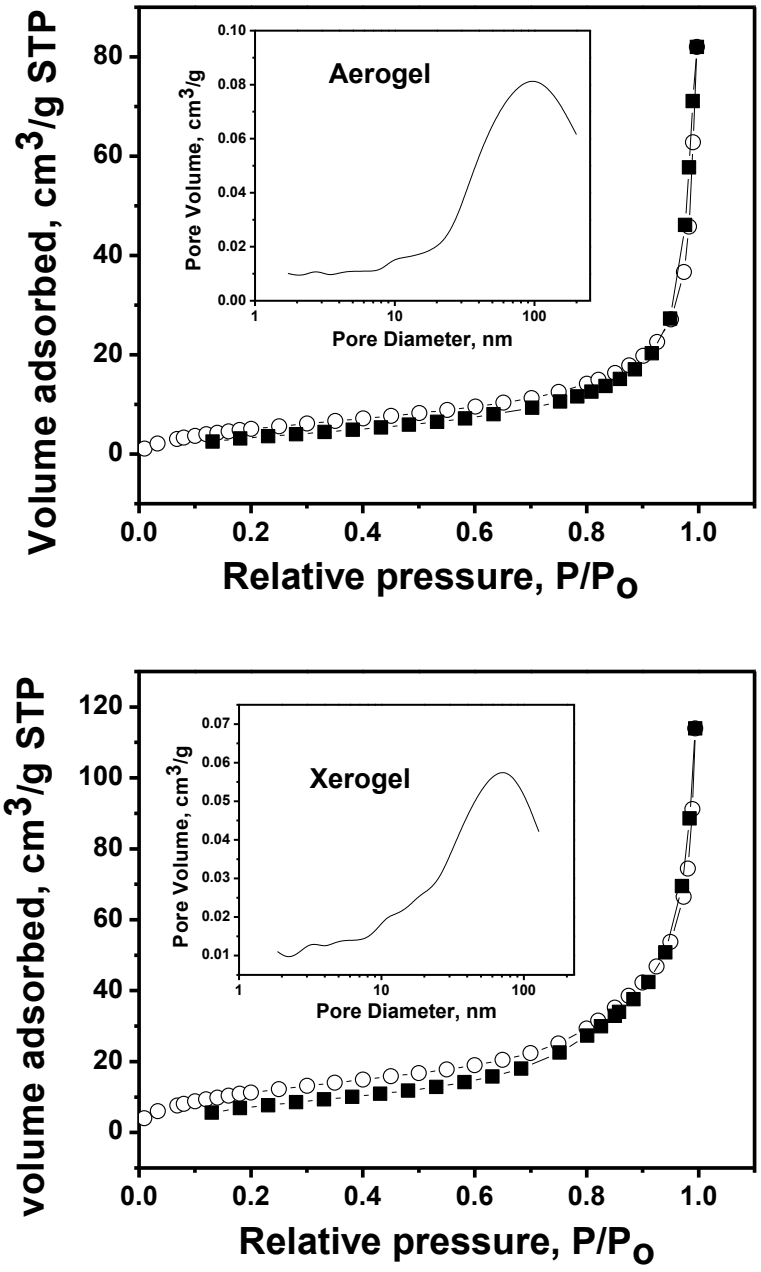

Figure 3.7 N_2 adsorption (○)/desorption (■) isotherms of PbTe aerogels and xerogels assembled from cube-shaped PbTe nanoparticles; the insets show the corresponding BJH pore size distributions.

Table 3.2 PXRD crystallite sizes, BET surface area, theoretical surface area, average pore diameter and cumulative pore volume of aerogels and xerogels obtained from spherical and cube-shaped nanoparticles.

Samples	PXRD Size (nm)	BET surface area (m^2/g)	Theoretical surface area[a] (m^2/ g)	Average pore Diameter (nm)	Cumulative pore Volume (cm^3/g)
PbTe spherical aerogel	8.4	74	81	19	0.34
PbTe spherical xerogel	8.4	43	81	20	0.24
PbTe cubic aerogel	15	24	57	18	0.07
PbTe cubic xerogel	15	28	57	28	0.14

[a]Based on the expected surface area of discrete nanoparticles (spheres and cubes).[67]

One possible reason for the difference between cube and spherically shaped gel materials is the fact that the cubes themselves have a lower theoretical surface area due to their increased size and geometric shape, and are also likely to pack together with fewer void spaces. Supercritical vs. ambient drying appears to have a more profound effect on the surface area of the spheres relative to the cubes, with the aerogels from spheres exhibiting a surface area roughly 90 % of theoretical and nearly twice that of the corresponding xerogels, whereas the cubes result in gels that attain only 50 % of their theoretical surface area, with xerogels being virtually identical to aerogels.

3.4.5 Probing the Thermal Stability of PbTe Nanostructures

The presence of nanoscale interfaces as well as pores in the nanostructures can be beneficial for phonon scattering, yielding improved thermoelectric performance. However, for thermoelectric power generators, materials that operate at elevated temperature are required;[72] thus, thermal stability is a key factor in probing utility. Bulk PbTe has a melting point of 917 °C and a sublimation temperature range of 450-600 °C in vacuum,[72] but since nanoparticles have large surface-to-volume ratios, the physical characteristics of PbTe nanoparticles and aerogels may be quite different. In order to probe the thermal stability of the nanoparticles and aerogels, *in situ* heating experiments on dispersed samples in the TEM, as well as DSC measurements in closed pans, were conducted.

Figure 3.8 shows a series of TEM images obtained during *in situ* heating of the PbTe oleate-capped nanoparticles (size = 12 nm). No change in the image was observed up to 400 °C, but at 405 °C, some of the nanoparticles disappeared (shown by circles), suggesting that the nanoparticles started subliming from the TEM grid. The TEM image obtained at 406 °C showed that most of the nanoparticles have sublimed. Loss of nanoparticles continued to be evident from data at 408 °C and 411 °C, and finally, the TEM image obtained at 413 °C showed all the nanoparticles have disappeared. Based on this data, it can be concluded that the sublimation of the PbTe nanoparticles occurs over a very narrow range, and at a very low temperature, 405-413 °C.

A similar in situ heating experiment was conducted on PbTe aerogels prepared from 12 nm particles. In this case, no change was observed in the aerogels up to 425 °C (Figure 3.9). The inset of the TEM image at 425 °C shows a clear diffraction pattern, detected by selected area electron diffraction (SAED), suggesting the presence of crystalline nanoparticles. The first

changes were noted between 425 °C and 430 °C as nanoparticles started disappearing gradually (see area in the circle). Finally, by 500 °C nearly all the nanoparticles disappeared, consistent with sublimation; SAED reveals an absence of crystalline PbTe (i.e., it is featureless).

From the above *in situ* heating data, it appears that the sublimation temperature onset for nanoparticles and aerogels is lower than that reported by Dughaish for bulk material in vacuum.[72] The consequence of assembly is to retard and broaden the sublimation process such that sublimation started at a higher temperature and occurred over a wider temperature range for aerogels. This can be attributed to the inherent heterogeneity of the aerogels, as well as the fact that the nanoparticles are now embraced in a bonding network, reducing the surface area. Indeed, the sublimation of a heterogeneous mixture of larger size (and therefore reduced surface area) PbTe nanoparticles (ca. 20 nm, prepared using a growth time of 10 min) was not initiated until after 500 °C and was not complete until 700 °C, **Figure 3.10**.

In order to discern the melting temperature of PbTe nanoparticles and aerogels, as well as to evaluate processing conditions for ligand removal, DSC and TGA were acquired (**Figure 3.11**). The DSC of the nanoparticles shows a sharp exotherm at 322 °C and a smaller feature at 397 °C that correlate with weight losses in the TGA between 255-360 °C and 360-455 °C, respectively. These thermal/weight loss events are consistent with loss and/or decomposition of surface organic groups. A subsequent endotherm at 455 °C does not seem to correlate to a weight change event, and we attribute this feature to melting of excess tellurium (Te, mp = 452 °C) present in the sample[73] as confirmed by EDS analysis (**Figure 3.12**). Finally, a sharp endotherm at 918 °C was assigned to the melting of the nanoparticles. This is nearly identical to the bulk melting point of PbTe, suggesting that there is no size effect on melting for these particles, or, more likely, that they sinter together, forming a bulk phase that subsequently melts. Data for the aerogel have

similar features, including a broad exotherm centered at 310 °C that correlates to a weight loss in TGA between 275 °C and 380 °C, associated with the loss of surface bound groups. This overall weight loss is much smaller in the aerogels relative to the nanoparticles (8 vs. 16 %) due to removal of surface ligands during the gel formation step. The aerogel also exhibits endotherms at 420 °C and 920 °C due to the melting of Te impurities and PbTe, respectively.

3.4.6 Effect of Oxidant on Gel Formation

A common problem encountered with the gels is excessive fragility. Indeed, attempts to make monolithic aerogels of PbTe from TNM oxidation were unsuccessful, even when very long gel aging times (10 days) were employed. In order to obtain stronger gels than those routinely prepared from TNM, H_2O_2 was evaluated as an oxidizing agent for gel generation. It was observed that when 3% aqueous H_2O_2 was added to the wet gel in a molar ratio of $[H_2O_2]$: $[Pb^{2+}] = 1 : 6$, gelation was achieved (**Figure 3.13**); but after 1 day of aging, bleaching of the wet gel was evident (the color of the gel changed from black to light brown). In contrast, when 3% aqueous H_2O_2 was incorporated to produce a molar ratio of $[H_2O_2]$: $[Pb^{2+}] = 1 : 11$, gelation was achieved and yielded a black product **(Figure 3.13)**. Based on these data, we hypothesize that H_2O_2, when present in excess, can oxidize tellurium and lead. This was confirmed by PXRD (**Figure 3.14**), which reveals the presence of crystalline Te_2O_5 and Pb_2O_3 in gels prepared from sols with an overall higher concentration of H_2O_2, whereas a pure PbTe phase is obtained with less H_2O_2 (**Figure 3.14**). Unfortunately, H_2O_2 gels showed a similar propensity to fracture. While monolithic gels remain elusive, this experiment demonstrates that oxidizing agents other than TNM, and in particular oxygen-atom transferring oxidants like H_2O_2, can be used for gelation of PbTe nanoparticles without significant oxygen atom incorporation (i.e., Te_2O_5 and Pb_2O_3 formation) provided the oxidant concentration is sufficiently low.

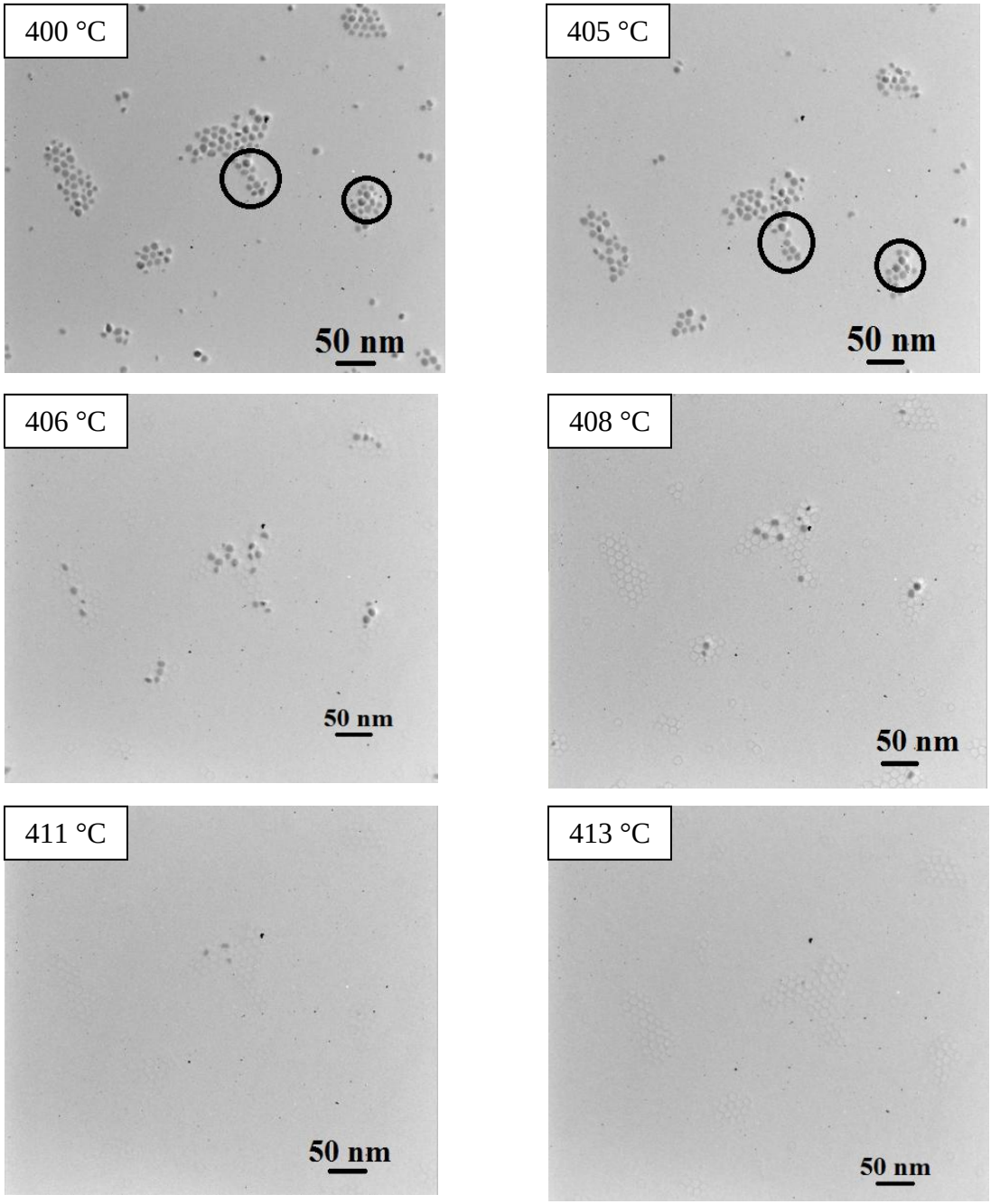

Figure 3.8 TEM images obtained upon heating 12 nm diameter PbTe nanoparticles. The ghost images apparent after sublimation are attributed to the carbonaceous residue from surface organic functionalities on the particles and/or damage to the underlying carbon film.

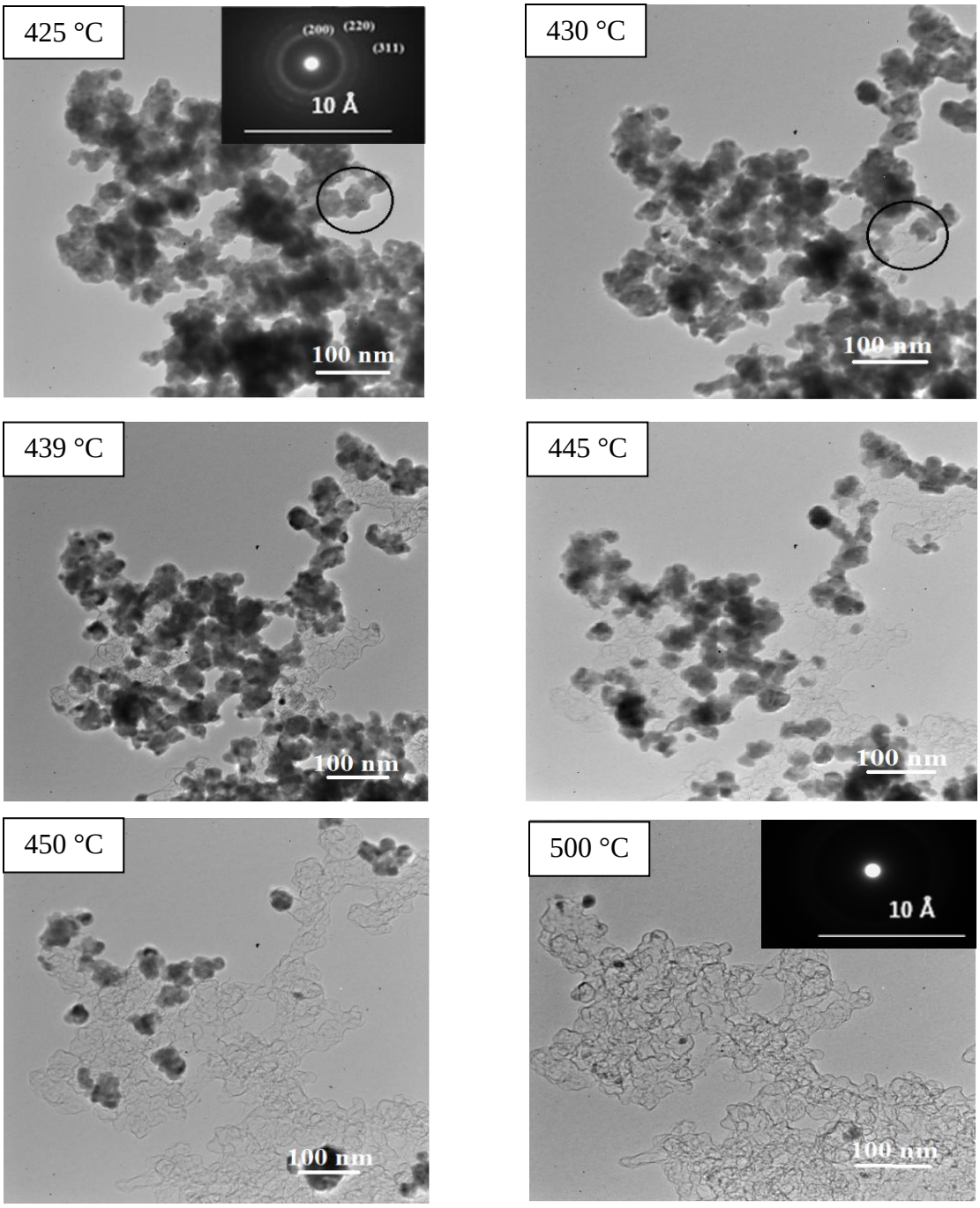

Figure 3.9 TEM images obtained upon heating a PbTe aerogel prepared from 12 nm particles. The insets in the images collected at 425 °C and 500 °C show the selected area electron diffraction (SAED) patterns.

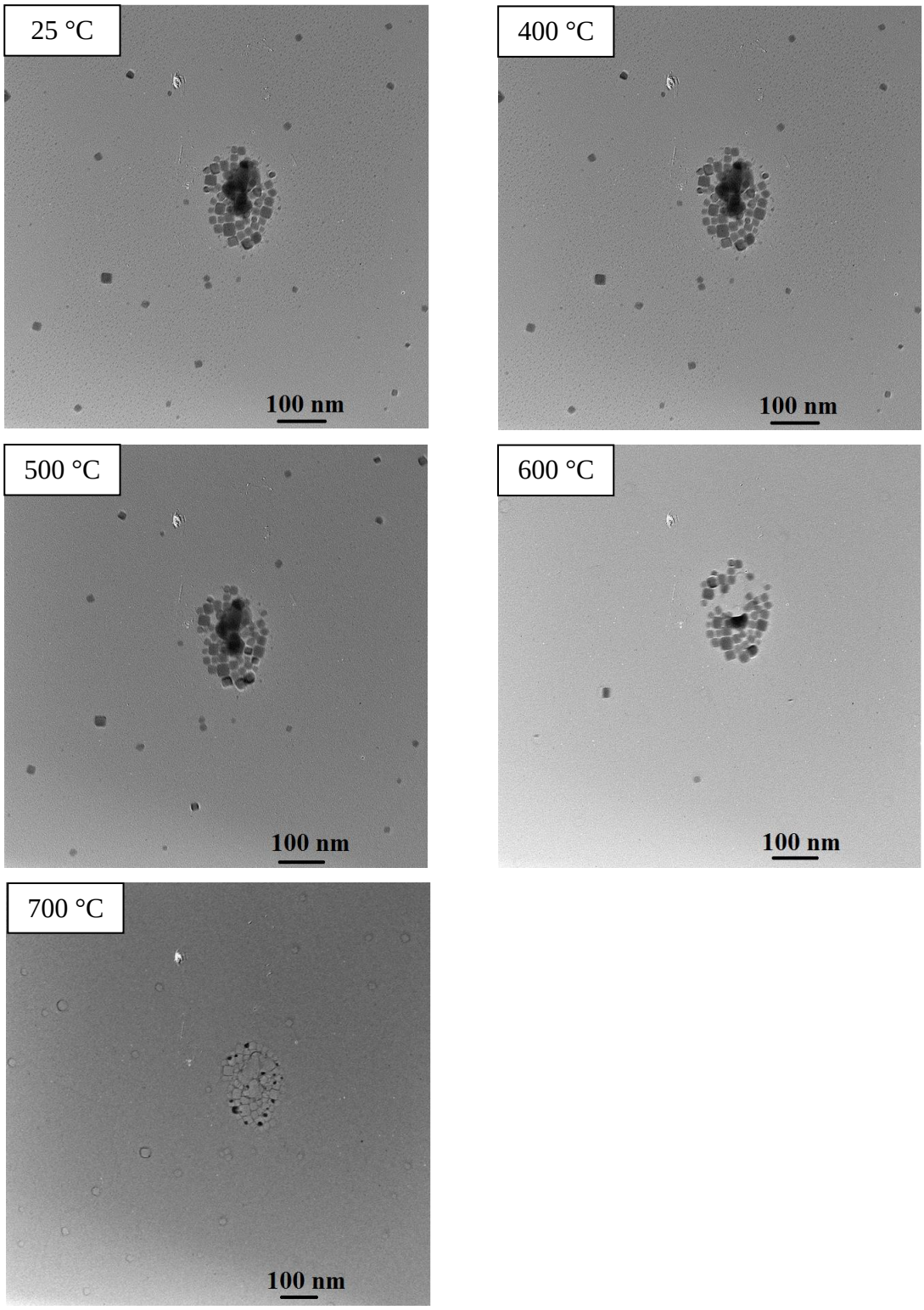

Figure 3.10 TEM images obtained upon *in situ* heating of a sample of PbTe nanoparticles of diameter 20 nm.

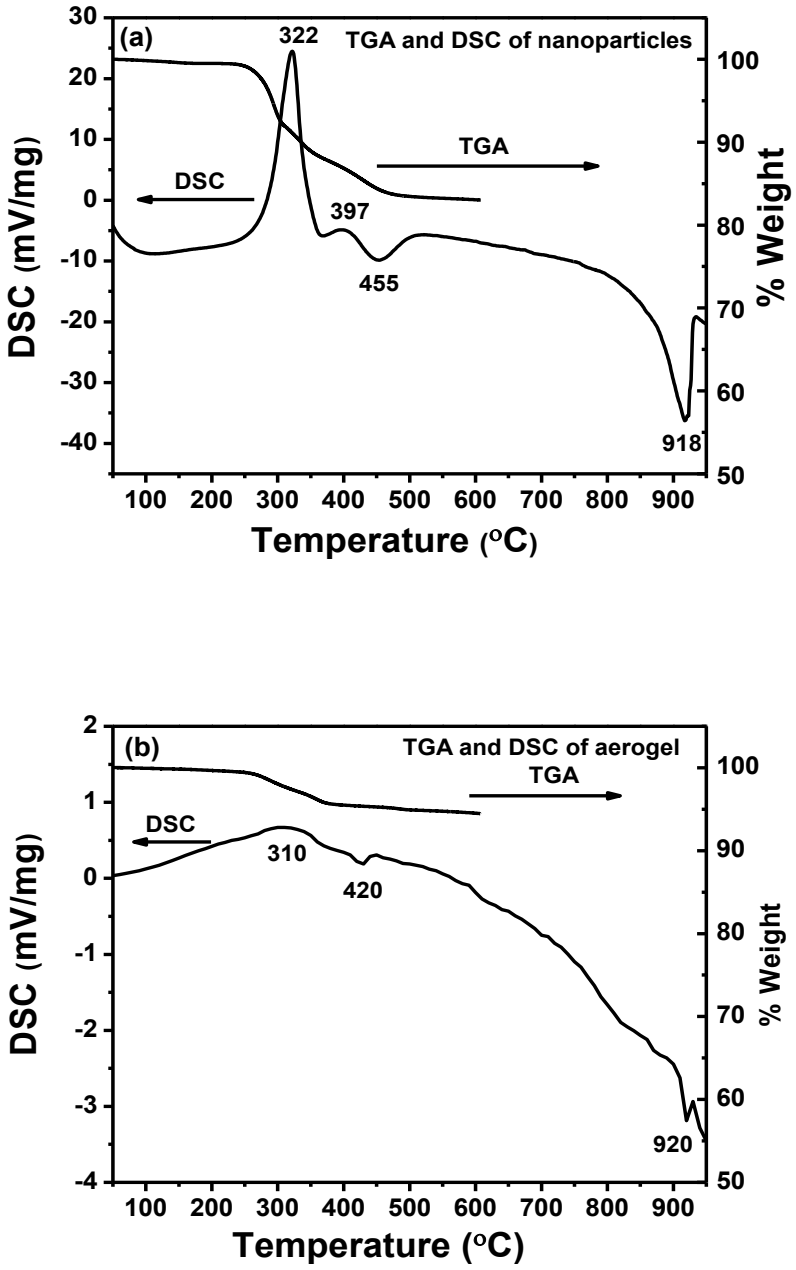

Figure 3.11 DSC and TGA of (a) 12 nm PbTe oleate-capped nanoparticles and (b) PbTe aerogel prepared from 12 nm particles.

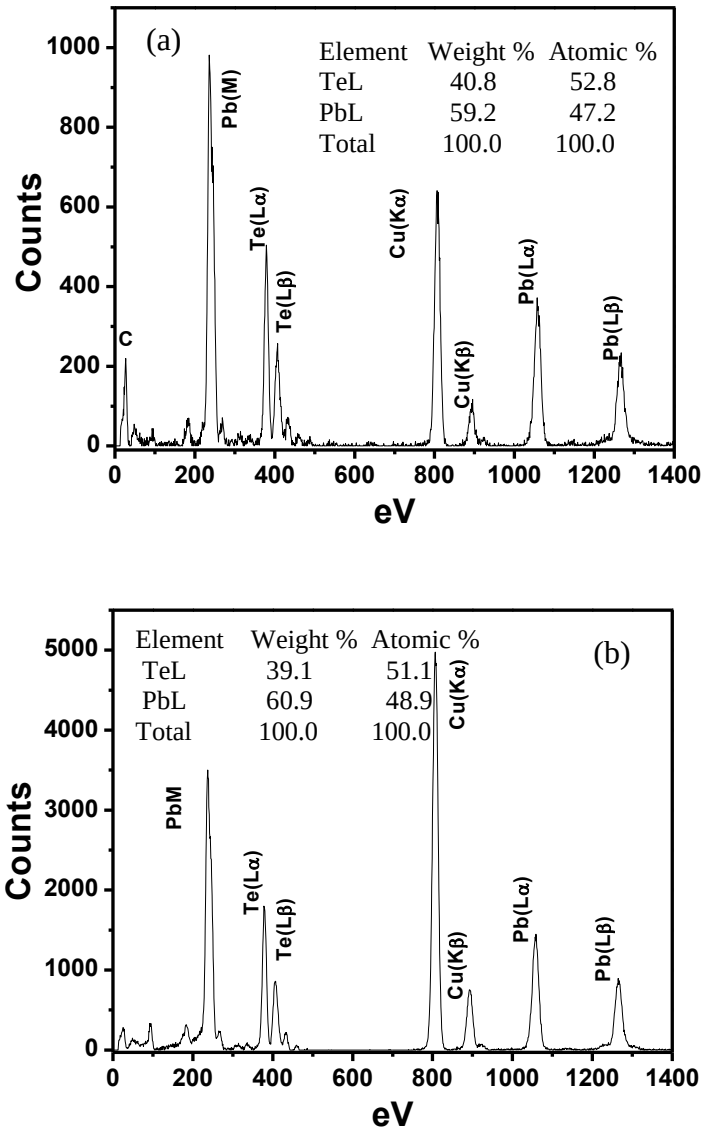

Figure 3.12 EDS of a) PbTe nanoparticles of size 12 nm and b) PbTe aerogels prepared from 12 nm particles.

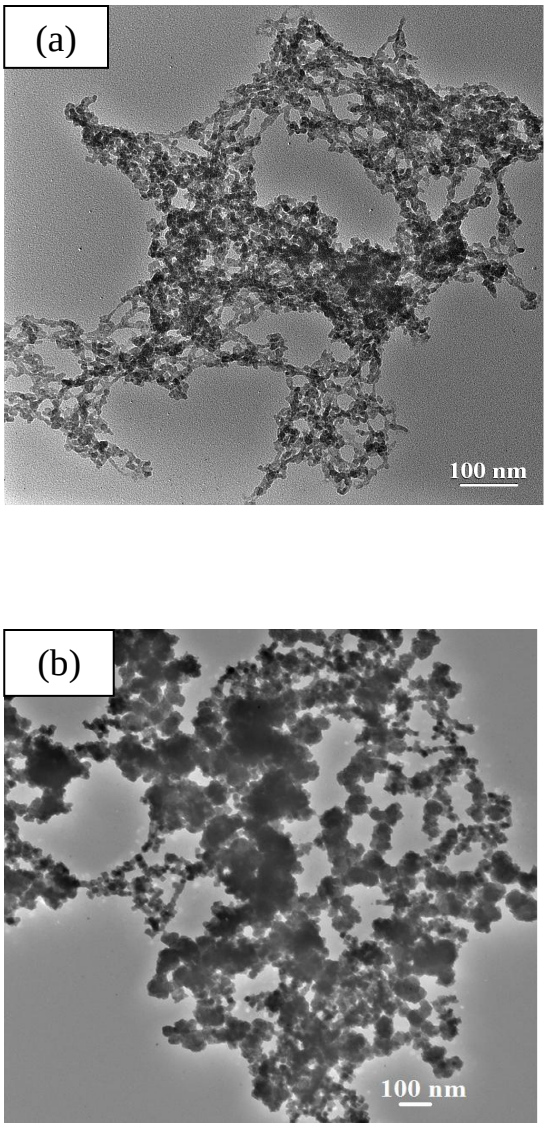

Figure 3.13 TEM micrographs of aerogel networks obtained after addition of 3% H_2O_2 to achieve a ratio of concentration of a) $[H_2O_2]$:$[Pb^{2+}]$ = 1: 6 and b) $[H_2O_2]$: $[Pb^{2+}]$ = 1: 11.

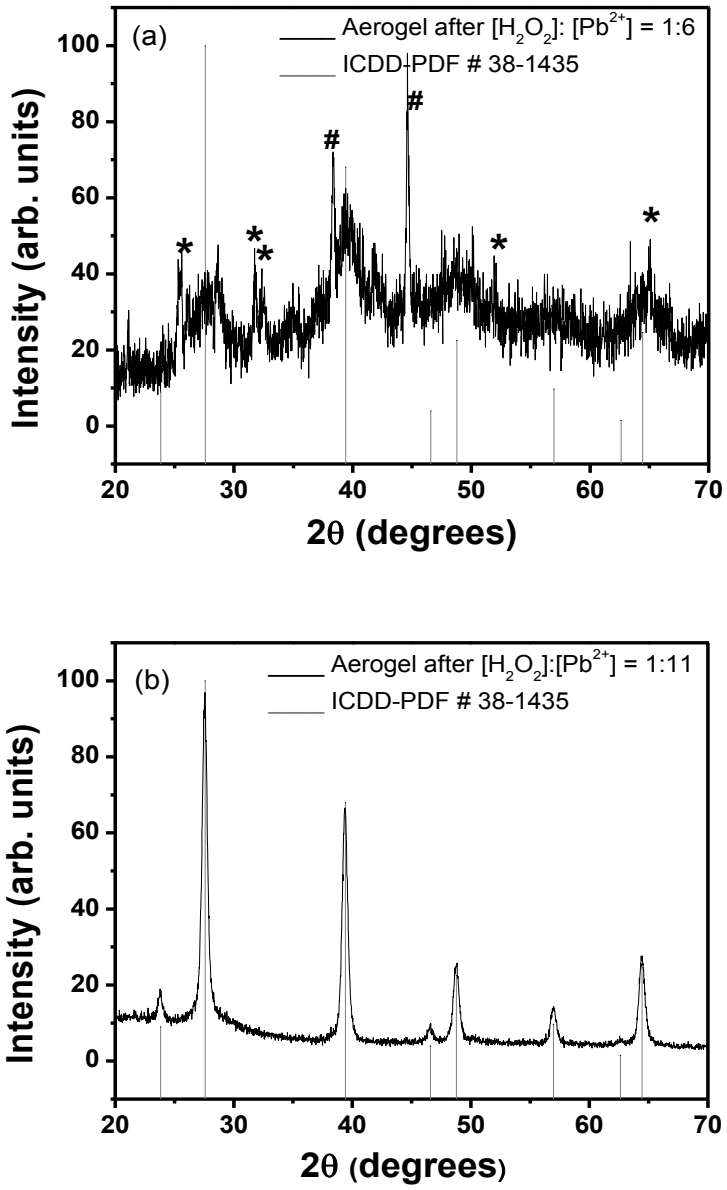

Figure 3.14 PXRD pattern of PbTe aerogel obtained after addition of 3 % H_2O_2 to achieve a ratio of concentration of a) $[H_2O_2]$: $[Pb^{2+}]$ = 1: 6 and b) $[H_2O_2]$:$[Pb^{2+}]$ = 1:11. The symbols "*" and "#" in (a) denote impurity peaks from Te_2O_5 and Pb_2O_3, respectively. The line diagrams correspond to the ICDD-PDF # 38-1435 of cubic PbTe.

3.5 Conclusion

The sol-gel method of nanoparticle assembly has been applied to the PbTe system. The resulting aerogels and xerogels have identical crystallite size to the precursors, but the particles are linked together into a matter-pore architecture with average pore diameter in the meso (2-50 nm) regime and surface areas ranging from 25-75 m^2/g. Temperature processing over the 250-450 °C range at atmospheric pressure results in desorption/decomposition of surface ligands, and melting is observed at 920 °C, which corresponds to the reported melting point of PbTe. However, under vacuum, sublimation is initiated just beyond 400 °C; linking the particles together has resulted in an increase in the onset, and a broadening of the temperature range, relative to the precursor particles, as probed by *in situ* heating in the TEM. Thus, aerogels show augmented thermal stability over the nanoparticle precursors. The presence of pores and interfaces on the nanoscale is expected to result in phonon scattering, thereby decreasing thermal transport and potentially leading to enhanced thermoelectric properties.

Chapter 4

Extension of sol-gel methodology to Bi_2Te_3 and $Bi_xSb_{2-x}Te_3$ nanoparticles and corresponding aerogel materials

4.1 Introduction

After successfully applying the sol-gel method to PbTe nanostructures, we wanted to examine the generality of this procedure for other heavier telluride materials, specifically Bi_2Te_3 and alloys of Bi_2Te_3-Sb_2Te_3. Bi_2Te_3 and Bi_2Te_3-Sb_2Te_3 alloys are state-of-the-art thermoelectric materials for devices operating in the temperature region from -20 °C to 100 °C.[8] Thus, they have been used as elements for cooling purposes. Nanostructures of these materials have been the focus of considerable attention in the hope of further enhancing the ZT of the material (which attains a value of 1 at 300 K for bulk Bi_2Te_3 materials). This Chapter deals with the synthesis and characterization of nanoparticles and aerogels of Bi_2Te_3 and Bi_2Te_3-Sb_2Te_3 alloy ($Bi_xSb_{2-x}Te_3$) materials along with thermoelectric property measurements, enabling the effect of sol-gel assembly on the thermoelectric figure of merit to be assessed.

This is a collaborative project that includes the groups of Dr. Donald Morelli and Dr. Jeff Sakamoto from Michigan State University. I did the synthesis and characterization of the nanoparticles and aerogels whereas the hot pressing and the thermoelectric property measurements of the samples were done at Michigan State University (MSU) by Dr. Chen (Kevin) Zhou, then a joint student of Dr. Morelli and Dr. Sakamoto.

4.2 Experimental

4.2.1 Materials

Bismuth neodecanoate (technical grade), bismuth acetate (≥ 99.99 % metal basis), antimony acetate (≥ 99.99 % metal basis), tellurium powder (Te, 200 mesh, 99.8 %), 1-dodecanethiol (DDT, 98 %), diphenylether (DPE, technical grade 90 %) and tetranitromethane (TNM) were

obtained from Sigma-Aldrich; trioctylphosphine (TOP, technical grade 97 %) and triethyl amine (TEA, reagent) were obtained from Strem chemicals and oleic acid (OA, technical grade, 90 %) was obtained from Fisher.

4.2.2 Synthesis of Thiolate-Capped Bi_2Te_3 and $Bi_xSb_{2-x}Te_3$ Nanoparticles

The synthesis of the Bi_2Te_3 nanoparticles employed in the sol-gel assembly was adapted with minor variations from Dirmyer and coworkers.[59] The method includes heating a mixture of bismuth neodecanoate (0.63 mL, 0.9 mmol), diphenyl ether (50 ml, 290 mmol) and thiol capping agent, 1-dodecanethiol (1-DDT) (10 ml, 40 mmol), at 120 °C followed by injection of anion monomer trioctylphosphine telluride (TOPTe) (1.5 mL, 1 M). The temperature was maintained for 1 h (growth time), followed by quenching of the reaction in a cold water bath and isolation by centrifugation. The black product was washed twice with toluene and dried under vacuum.

The synthesis of the $Bi_xSb_{2-x}Te_3$ nanoparticles (where, x = 0.5) employed in the sol–gel assembly was adapted from Burda and coworkers.[74] Briefly, a mixture of bismuth acetate (0.193 g, 0.4 mmol), antimony acetate (0.342 g, 1 mmol), diphenyl ether (50 ml, 290 mmol) and thiol capping agent, 1-DDT (10 mL, 40 mmol), was heated to 120 °C followed by injection of anion monomer trioctylphosphine telluride (TOPTe) (2 mL, 1 M). The temperature was maintained for 30 min (growth time), followed by quenching of the reaction in a cold water bath. The product was isolated as described for Bi_2Te_3.

4.2.3 Generation of Bi_2Te_3 and $Bi_xSb_{2-x}Te_3$ Aerogels

Once the dried thiolate capped nanoparticles of Bi_2Te_3 and $Bi_xSb_{2-x}Te_3$ were obtained, 500 mg and 200 mg, respectively, of the samples were dispersed in 20 mL of acetone targeting a final concentration of Bi^{3+} = 0.06 M (Bi_2Te_3) and combined concentration of Bi^{3+} and Sb^{3+} of 0.03 M for $Bi_xSb_{2-x}Te_3$, assuming $Bi_{0.5}Sb_{1.5}Te_3$ composition. The concentrations were calculated based

on the bulk molecular weight of each species. The solutions were then each divided in four different vials (5 mL each) and gelation was induced by adding 0.1 mL of 3 % TNM in acetone (v/v). The solution was shaken and gelation was observed within 1 h. The wet gels were aged for 4-5 days under ambient conditions and then were exchanged with acetone twice a day for another 2 days. A portion of the wet gel was transferred to fresh vials and supercritically dried, as described in Chapter 2, to produce an aerogel.

4.3 Characterization Techniques

PXRD, TEM, IR, surface area/porosimetry and thermoelectric property measurements (Seebeck coefficient, electrical resistivity, thermal conductivity and Hall coefficient) were used to characterize the materials. For more details on the measurement techniques, refer to Chapter 2.

4.4 Results and Discussion

4.4.1 Synthesis and Characterization of Bi_2Te_3 and $Bi_xSb_{2-x}Te_3$ Nanoparticles and Aerogels

a) Synthesis

Bi_2Te_3 and $Bi_xSb_{2-x}Te_3$ materials were chosen because they are well established thermoelectric materials in the bulk form, and nanostructuring of these materials is expected to enhance ZT by reducing the lattice thermal conductivity via scattering of heat carrying phonons from the nanoscale interfaces, as has been observed in related systems.[61, 75] Moreover, the presence of pore-matter interfaces in aerogels may lead to enhanced phonon scattering. The synthetic procedure for Bi_2Te_3 nanoparticles was adapted from Dirmyer et. al.[59] The synthesis involved injecting bismuth neodecanoate, the cation monomer, to a heated solution of DPE at high temperatures. Immediately after injecting the bismuth precursor, the thiolate capping agent, 1-DDT was added, changing the colorless solution to yellow. Upon addition of the anion monomer, TOPTe, the color of the solution changed from yellow to black. After a growth time

of 1 h, the particles were centrifuged and isolated. The black solids were further washed with toluene and dried under vacuum.

The synthetic procedure followed for the $Bi_xSb_{2-x}Te_3$ nanoparticles was adapted from Burda et. al.[74] The bismuth (bismuth acetate) and the antimony precursor (antimony acetate) were heated at high temperatures along with 1-DDT (capping agent) and DPE solvent. TOPTe was injected at high temperature. After a desired growth time of 30 min, the black solution was centrifuged followed by washing with toluene. The final black product obtained was dried under vacuum.

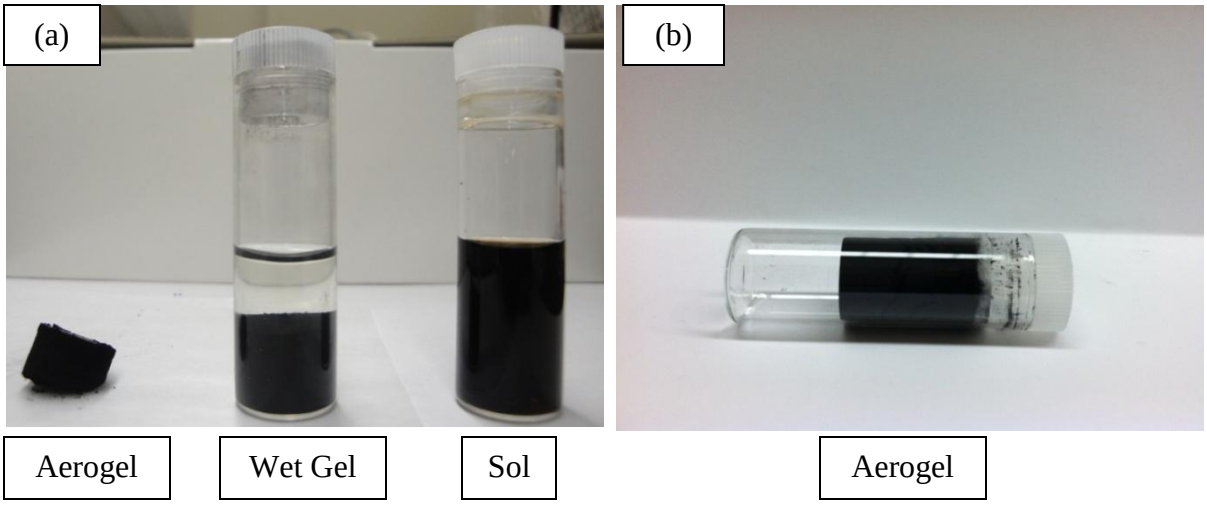

Figure 4.1 Images of (a) Bi_2Te_3 aerogel, wet gel and sol, (b) $Bi_xSb_{2-x}Te_3$ aerogel obtained after supercritical drying of the wet gel.

Gelation of the Bi_2Te_3 and $Bi_xSb_{2-x}Te_3$ nanoparticles was achieved by dispersing the thiolate capped nanoparticles in acetone to form a sol, followed by addition of 0.1 mL of 3 % TNM as oxidizing agent removing the surface bound thiolate groups and also condensing the nanoparticles together, forming the wet gels (**Figure 4.1)**. These wet gels were further aged for 4 days under ambient conditions then exchanged with fresh acetone twice daily for two days to

remove byproducts of gelation. At this point strong monolithic wet gels were obtained, which were transferred carefully into new vials and then supercritically dried to form aerogels. The resultant aerogels for both the samples were monolithic in nature and black in color as shown in **Figure 4.1**.

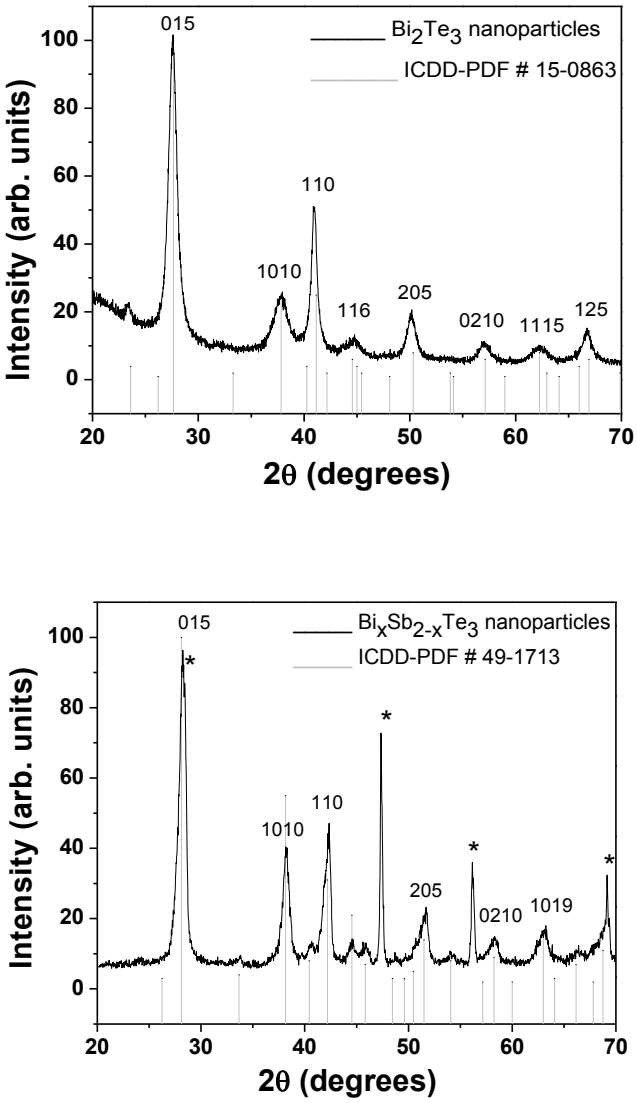

Figure 4.2 Powder X-ray diffraction patterns of Bi_2Te_3 nanoparticles and $Bi_xSb_{2-x}Te_3$ nanoparticles. The vertical lines correspond to the ICDD-PDF #15-0863 for Bi_2Te_3 and ICDD-PDF #49-1713 for $Bi_{0.5}Sb_{1.5}Te_3$, both adopting the rhombohedral phase. The * on the PXRD corresponds to Si peaks matching the ICDD-PDF # 27-1402 of Si.

b) Characterization

The phase and crystallite size of the products obtained above were determined by powder X-ray diffraction experiments. The PXRD patterns of the Bi_2Te_3 and $Bi_xSb_{2-x}Te_3$ nanoparticles, matched the rhombohedral phase of Bi_2Te_3 and $Bi_{0.5}Sb_{1.5}Te_3$, respectively (**Figure 4.2**). The PXRD data for $Bi_xSb_{2-x}Te_3$ was collected along with an internal silicon standard to observe any shifts in the lattice parameter due to formation of more Sb-rich or less Sb-rich phases than the targeted $Bi_{0.5}Sb_{1.5}Te_3$. The pattern was a perfect match to ICDD-PDF # 49-1713 of $Bi_{0.5}Sb_{1.5}Te_3$. Application of the Scherrer equation rendered a value of 35 nm for Bi_2Te_3 and 50 nm for $Bi_{0.5}Sb_{1.5}Te_3$ nanoparticles, based on the (015) plane in both cases.

TEM was employed to verify the size and determine the morphology of the Bi_2Te_3 and $Bi_xSb_{2-x}Te_3$ nanoparticles. Both the Bi_2Te_3 and $Bi_xSb_{2-x}Te_3$ nanoparticles manifested as aggregates of plate like morphology with an overall aggregate size of ~ 40 nm (**Figure 4.3**). The plate like morphology is inherent to Bi_2Te_3 materials, as the crystal structure of Bi_2Te_3 consists of Bi and Te layers with rhombohedral hexagonal symmetry.[8, 76] Strong covalent interactions exist between the Bi and Te layers whereas the adjacent Te layers are held together by weak Van der Waals interactions.

The PXRD patterns for the Bi_2Te_3 and $Bi_xSb_{2-x}Te_3$ aerogels obtained from the nanoparticles were similar to those of the starting precursor nanoparticles suggesting both the crystallite size and phase are retained in the gelation and drying process (**Figure 4.4**). The $Bi_xSb_{2-x}Te_3$ and Bi_2Te_3 aerogels displayed a colloidal morphology consisting of an interconnected network of nanoparticles with pores clearly evident in the TEM images (**Figure 4.5**). This shows that the sol-gel method was successful in connecting the discrete nanoparticles together forming a gel network.

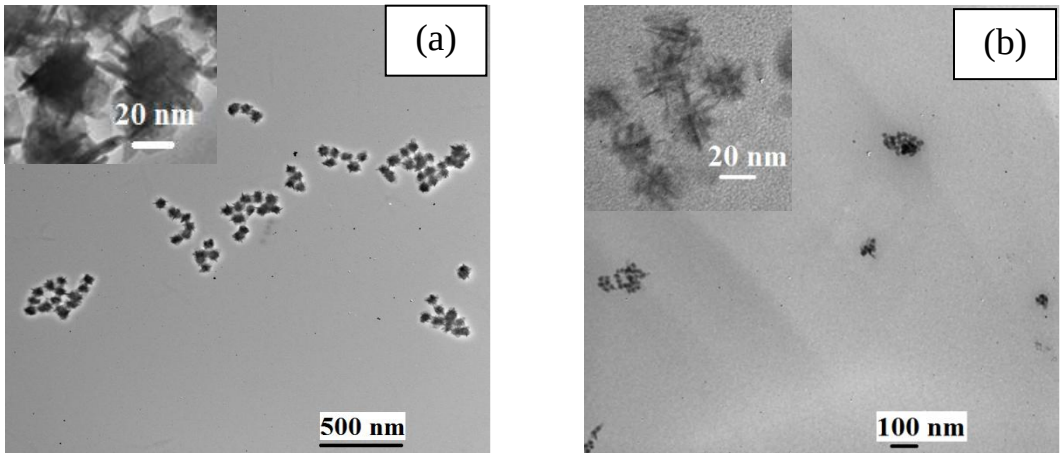

Figure 4.3 TEM images of (a) Bi_2Te_3 nanoparticles and (b) $Bi_xSb_{2-x}Te_3$ nanoparticles. The inset show high resolution TEM images (HRTEM).

A semiquantitative EDS study of the Bi_2Te_3 and $Bi_xSb_{2-x}Te_3$ nanoparticles and aerogels was performed to determine the elemental compositions in the samples. The Bi_2Te_3 nanoparticles have a Bi:Te:S ratio of 1.8:3:0.9 for the nanoparticles, corresponding to a Te-rich Bi_2Te_3 phase. The sulfur content is attributed to surface thiolate groups. The aerogels have a Bi:Te:S ratio of 2.2:3:0.4, suggesting some Te loss in the gel and aerogel formation process, yielding a Bi-rich phase (**Figure 4.6**). The decrease in sulfur content is indicative of loss of surface thiolates, consistent with the oxidative gelation mechanism.[77]

In the case of $Bi_xSb_{2-x}Te_3$ nanoparticles and aerogels, the Bi:Sb:Te:S ratio was found to be 0.6:1.6:3:0.1 for nanoparticles and 0.5:1.5:3:0.1 for aerogels, respectively. The values obtained are close to the desired composition of $Bi_{0.5}Sb_{1.5}Te_3$. The data also show that there was less residual sulfur from the dodecanethiol in the case of $Bi_{0.5}Sb_{1.5}Te_3$ nanoparticles and aerogels relative to the Bi_2Te_3 case (**Figure 4.7**). The presence of a lower amount of organic groups is a

good sign for thermoelectric measurements as the organic groups are expected to act as an insulating layer that reduces the electrical conductivity of the system.[78]

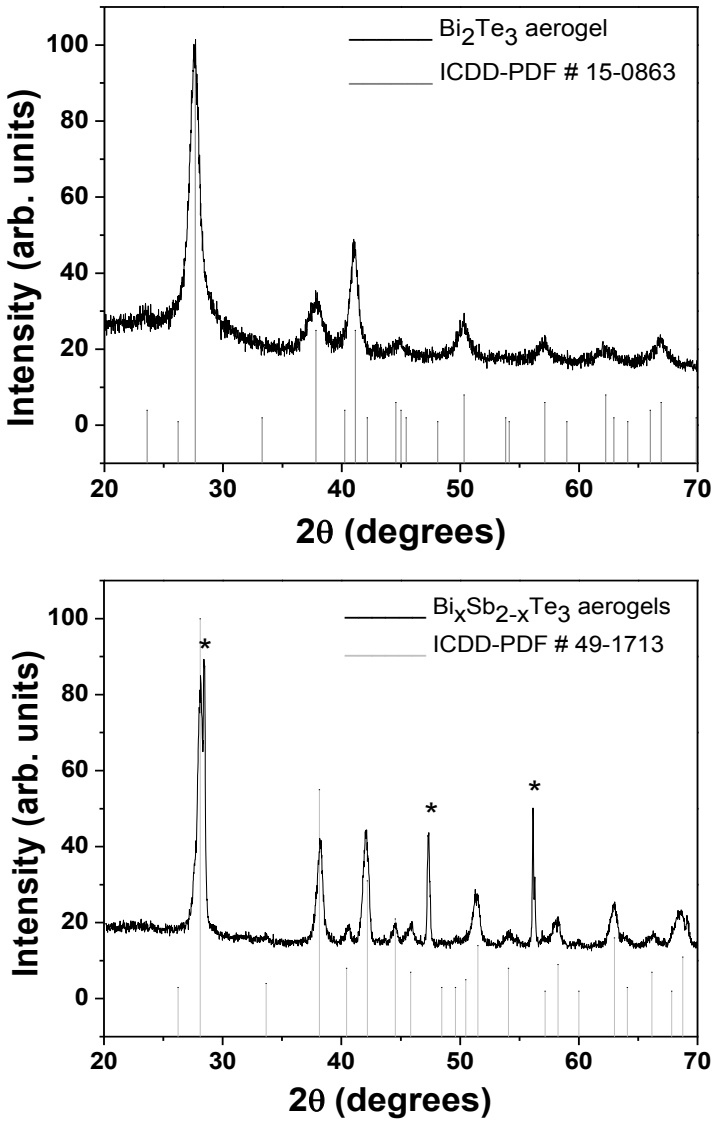

Figure 4.4 Powder X-ray diffraction patterns of Bi_2Te_3 and $Bi_xSb_{2-x}Te_3$ aerogels derived from discrete nanoparticles. The vertical lines correspond to the ICDD-PDF #15-0863 for Bi_2Te_3 and ICDD-PDF #49-1713 for $Bi_{0.5}Sb_{1.5}Te_3$, both adopting the rhombohedral phase. The ICDD-PDF # 27-1402 of Si is also shown.

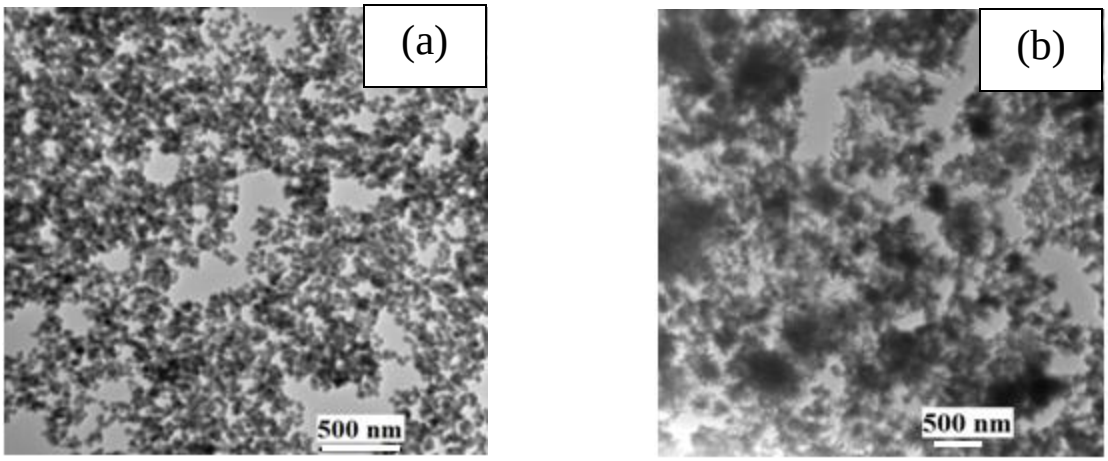

Figure 4.5 TEM images of (a) Bi_2Te_3 and (b) $Bi_xSb_{2-x}Te_3$ aerogels obtained from the corresponding nanoparticles.

To analyze the surface area and porosity characteristics of the Bi_2Te_3 and $Bi_xSb_{2-x}Te_3$ nanoparticles and aerogels, samples were heated at 150 °C under Ar, for 24 h to remove any moisture or volatile impurities from the surface of the aerogels, followed by acquisition of nitrogen adsorption/desorption isotherms (**Figure 4.8).**

The surface area analysis of Bi_2Te_3 materials, modeled by the Brunauer, Emmet and Teller (BET) method, yielded a value of ca 40 m^2/g for aerogels and 16 m^2/g for nanoparticles (**Table 4.1**). The surface area of the nanoparticles was lower than that of the aerogels suggesting that supercritical drying enables better access to the particle surface. The nitrogen adsorption/desorption isotherms illustrated that the aerogels and xerogels display type IV isotherm curves that are characteristic of a mesoporous material (2-50 nm pore diameter), and the pore size distribution (**Figure 4.8,** inset), calculated using the Barret, Joyner and Halenda (BJH) model, is consistent with a broad range of pores extending into the macropore region (>50 nm). Intriguingly, BJH plots for nanoparticles reveal very similar features. As there is no pore

structure evident in TEM images, we attribute these to filling of interstices in the solid nanoparticle samples.[79] Similar pore characteristic/pore sizes were observed for the $Bi_xSb_{2-x}Te_3$ aerogels and nanoparticles (**Figure 4.9)**, where the nanoparticles again showed lower surface area (15 m^2/g) relative to the aerogels (36 m^2/g) (**Table 4.1**).

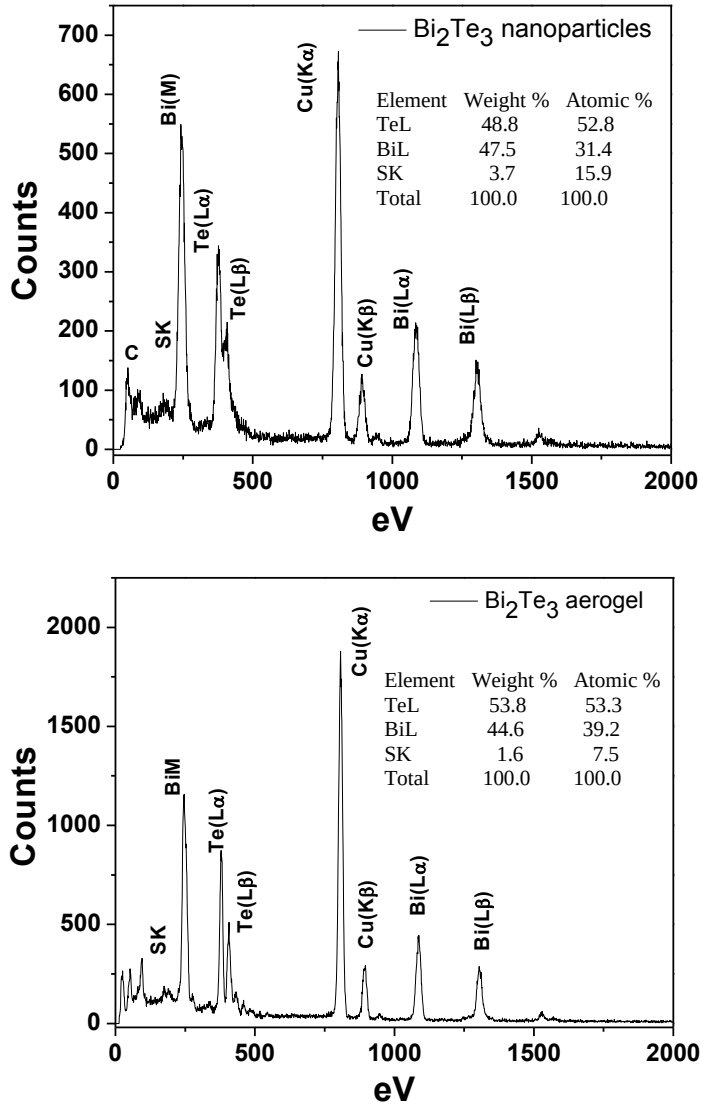

Figure 4.6 EDS of Bi_2Te_3 nanoparticles and resultant aerogel. The peak due to copper is attributed to the TEM grid.

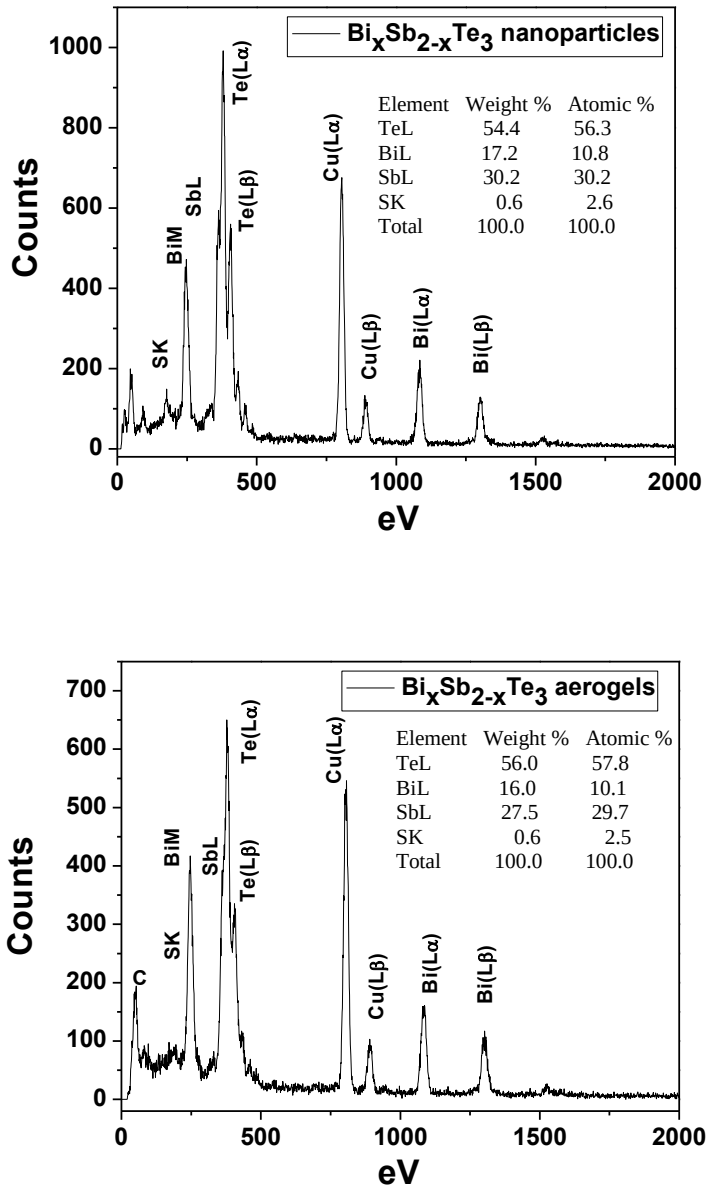

Figure 4.7 EDS of $Bi_xSb_{2-x}Te_3$ nanoparticles and resultant aerogel. The peak due to copper is attributed to the TEM grid.

Table 4.1 BET surface area, average pore diameter and cumulative pore volume of the nanoparticles and aerogels of Bi_2Te_3 and $Bi_xSb_{2-x}Te_3$ samples.

Samples	BET surface area in m^2/g	Average pore diameter (nm)	Cumulative pore volume (cm^3/g)
Bi_2Te_3 nanoparticles	16	24	0.10
Bi_2Te_3 aerogel	45	9.3	0.10
$Bi_xSb_{2-x}Te_3$ nanoparticles	15	13	0.06
$Bi_xSb_{2-x}Te_3$ aerogel	36	9	0.10

To prepare for measurement of thermoelectric properties, the nanoparticles and aerogels of Bi_2Te_3 and $Bi_xSb_{2-x}Te_3$ were annealed at 200 °C for 2 h under Ar atmosphere in a flow furnace to remove residual organic ligands. This is done because the organic ligands are expected to act as trap centers for the electrons and hamper the electrical transport in the system. IR was employed to probe the removal of the surface organic groups. **Figure 4.10** shows the IR before and after heating the aerogels of Bi_2Te_3 samples. The peaks at 2924 cm^{-1} and 2846 cm^{-1} correspond to the aliphatic–CH stretches from the capping agent (1-DDT) which are present before heating. The disappearance of organic peaks, as evident in the IR spectra after annealing the samples, suggests that heating removes the organic surface capping groups. The same observation was noted for the $Bi_xSb_{2-x}Te_3$ nanoparticles and aerogels.

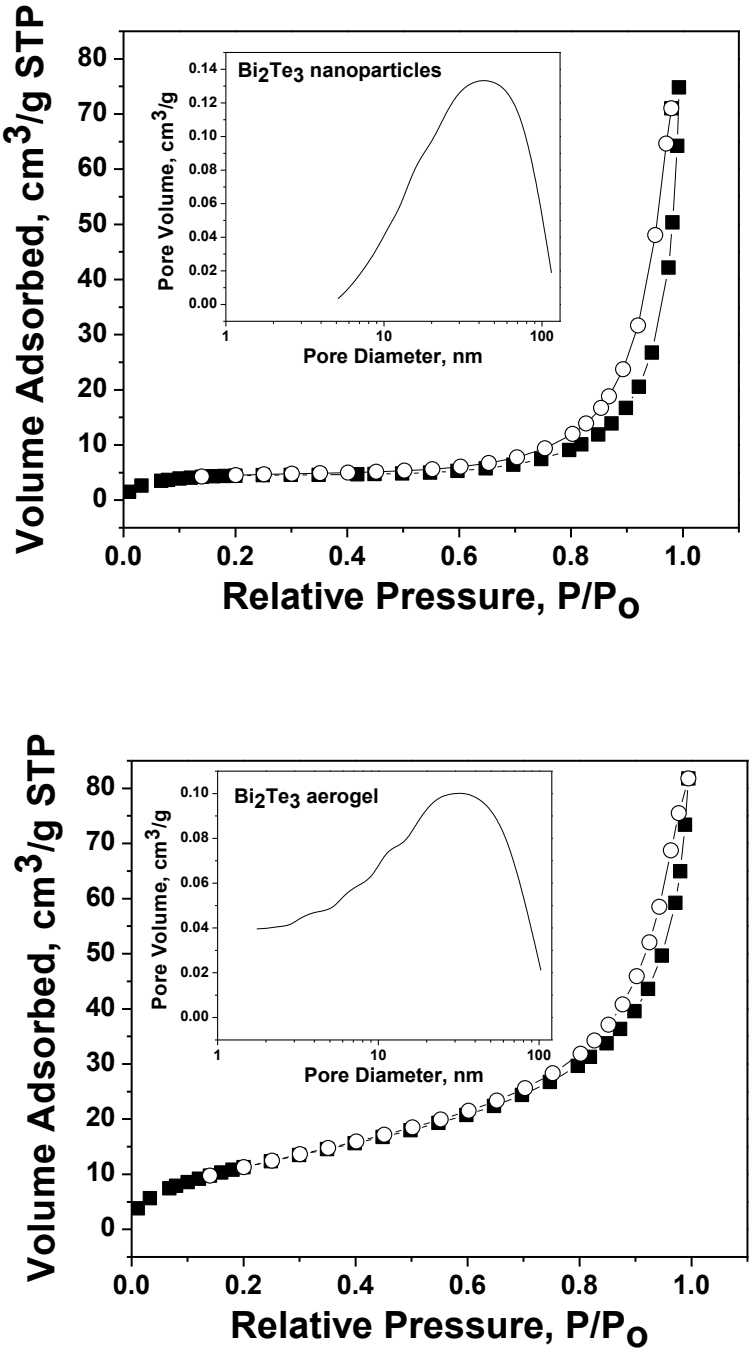

Figure 4.8 N_2 adsorption (■)/desorption (○) isotherms of Bi_2Te_3 nanoparticles and aerogel samples. The inset shows the corresponding BJH pore size distributions.

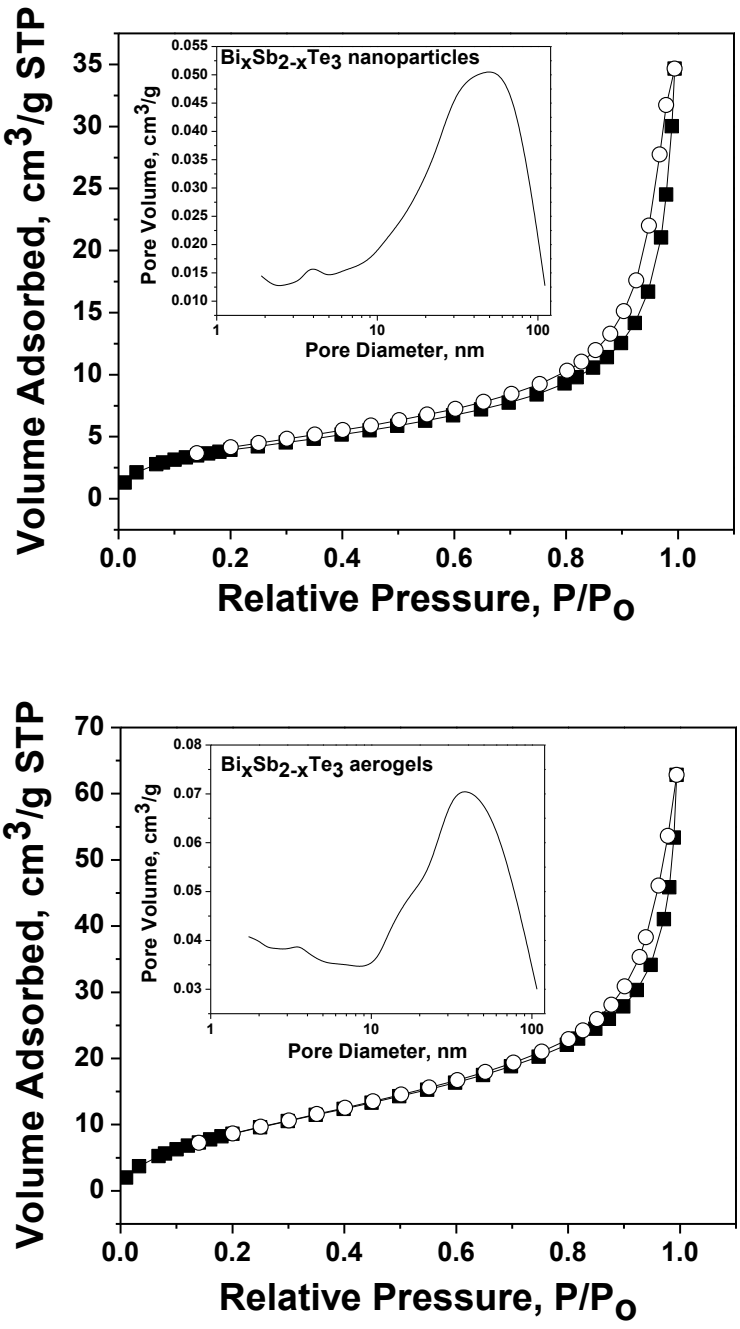

Figure 4.9 N_2 adsorption (■)/desorption (○) isotherms of $Bi_xSb_{2-x}Te_3$ nanoparticles and aerogel samples. The inset shows the corresponding BJH pore size distributions.

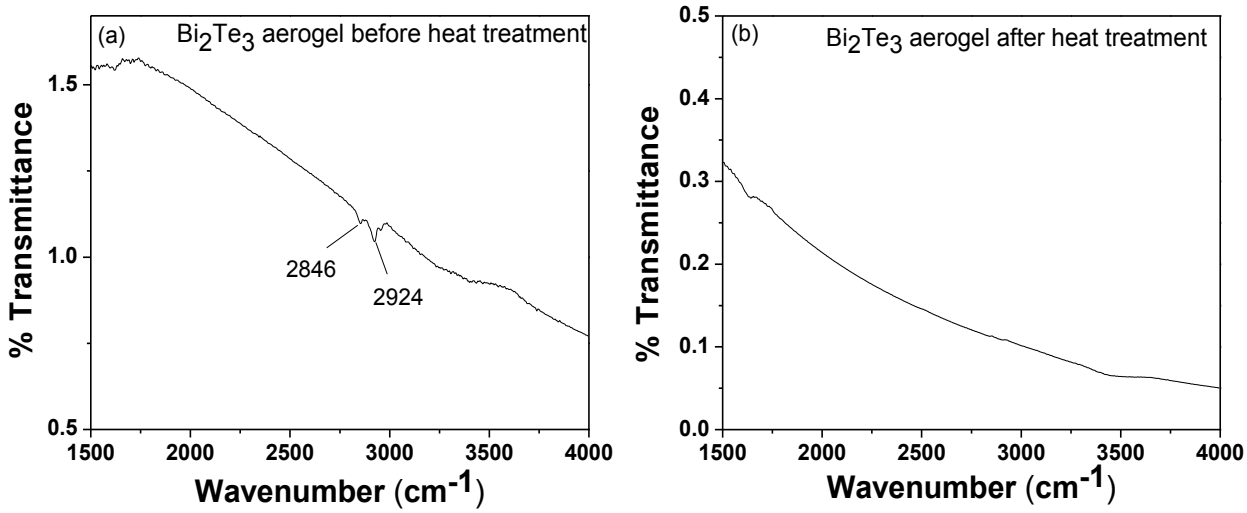

Figure 4.10 IR of Bi_2Te_3 aerogel (a) before and (b) after heating under Ar in a flow furnace at 200 °C.

4.4.2 Thermoelectric Property Measurements (Acquired by our Collaborators from Michigan State University)

Bi_2Te_3 and $Bi_xSb_{2-x}Te_3$ nanoparticles and aerogels were hot pressed at 450 °C to form pellets from which rectangular parallelopipeds were cut to perform TE transport property measurements. To probe the effect of hot-pressing on crystallite size and composition, TEM/EDS data were acquired on the hot pressed pellets of the nanoparticles and aerogels. TEM images of the nanoparticles show nanoscopic features which are < 100 nm in diameter (**Figure 4.11**). Similar results were seen in aerogels, suggesting that hot pressing keeps the size of the resultant materials in the nano-regime. The elemental analysis of the hot pressed Bi_2Te_3 aerogels reveals the Bi:Te ratio to be 2.5:3 and the Bi:Sb:Te ratio in $Bi_xSb_{2-x}Te_3$ aerogels to be 0.3:1.2:3 (**Figure 4.12**), whereas for the hot pressed nanoparticles, the ratios are Bi:Te = 2:3 and Bi:Sb:Te

= 0.5:1.2:3, respectively. This suggests, relative to the nanoparticles, a Bi rich phase for the hot pressed Bi_2Te_3 aerogels and a Te rich phase for the hot pressed $Bi_xSb_{2-x}Te_3$ aerogel.

Figure 4.13 shows the Seebeck coefficient (S) as a function of temperature for the Bi_2Te_3 and $Bi_xSb_{2-x}Te_3$ nanoparticles. As discussed in Chapter 1, the sign of S (negative or positive) reflects the majority charge carriers (electrons or holes) in the system. The Seebeck coefficient increases monotonously with increasing temperature for both the samples and acquires a positive value, suggesting p-type behavior for these materials. For Bi_2Te_3 nanoparticles, the S value obtained at 300 K is lower than the bulk material[80] whereas for $Bi_xSb_{2-x}Te_3$ nanoparticles, the S value is comparable to the bulk material (**Table 4.2**).[81] The electrical resistivity for both Bi_2Te_3 and $Bi_xSb_{2-x}Te_3$ nanoparticles exhibits a similar trend, the value increases with the increase in temperature as shown in **Figure 4.13**. However, despite this temperature dependent increase, due to the strong influence of S in the power factor term, $S^2\sigma$ (S^2/ρ) increases with the increase in temperature (**Figure 4.13**). While the room temperature value of S (**Table 4.2**) is higher for the $Bi_xSb_{2-x}Te_3$ nanoparticles relative to Bi_2Te_3 nanoparticles, the greater electrical resistivity values in the former results in a lower power factor for $Bi_xSb_{2-x}Te_3$ nanoparticles. The power factor value obtained at 300 K for Bi_2Te_3 nanoparticles (5.0 $\mu W/(cm\cdot K^2)$) is either higher or comparable to other chemically synthesized Bi_2Te_3 nanoparticles (for example, 2.4 $\mu W/(cm\cdot K^2)$[75] and 5.0 $\mu W/(cm\cdot K^2)$[61] at 300 K). However, for $Bi_xSb_{2-x}Te_3$ nanoparticles, the power factor value obtained at 300 K (3.3 $\mu W/(cm\cdot K^2)$) is lower than that reported in the literature (for example, 7.8 $\mu W/(cm\cdot K^2)$[75] and 7.0 $\mu W/(cm\cdot K^2)$[62] at 300 K). Power factors for bulk $Bi_xSb_{2-x}Te_3$ materials are a factor of 5-10 times greater than those obtained for nanoparticles.

One of the main benefits of using nanoparticles for thermoelectric applications is to achieve reduction in thermal conductivity.[75] The total thermal conductivities of the Bi_2Te_3 and $Bi_xSb_{2-x}Te_3$ nanoparticles are shown in **Figure 4.13**. The lattice thermal conductivity is estimated by subtracting the electronic thermal conductivity from the total thermal conductivity. The electronic thermal conductivity is calculated by the Wiedemann Franz law $\kappa_e = L\sigma T$ where σ is the electrical conductivity, T is the absolute temperature and L is the Lorenz number, which assumes a value of $L = 2.44 \times 10^{-8}\ V^2/K^2$. The total, as well as the lattice thermal conductivity, decreases with the increase in temperature for Bi_2Te_3 nanoparticles, whereas for $Bi_xSb_{2-x}Te_3$ nanoparticles, both remain constant over the entire temperature range measured. The lattice thermal conductivity value obtained for the Bi_2Te_3 nanoparticle sample at 300 K is lower than the reported value for bulk material (**Table 4.2**).[82] This result justifies the benefit of utilizing the reduced dimension (less than 100 nm) of Bi_2Te_3 nanoparticles to effectively cap the phonon mean free path. For the case of $Bi_xSb_{2-x}Te_3$, addition of nanostructuring has little effect on the lattice thermal conductivity, which is already pretty low due to point scattering effects from the disordered cation lattice. Overall, the lattice thermal conductivity value obtained for Bi_2Te_3 and $Bi_xSb_{2-x}Te_3$ nanoparticles is similar to that found in prior reports (0.011 W/(cm·K) and 0.012 W/(cm·K) at 300 K for Bi_2Te_3 and $Bi_xSb_{2-x}Te_3$ nanoparticles, respectively).[75] Finally, the overall ZT obtained after combining all the parameters increases with that of temperature and at 300 K the ZT obtained was 0.18 for Bi_2Te_3 and 0.1 for $Bi_xSb_{2-x}Te_3$ nanoparticles. The value of ZT obtained for Bi_2Te_3 nanoparticles was either higher or comparable to other chemically synthesized nanoparticles (ZT = 0.03-0.2)[59,61] whereas for $Bi_xSb_{2-x}Te_3$ nanoparticles, the ZT is lower than the other chemically synthesized $Bi_xSb_{2-x}Te_3$ nanoparticles (previously reported as 0.5).[62, 75]

For Bi_2Te_3 and $Bi_xSb_{2-x}Te_3$ aerogels, surprising changes in electronic properties are observed. In Bi_2Te_3 aerogels, the value of S changed from negative at low temperature to positive at high temperatures during the measurement, suggesting the presence of two types of carriers in the system. This result is distinct from that observed for the nanoparticles of Bi_2Te_3, where the type of conduction was p-type over the entire measured temperature range (**Figure 4.14**). This suggests the advent of intrinsic conduction in the case of Bi_2Te_3 aerogels leading to two carriers co-existing in our material (**Figure 4.14**).

For $Bi_xSb_{2-x}Te_3$ aerogels, S shows a negative value, increasing in magnitude with the increase in temperature, suggesting n-type behavior, which again differs from that obtained for the $Bi_xSb_{2-x}Te_3$ nanoparticles. The cause of this conversion is uncertain but it might be due to the presence of excess tellurium present in the sample after hot pressing, as suggested by semi-quantitative elemental analysis (**Figure 4.12**). Excess Te is reported to act as n-type dopant by occupying Bi lattice sites in Bi_2Te_3 films.[83]

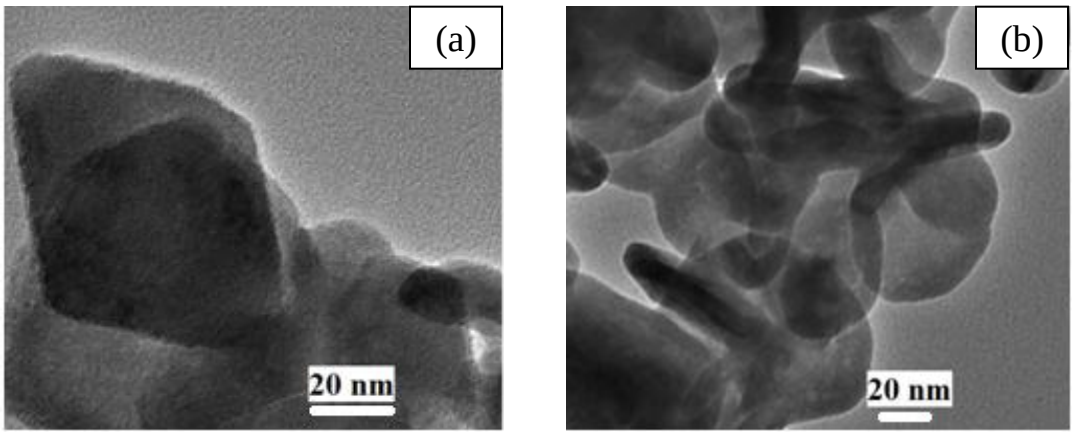

Figure 4.11 TEM images of (a) Bi_2Te_3 and (b) $Bi_xSb_{2-x}Te_3$ nanoparticles after hot pressing.

The electrical resistivity for the Bi_2Te_3 aerogels shows an activated behavior, decreasing with increasing temperature; for $Bi_xSb_{2-x}Te_3$ aerogels, the electrical resistivity increases marginally with the increase in temperature. Thus, the power factor obtained at 300 K for Bi_2Te_3 and $Bi_xSb_{2-x}Te_3$ aerogels is 0.06 $\mu W/(cm \cdot K^2)$ and 0.17 $\mu W/(cm \cdot K^2)$, respectively; both significantly lower than values obtained for the corresponding nanoparticles (**Table 4.2**).

Moreover, the power factor value for the Bi_2Te_3 aerogel is lower than that obtained previously (6×10^6 $\mu W/(cm \cdot K^2)$), which was prepared in our lab and processed similarly, yet demonstrated dramatically different electrical properties.[84] This underscores the sensitivity of the system to adventitious doping.

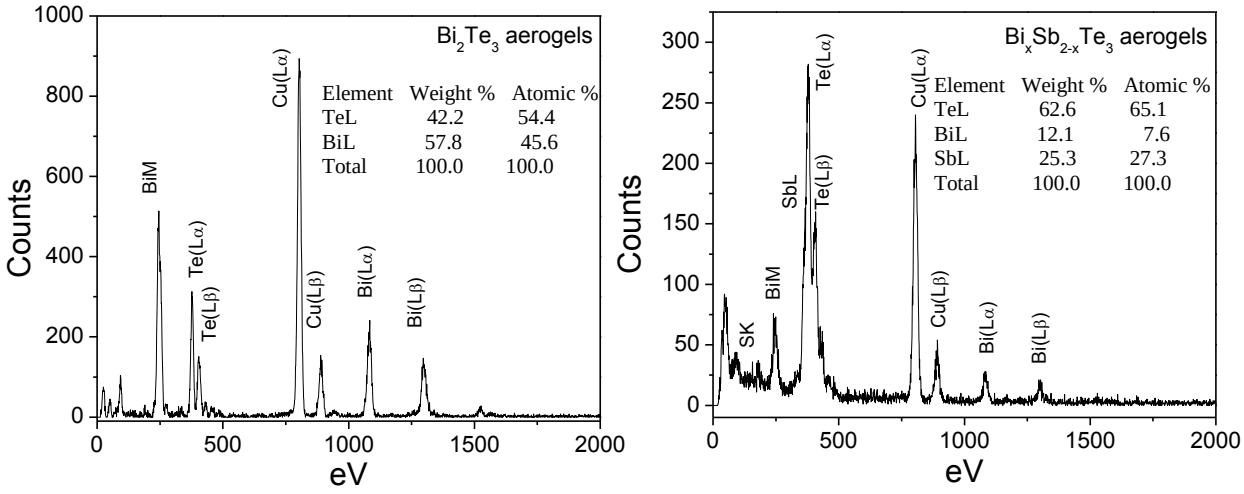

Figure 4.12 EDS analysis of aerogels of (a) Bi_2Te_3 and (b) $Bi_xSb_{2-x}Te_3$ after hot pressing. The peak due to copper is attributed to the TEM grid.

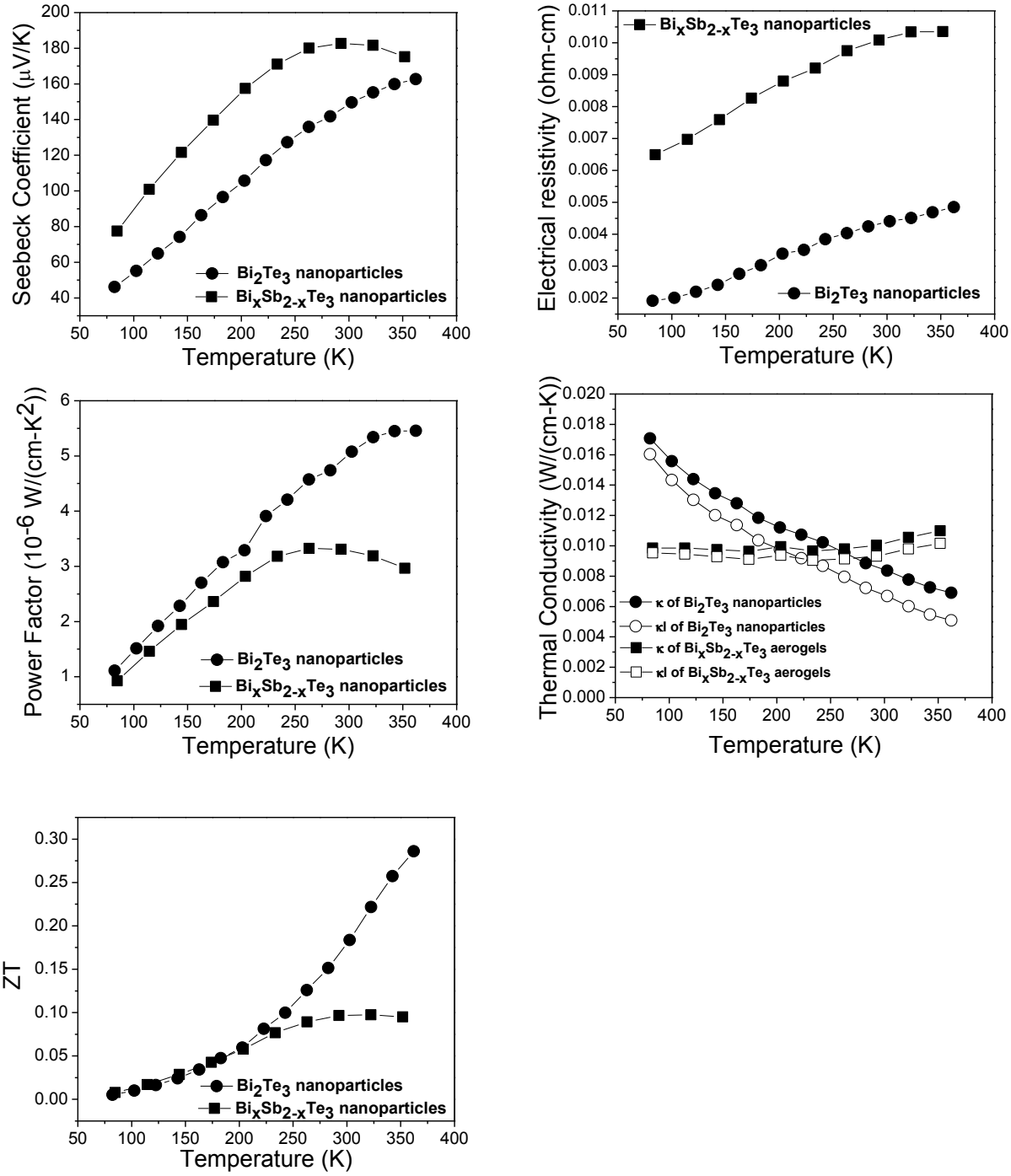

Figure 4.13 Thermoelectric properties of Bi_2Te_3 and $Bi_xSb_{2-x}Te_3$ nanoparticles.

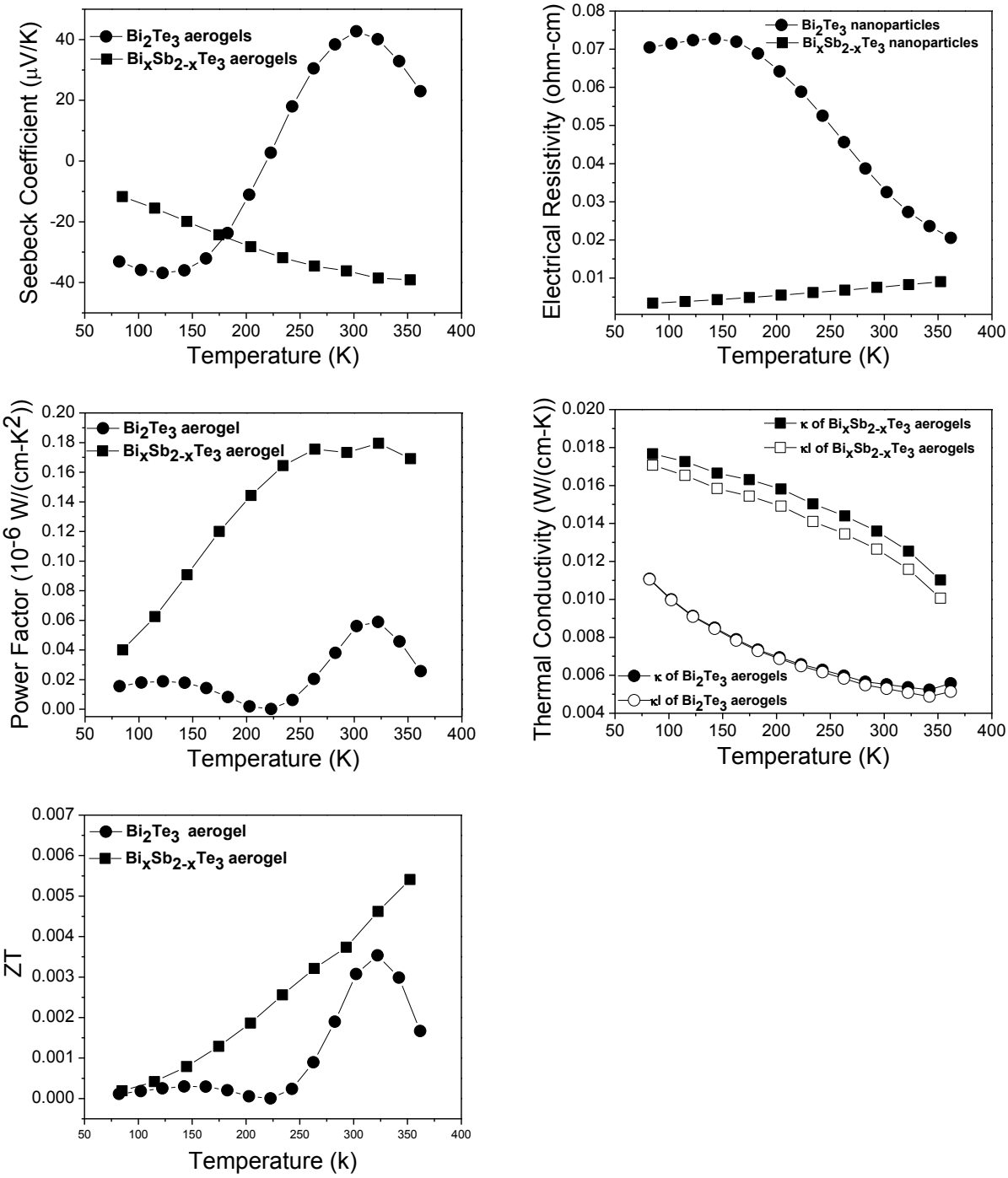

Figure 4.14 Thermoelectric properties of Bi_2Te_3 and $Bi_xSb_{2-x}Te_3$ aerogels obtained from discrete nanoparticles.

Table 4.2 Some room temperature (300 K) physical properties of Bi_2Te_3 and $Bi_xSb_{2-x}Te_3$ nanoparticles and aerogels along with their respective bulk counterparts for comparison

Thermoelectric properties	Bulk Bi_2Te_3[82]	Bi_2Te_3 nanoparticles	Bi_2Te_3 aerogels	Bulk $Bi_{0.5}Sb_{1.5}Te_3$[68]	$Bi_xSb_{2-x}Te_3$ nanoparticles	$Bi_xSb_{2-x}Te_3$ aerogels
Seebeck coefficient (μV/K)	227	150	43	186	183	-36
Electrical resistivity (10^{-3} Ω·cm)	1.9	4.5	33	1.1	10	7.5
Power factor (10^{-6} W/(cm·K^2)	26.4	5.0	0.06	31.5	3.3	0.17
Lattice thermal conductivity (10^{-2} W/cm·K)	17	0.6	0.5	1.0	0.9	1.0
ZT	0.7	0.18	0.003	0.6	0.1	0.005

The thermal conductivity data for the Bi_2Te_3 and $Bi_xSb_{2-x}Te_3$ aerogels were plotted as a function of temperature (**Figure 4.14)**. The lattice thermal conductivity measurements were calculated similarly to those of the nanoparticles assuming an L value of 2.44×10^{-8} V^2/K^2. The lattice thermal conductivity indeed reduces with the increase in temperature in the aerogel system, attributed to a strong phonon scattering effect from the pore-matter interfaces. The lattice thermal conductivity for Bi_2Te_3 aerogels is lower than that of the corresponding nanoparticles at 300 K, whereas the lattice thermal conductivity for the $Bi_xSb_{2-x}Te_3$ aerogels has a similar value to the starting nanoparticles (**Table 4.2**), again suggesting that nanostructuring does not add to phonon scattering beyond the doping effect. Unfortunately, the change in sign for S in both the aerogel samples indicates the electronic properties are severely degraded; hence, the overall ZT

values for the aerogel systems are significantly lower than for the corresponding nanoparticles at 300 K (**Figure 4.14, Table 4.2**). Previous studies on Bi_2Te_3 aerogel materials,[84] where high power factors are maintained, did not include thermal conductivity measurements, so no comparison of ZT can be made.

4.5 Conclusion

The sol-gel method has successfully been extended to Bi_2Te_3 and $Bi_xSb_{2-x}Te_3$ systems. The resultant aerogels preserve the phase and size of the precursor nanoparticles, and show a well connected network of nanoparticles with many pore-matter interfaces. The average pore diameter lies in the mesopore regime, and surface areas are ~36-40 m^2/g for the aerogels showing that the supercritical drying increases the accessible surface area as compared to the nanoparticles (15-16 m^2/g). Evaluation of the thermoelectric properties of the Bi_2Te_3 and $Bi_xSb_{2-x}Te_3$ aerogels suggested degraded electronic properties, as compared to the respective nanoparticles, owing to poor power factor ($S^2\sigma$). This could be attributed to the presence of excess Te in $Bi_xSb_{2-x}Te_3$ aerogels, and the presence of two types of carriers in Bi_2Te_3 as a result of adventitious doping in intrinsic materials, compensating the majority charge carriers in these systems. The power factor obtained for the Bi_2Te_3 aerogel is drastically lower than the Bi_2Te_3 aerogel previously published in literature, reiterating the fact that adventitious doping in these materials can lead to vastly different electronic properties.

Chapter 5

Synthesis and Evaluation of Lead Telluride/Bismuth Antimony Telluride Nanocomposites for Thermoelectric Applications

5.1 Introduction

Recently, considerable focus has been given to synthesizing nanostructures and nanocomposite materials[85] for improved figure of merit (ZT) in thermoelectric devices. Specifically, it has been shown that inclusion of nanoscale features dramatically reduces the thermal conductivity and improves the thermopower (S) of the system, as mentioned in Chapter 1.[2] The focus of this Chapter is the synthesis and characterization of heterostructured nanocomposites by incipient wetness impregnation of discrete PbTe nanoparticles in a bulk Bi_2Te_3 matrix, (both n-type and p-type). The efficacy of organic ligand removal from the surface of PbTe nanoparticles, both chemically and thermally, will be presented as these organic ligands, can potentially act as insulators and hamper the easy flow of electrons (as discussed in Chapter 1). Finally, the effect of impregnating different concentrations of PbTe nanoparticles in the bulk Bi_2Te_3 matrix on the thermoelectric properties of the composite will be discussed.

This work on PbTe nanoparticle inclusion in a p-type Bi_2Te_3 matrix has been published in *Journal of Solid State Chemistry*, 2011.[81] This is a collaborative project that includes the groups of Donald Morelli and Jeff Sakamoto from Michigan State University and the group of Ctirad Uher from the University of Michigan. I did the synthesis and characterization of the nanoparticles and nanocomposites and the preparation of the n-type and p-type Bi_2Te_3 matrices. The thermoelectric property measurements of the composites were done at Michigan State University (MSU) by Dr. Chen (Kevin) Zhou, then a joint student of Dr. Morelli and Dr. Sakamoto.

5.2 Experimental

5.2.1 Materials

Most of the materials used are mentioned in Chapter 3 except for high purity starting materials of bismuth (granule 99.997%), antimony (shot 99.999%), selenium (shot 99.999%) and tellurium (shot 99.9999%) which were obtained from Alfa Aesar.

5.2.2 Synthesis

5.2.2.1. General Synthesis of PbTe Nanoparticles and Ligand Removal

The PbTe nanoparticles were synthesized using the protocol mentioned in Chapter 3. The dried nanoparticles were either treated with (1) anhydrous hydrazine, where the PbTe nanoparticles were dispersed in hexane and added to a 1:1 volume ratio of anhydrous hydrazine in the glove box and stirred until the hexane phase becomes colorless. The upper colorless organic phase was discarded and acetonitrile in 2:1 volume ratio was added to the PbTe hydrazine phase which caused flocculation of the PbTe nanoparticles. Alternatively, (2) the nanoparticles were thermally annealed at 410 °C under inert atmosphere for 2 h in order to remove surface ligands.

5.2.2.2 General Synthesis of n-type and p-type Bismuth Telluride (Performed by Collaborators at MSU)

Bismuth antimony telluride with nominal composition $Bi_{0.4}Sb_{1.6}Te_3$ was employed as the p-type matrix material for making nanocomposites; for n-type, we chose to alloy bismuth telluride with bismuth selenide for a nominal composition $(Bi_2Te_3)_{0.95}(Bi_2Se_3)_{0.05}$, yielding the formula $Bi_2Te_{2.85}Se_{0.15}$. High purity elements were weighed according to the targeted ratio and sealed in a fused silica ampoule under a vacuum < 10^{-5} Torr. The ampoule was heated at 750 °C for 12 h followed by rapid water quenching. The quenched ingot was annealed for another three days in

order to homogenize the properties. The annealing temperatures were carefully selected to optimize the overall thermoelectric transport properties. For n-type, the annealing temperature is set at 450 °C and for p-type, it is 540 °C. The annealed ingot was then ball milled into fine powders in a Spex 8000 Mixer/Mill and stored inside an Ar purged glovebox before making nanocomposites.

5.2.2.3. General Synthetic Procedure for Incorporation of PbTe Nanoparticles into Bulk Bismuth Telluride (n- or p- doped) Matrix

The synthesis of nanocomposites involved dispersion of an appropriate mass of oleate-capped PbTe nanoparticles into a minimum amount of solvent, hexane. The resulting solution was sonicated for 10 min to make a colloidal suspension. The PbTe nanoparticle sol was then added dropwise to an appropriate mass of bulk bismuth telluride (n- or p-doped) matrix with constant stirring, followed by solvent evaporation under ambient temperature and pressure, in a glove box.

The mixed composite powder was loaded into a graphite crucible and heated at 410 °C for 2 h in an Ar purged glove box in order to eliminate residual organics at the surface of the PbTe nanoparticles. The heat treated powder was then hot pressed between 350 °C and 380 °C under a pressure of 60 MPa for 15 min to form a dense pellet. For n-type nanocomposite a total of five samples (2 g each) were prepared with PbTe weight percentages 10, 5, 1, 0.1 and 0 wt%; and for p-type nanocomposite, a total of four samples (2 g each) with PbTe weight percentage of 0%, 0.1%, 0.5% and 1% were prepared.

5.3 Characterizations

PXRD, TEM, IR, TGA and thermoelectric property measurements (Seebeck coefficient, electrical resistivity, thermal conductivity and Hall coefficient) were used to characterize the materials. For more details on the measurement technique, refer to Chapter 2.

5.4 Results and Discussion

5.4.1 Synthesis of PbTe Nanoparticles and Bulk n- and p-doped Bismuth Telluride Matrix

We expected that the presence of uniform PbTe nanoparticles within a bismuth telluride bulk material doped with either Se (n-type) or Sb (p-type), would result in heterogeneous interfaces that would scatter phonons and thus reduce the thermal conductivity (κ) within the matrix (particularly the lattice part of the thermal conductivity, κ_l), while having minimal impact on the electrical properties. To obtain a nanocomposite, we first prepared PbTe nanoparticles, bulk $Bi_{2-x}Sb_xTe_3$ and $Bi_2Te_{3-x}Se_x$ independently, and then incorporated PbTe into the bulk bismuth telluride matrix via incipient wetness impregnation.

The p-type $Bi_{2-x}Sb_xTe_3$ and n-type $Bi_2Te_{3-x}Se_x$ were prepared following literature procedures[86, 87] targeting the composition $Bi_{0.4}Sb_{1.6}Te_3$ and $Bi_2Te_{2.85}Se_{0.15}$, respectively. The compositions were chosen where the electrical and thermal characteristics balance to generate the maximum ZT within the homogeneous p-doped or n-doped alloy. These materials were prepared by our collaborators at MSU. The ball milled powders were characterized by powder X-ray diffraction (PXRD) patterns and were found to match the expected rhombohedral phase of Bi_2Te_3.

Oleate-capped PbTe nanoparticles were synthesized by modification of a literature procedure as previously reported in Chapter 3. The PXRD pattern of the nanoparticles matches the cubic PbTe (Altaite) phase and the crystalline size is 13-14 nm, determined using the Scherrer

equation. TEM images reveal that the particles exhibit a cubic morphology with an average particle size of 13 ± 1.2 nm, consistent with the Scherrer equation. Similar sizes were obtained for the nanoparticles employed with the n-type composites. The elemental analysis (EDS) of the as-prepared nanoparticles gives a composition Pb:Te of 1:0.94, close to the ideal value of Pb:Te of 1:1.

5.4.2 Removal of Organic Surface Ligands from PbTe Nanocrystals

The oleate groups bonded to the surface of PbTe nanoparticles can be expected to act as insulating barriers, decreasing the overall electrical conductivity of the system.[30, 78] Hence, we sought to remove the oleate ligands, using both chemical and thermal treatments. For the chemical treatments, PbTe nanoparticles dispersed in hexane were treated with anhydrous hydrazine with stirring, followed by precipitation with acetonitrile, following the literature procedure.[78] Hydrazine treatment led to some ripening, manifest as a slight increase in the crystallite size from 14 nm to 15 nm (Scherrer analysis of PXRD pattern) with significant aggregation. A comparison of infrared spectra (IR) obtained before and after hydrazine treatment, is shown in **Figure 5.1.** The peaks at 1512 cm^{-1} and 1394 cm^{-1} are attributed to the presence of symmetric and asymmetric vibrations of oleate COO^-, respectively, whereas those at 2918 cm^{-1} and 2840 cm^{-1} correspond to aliphatic –CH stretches. While significant reduction in peak intensity is observed upon hydrazine treatment, the IR data suggest that complete removal is not achieved.

Thermal treatment was found to be more effective for oleate group removal. The optimum temperature was determined by thermogravimetric analysis (TGA). As shown in **Figure 5.2**, the TGA of the oleate-capped PbTe nanoparticles revealed a 16 % weight loss overall between 255-455 °C, which we attribute to desorption/decomposition of surface oleate functionalities as well

as possible loss of Te due to sublimation at the high temperature end of the measurement. However, the loss of Te is expected to be less than 1 wt % under these conditions.[88] Based on the TGA data, heat treatment of the nanoparticles was carried out in a flow furnace at 410 °C for 2 h under nitrogen. As shown in **Figure 5.1**, both $–COO^-$ and –CH stretching vibrations are absent after thermal treatment, suggesting successful removal of the organic groups.

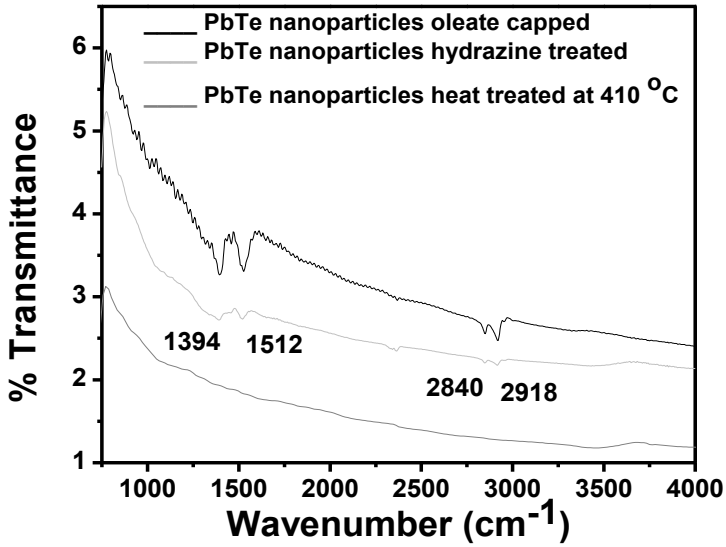

Figure 5.1 IR of PbTe oleate-capped nanoparticles, hydrazine-treated PbTe nanoparticles and thermally-treated PbTe nanoparticles under Ar in a flow furnace at 410 °C.

5.4.3 Nanocomposite Preparation and Characterization

In order to avoid aggregation and particle growth during the thermal ligand removal step, and to enable the most efficient and intimate mixing between the nanoparticles and the matrix, the incorporation of nanoparticles into bulk bismuth telluride (n- and p- doped) was achieved by addition of a dispersion of oleate-capped PbTe nanoparticles in hexane to solid $Bi_2Te_{3-x}Se_x$ and $Bi_xSb_{2-x}Te_3$ dropwise, with constant stirring of the slurry to facilitate incorporation of the PbTe nanoparticles throughout the matrix, then left to dry under inert atmosphere. The resultant composite was then placed inside a carbon crucible and heated at 410 °C for two hours to

pyrolyze organic ligands encapsulating the PbTe nanoparticles. The heat treated powder was then hot pressed inside a 10 mm graphite die under a pressure of 60 MPa at an approximate temperature of 350 °C to 390 °C for 15 min. A total of four nanocomposites with 10 wt %, 5 wt %, 1 wt % and 0.1 wt % for the n-type matrix, and three nanocomposites with 0.1 wt%, 0.5 wt% and 1 wt% PbTe nanoparticles for the p-type matrix, were prepared. A pure bismuth antimony telluride and bismuth selenium telluride matrix material was hot pressed under identical conditions to serve as a control sample.

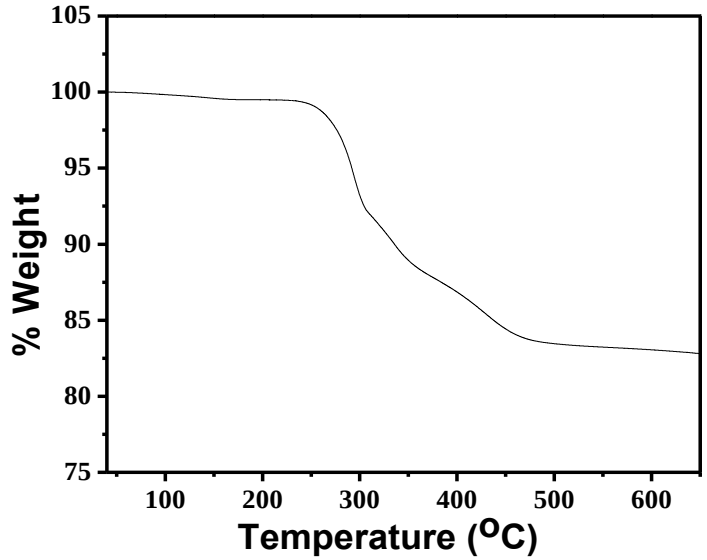

Figure 5.2 TGA of PbTe oleate-capped nanoparticles under N_2 atmosphere.

Figure 5.3 demonstrates the PXRD pattern of n-type and p-type composites showcasing the 10 and 1 wt % patterns for the former and 1 wt % for the latter. PbTe nanoparticles within the $Bi_2Te_{3-x}Se_x$ and $Bi_{2-x}Sb_xTe_3$ nanocomposites could not be detected by PXRD at the low concentrations (**Figure 5.3**) due to limitations in the sensitivity of the PXRD instrument, but the 10 wt % nanocomposite shows the presence of the most intense (220) reflection of Altaite, suggesting PbTe remains a discrete phase within the $Bi_2Te_{3-x}Se_x$ matrix under these processing conditions. For the case of p-type composites, the effect of incorporating PbTe nanoparticles into

the $Bi_{2-x}Sb_xTe_3$ matrix on the lattice parameters of the matrix was evaluated. Incorporation of nanoparticles had no definitive effect on the lattice parameters, which were found to be the same within 2σ (**Table 5.1**) for comparison of the matrix to the highest p-type doped material (1 wt %). However, this does not rule out solid-solution formation, since the doping levels are small and minimal changes in lattice parameter are expected.

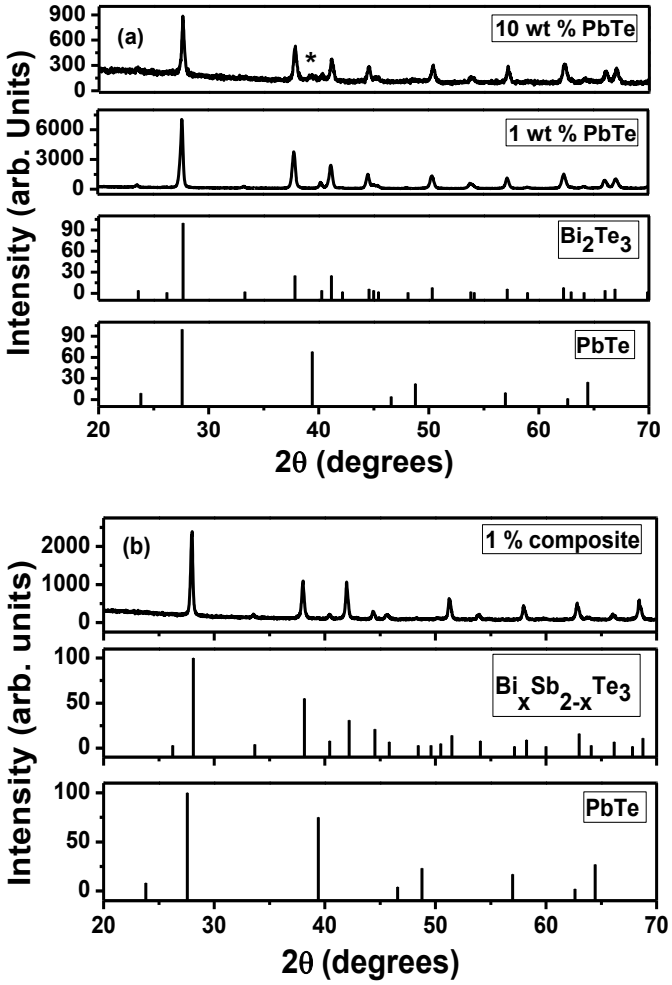

Figure 5.3 (a) PXRD of 10 and 1 wt % of PbTe in $Bi_2Te_{3-x}Se_x$ matrix after compaction and (b) PXRD of 1 wt % of PbTe in $Bi_{2-x}Sb_xTe_3$ matrix after compaction. The patterns are referenced to the ICDD-PDF # 38-1435 of cubic PbTe and ICDD-PDF # 15-0863 of rhombohedral Bi_2Te_3 and rhombohedral $Bi_xSb_{2-x}Te_3$. The (*) shows the (220) reflection of the Altaite phase of PbTe.

The incorporation of PbTe nanoparticles in doped bismuth telluride matrix was further confirmed by TEM images. **Figure 5.4** shows the images of the precursor nanoparticles as well as composites of 10, 5, 1 and 0.1 wt % of PbTe in $Bi_2Te_{3-x}Se_x$ matrix and **Figure 5.5** shows the TEM images of PbTe nanoparticles, 1 wt %, 0.5 wt % and 0.1 wt % of PbTe nanoparticles in the $Bi_{2-x}Sb_xTe_3$ matrix. The presence of higher contrast 12-13 nm sized cubes similar to those seen in the discrete PbTe nanoparticle samples is evident in all images, with fewer detected at lower concentrations inside the lighter contrast bulk matrices. The presence of PbTe nanoparticles was evident throughout the matrix in all cases and showed no agglomeration, suggesting good dispersion.

5.5 Transport Properties (Acquired by Collaborator Dr. Chen (Kevin) Zhou, in Morelli's Laboratory at Michigan State University)

For the sake of simplicity, we use the weight percentage, x, of PbTe nanoparticles to identify our samples. **Figure 5.6** displays the temperature dependence of electronic properties for our nanocomposite samples employing the n-type matrix as well as the control sample, x=0 for $Bi_2Te_{3-x}Se_x$. As mentioned in Chapter 1, the Seebeck Coefficient (S) measures the voltage change for a temperature gradient. The sign of the S reflects the majority carriers in the system. Introduction of PbTe nanoparticles in the n-doped matrix results in a decrease of Seebeck coefficient, shown in **Figure 5.6**, with a cross-over to positive values at higher wt % of PbTe. The electrical resistivity of the composites increases by an order of magnitude upon PbTe incorporation. Combining both the parameters, it was found that the thermoelectric power factor ($S^2\sigma$) of nanocomposites is significantly lower than the control sample (**Figure 5.6)**.

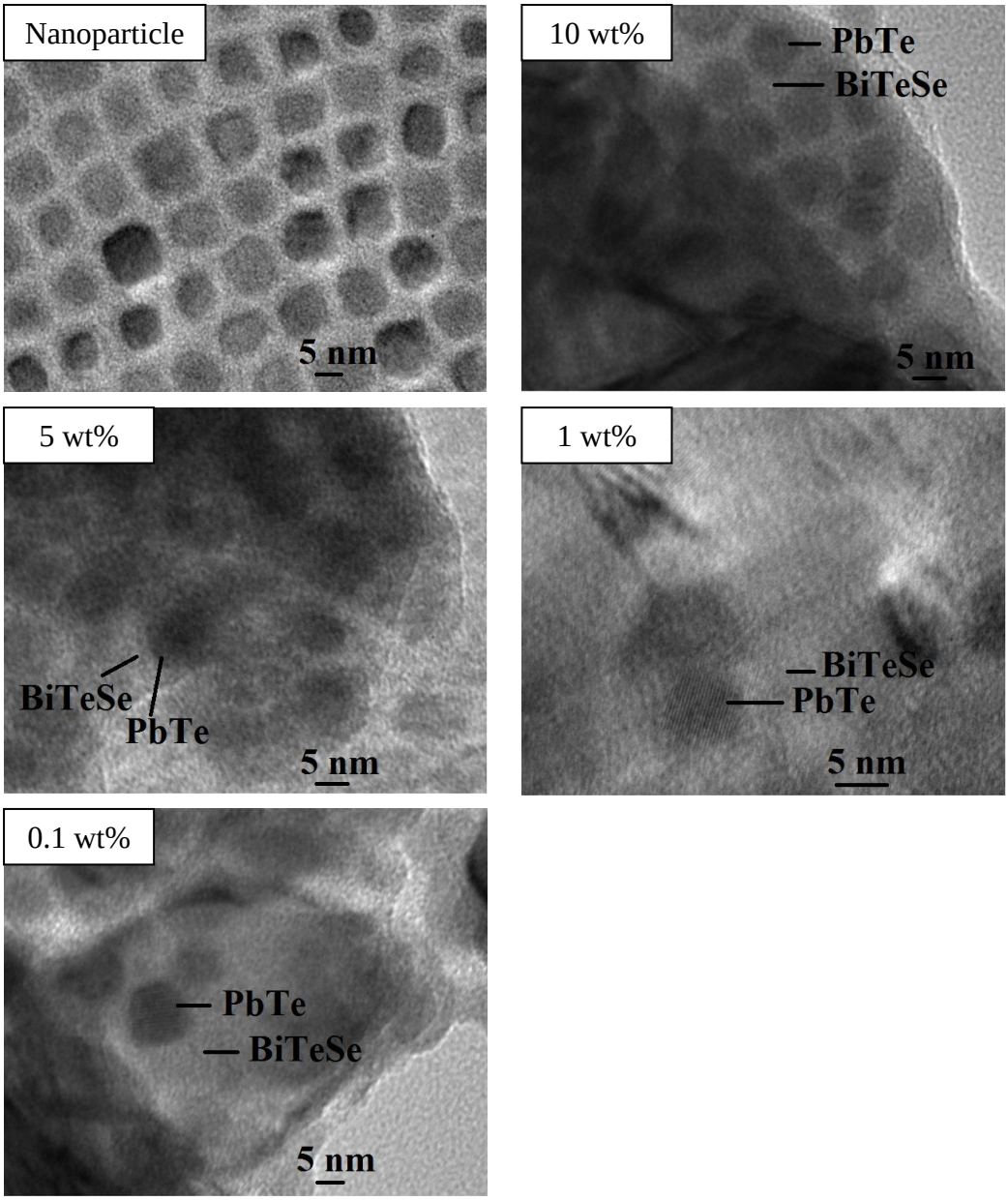

Figure 5.4 TEM images of discrete PbTe nanoparticles, 10 wt%, 5 wt%, 1 wt % and 0.1 wt% PbTe nanoparticles in BiTeSe nanocomposites.

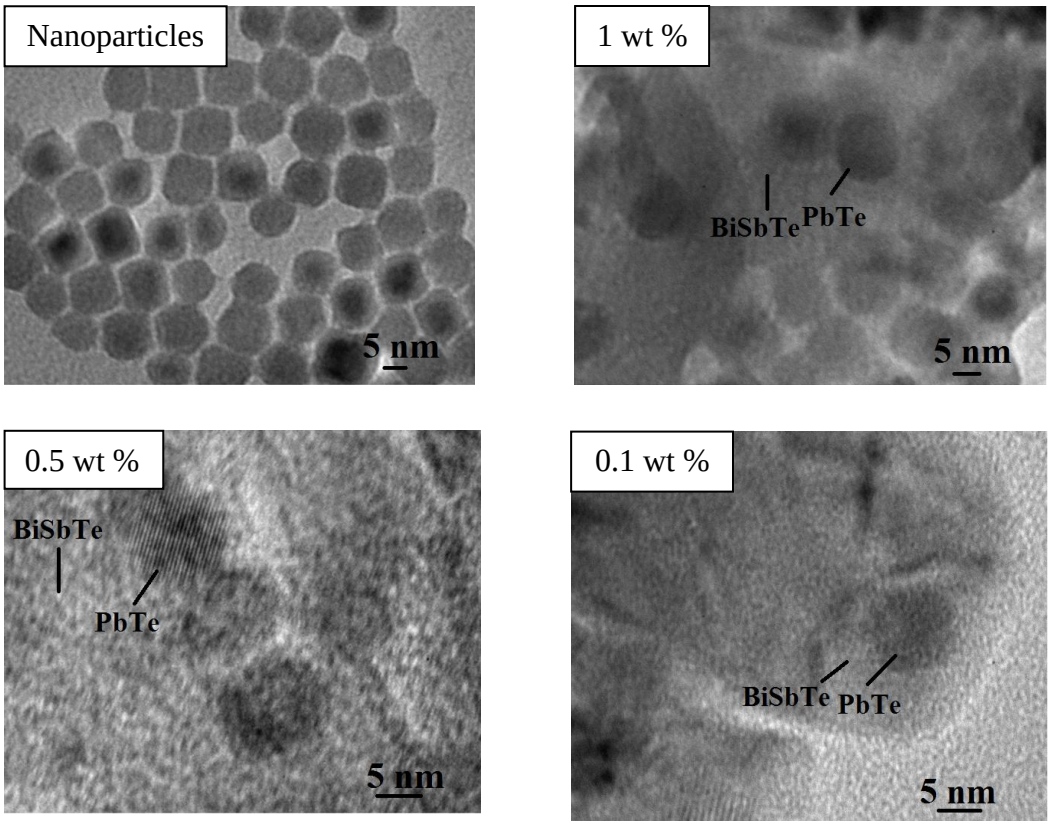

Figure 5.5 TEM images of discrete PbTe nanoparticles, 1 wt%, 0.5 wt% and 0.1 wt% PbTe nanoparticles in BiSbTe nanocomposites.

The suppression of S and the cross-over to a positive value at higher wt % as well as the decrease in electrical transport suggests that PbTe is compensating the majority carriers by producing holes and thus leading to a two-charge carrier system rather than a one-charge carrier system. Thus, for the case of n-type composites, the presence of extra holes, increasing with the increase in wt % of PbTe in the matrix, compensated the majority charge carriers, electrons, leading to crossover from n to p type at higher loading levels and an overall reduction in ZT.

. **Figure 5.7** shows the total thermal conductivity and lattice thermal conductivity data as a function of temperature. The lattice thermal conductivity, κ_l, shown in **Figure 5.7** was calculated

by subtracting the electronic thermal conductivity, κ_e, from the total thermal conductivity. The electronic thermal conductivity is estimated by using the Wiedemann-Franz law, $\kappa_e = L\sigma T$; where L is the Lorenz number, σ the electrical conductivity and T the absolute temperature. The value of Lorenz number used here is for a degenerate semiconductor, 2.45×10^{-8} $W\Omega/K^2$. This value is generally used for metals and heavily doped semiconductors.[4] However, in our case this value of Lorenz number is only a poor approximation as our materials are partially degenerate semiconductors. This results in a significant error in the calculated lattice thermal conductivity values. Overall, the thermal conductivities of the composites are similar to the control sample and there is no expected decrease in κ_l that could be attributed to phonon scattering from PbTe nanoparticles.

Figure 5.8 shows the dimensionless thermoelectric figure of merit, ZT, as a function of temperature. ZT's of nanocomposites are considerably reduced compared to matrix $Bi_2Te_{3-x}Se_x$, as all the parameters, S, σ and κ, are reduced with the addition of PbTe nanoparticles. A significant ZT reduction starts at PbTe wt % as little as 0.1. Since the composites prepared by incorporation of PbTe nanoparticles in n-Bi_2Te_3 matrix are electronically compensated, resulting in poor ZT, matrices that are already hole doped, such as p-Bi_2Te_3 matrix were explored, thereby avoiding compensation.

For p-type Bi_2Te_3, four different composites were prepared 0, 0.1, 0.5 and 1 PbTe wt %: These low values for incorporation were chosen based on data acquired with n-type, where properties changed minimally after 1 wt % loading. **Table 5.1** lists some of the room temperature physical properties for the series of hot pressed nanocomposites. **Figure 5.9** displays the temperature dependence of electronic properties for our p-type nanocomposite samples as well as the control sample, x = 0. The Seebeck coefficients of nanocomposites decrease monotonously

with increasing concentration of PbTe nanoparticles. The electrical resistivity exhibits the same trend, except that x = 0.1 and x = 0.5 have nearly identical resistivity

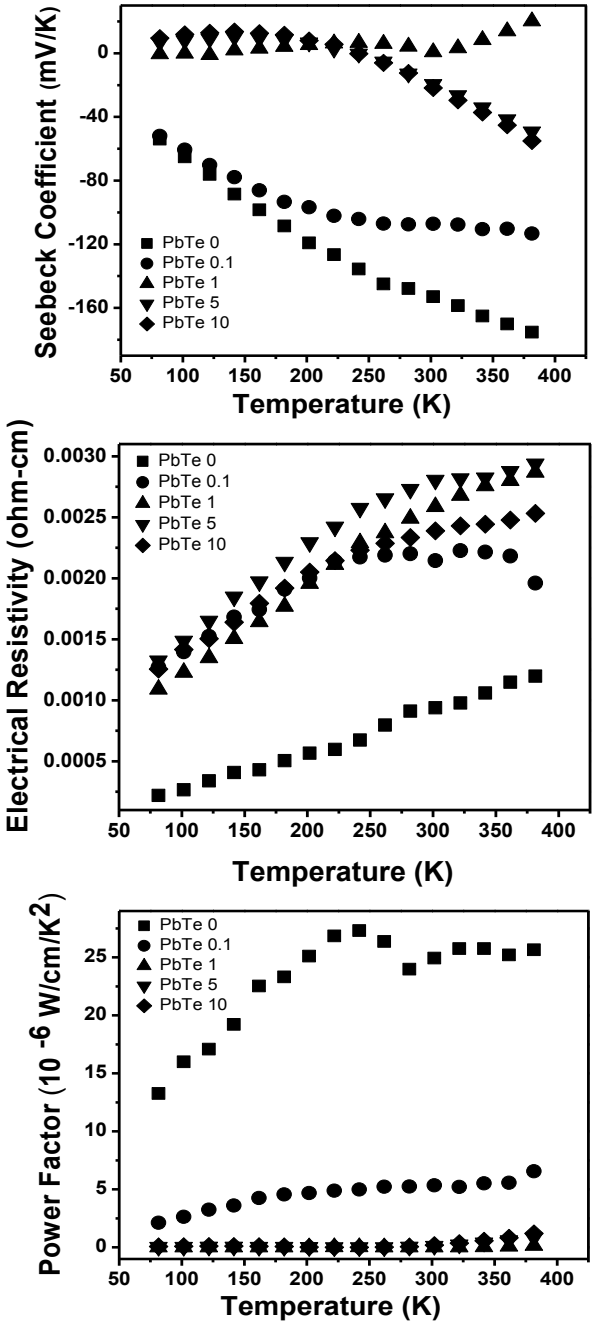

Figure 5.6 Electronic properties of nanocomposites formed from PbTe nanoparticles and n-type $Bi_2Te_{3-x}Se_x$ as a function of temperature.

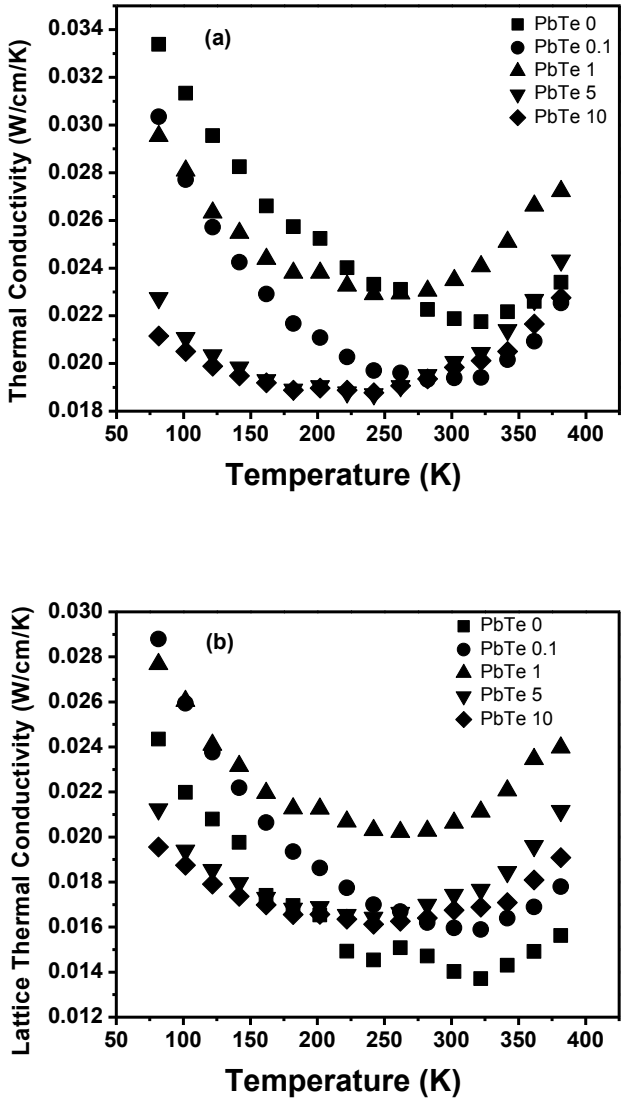

Figure 5.7 (a) Total thermal conductivity and (b) lattice thermal conductivity of nanocomposites formed from PbTe nanoparticles and n-type $Bi_2Te_{3-x}Se_x$ as a function of temperature.

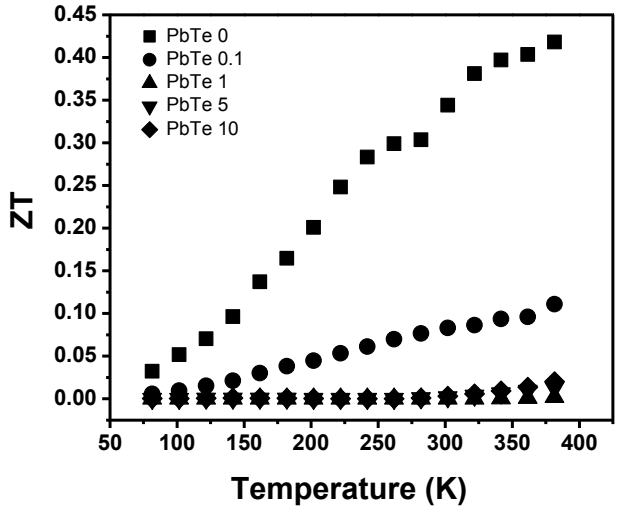

Figure 5.8 Figure of merit ZT, formed from PbTe nanoparticles and n-type $Bi_2Te_{3-x}Se_x$ as a function of temperature.

Table 5.1 Some room temperature (300 K) physical properties of $PbTe/Bi_{2-x}Sb_xTe_3$ nanocomposites.

Sample name	x = 0 (control)	x = 0.1	x = 0.5	x = 1
PbTe nanoparticles weight percentage	0%	0.1%	0.5%	1%
Lattice parameters (Å) and standard deviations	a = 4.2884 (13) c = 30.459 (8)	ND	ND	a = 4.2856 (19) c = 30.443 (15)
Relative density	95.74%	97.09%	96.32%	94.15%
Seebeck coefficient (10^{-6} V/K)	186	136	110	84
Electrical resistivity (mΩ cm)	1.14	0.672	0.688	0.500
Power factor (10^{-6} $Wcm^{-1}K^{-2}$)	30.15	26.48	18.11	15.37
Thermal conductivity (10^{-2} W/cm-K)	1.48	1.65	1.71	1.81
Lorenz number (10^{-8} $W\Omega K^{-2}$)	1.65	1.78	1.82	2.00
Carrier density (10^{-19} cm^{-3})	3.68	5.41	7.90	10.8

.

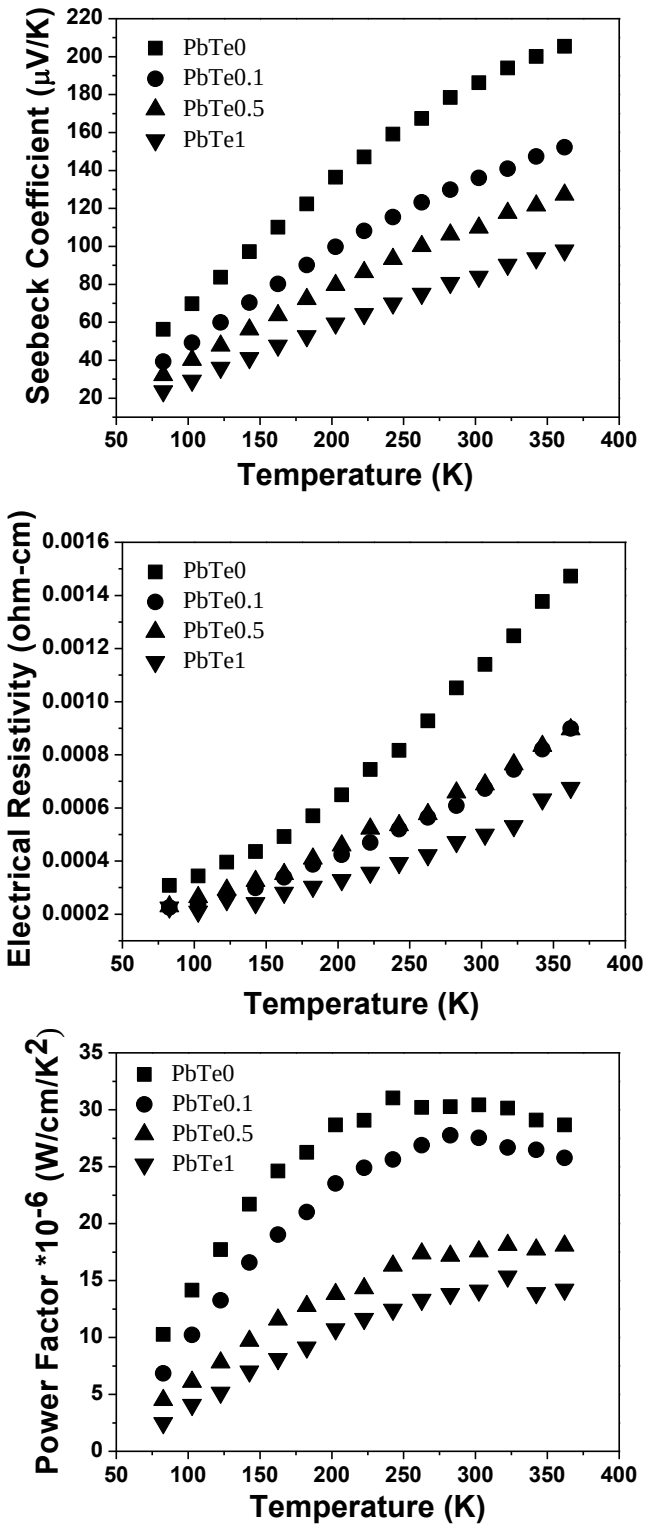

Figure 5.9. Electronic properties of nanocomposites formed from PbTe nanoparticles and p-type $Bi_{2-x}Sb_xTe_3$ as a function of temperature.

Despite the decrease in resistivity, the thermoelectric power factors ($S^2\sigma$) of nanocomposites are lower than the control sample due to the much stronger contribution of the Seebeck coefficient. **Figure 5.10** shows the corresponding thermal conductivity data as a function of temperature. As mentioned earlier, the choice of a reasonable Lorenz number in the Wiedemann-Franz law, $\kappa_e = L\sigma T$, is a delicate issue as we cannot assume our samples to be degenerate semiconductors. We also note that there is approximately a factor of three difference between the most resistive and least resistive samples, so one Lorenz number may not fit all the data equally well. To tackle this problem, Lorenz numbers for each nanocomposite were calculated (based on equations given in the literature) to determine the lattice thermal conductivity.[4] Based on this data (see **Table 5.1**), we found that, despite an overall increase in total thermal conductivity, the nanocomposite samples exhibit a reduced lattice thermal conductivity compared to the control sample, as expected if the nanoscale interfaces are acting to scatter phonons. The lattice thermal conductivity of sample x = 1 is reduced by close to 50 % compared to the control sample. Thus, it appears that the overall increase in thermal conductivity can be attributed to the increase in electrical conductivity causing an increase in κ_e. It is likely that the same process is occurring in n-type materials (phonon scattering) but is obscured unless a rigorous treatment of the contribution of the lattice to the total thermal conductivity is computed as has been done for p-type.

Figure 5.11 shows the dimensionless thermoelectric Figure of Merit, ZT, as a function of temperature. ZT's of nanocomposites are reduced compared to matrix $Bi_{2-x}Sb_xTe_3$, with the strongest contributing factor the decreased Seebeck coefficient. A significant ZT reduction starts at PbTe wt% as little as 0.5.

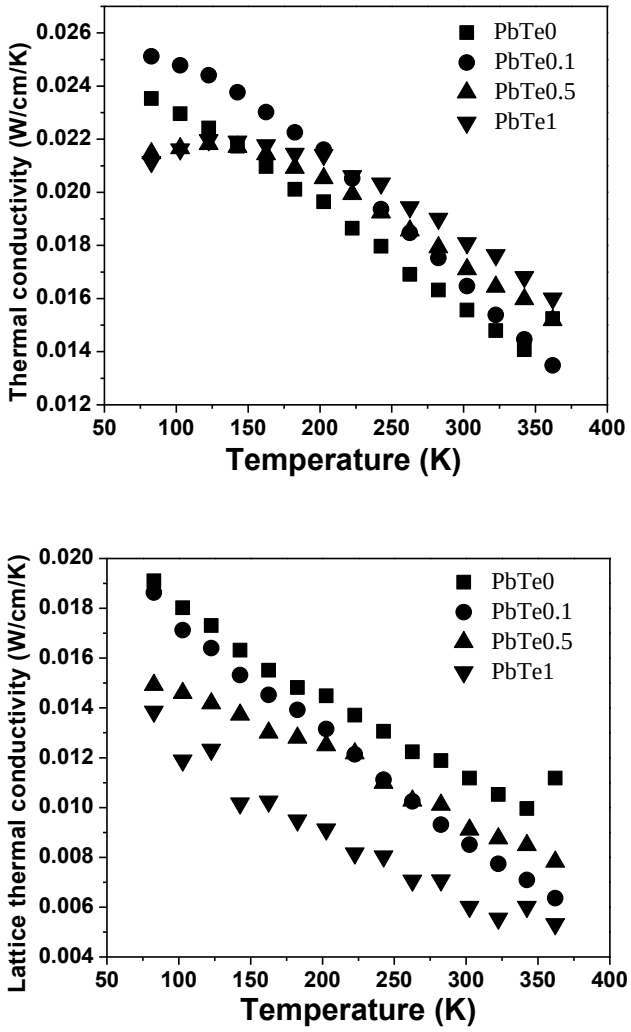

Figure 5.10 Total thermal conductivity and lattice thermal conductivity of nanocomposites formed from PbTe nanoparticles and p-type $Bi_{2-x}Sb_xTe_3$ as a function of temperature.

In order to discern the origin of the strong electronic effects noted upon PbTe nanoparticle incorporation, carrier concentration was measured as a function of temperature **(Figure 5.12).** The hole concentration increases with increasing PbTe concentration, suggesting the incorporation of PbTe nanoparticles is also introducing a p-type dopant. This is consistent with our work in the n-type system, as well as work by Kusano and coworkers, who have attempted to

mechanically alloy bulk $Bi_{2-x}Sb_xTe_3$ and PbTe and consolidated the powder by spark plasma sintering.

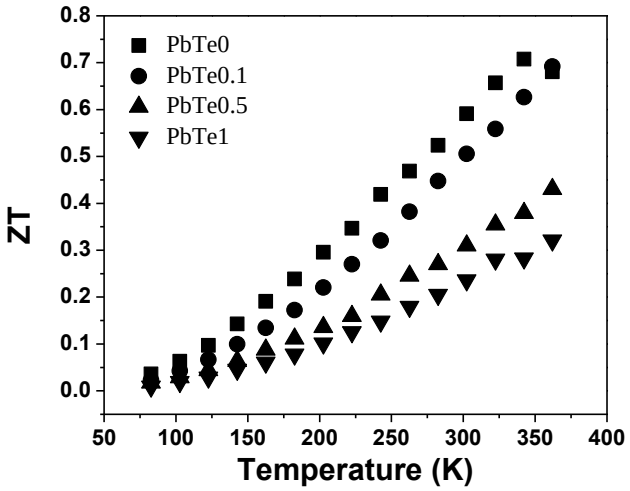

Figure 5.11 Dimensionless thermoelectric Figure of Merit, ZT, for nanocomposites formed from PbTe nanoparticles and p-type $Bi_{2-x}Sb_xTe_3$ as a function of temperature.

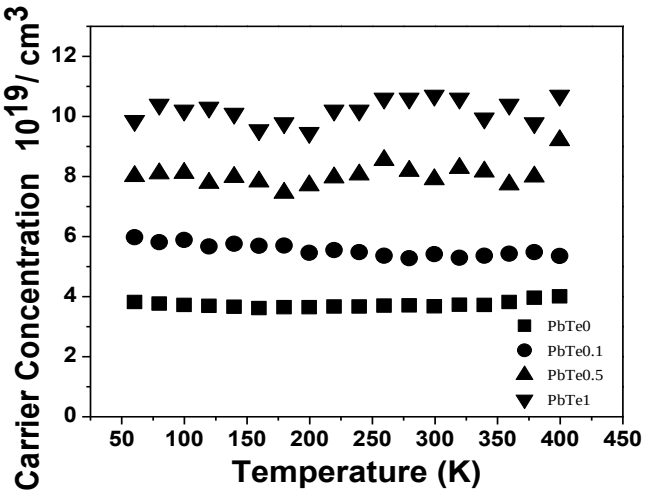

Figure 5.12 Temperature dependence of carrier concentration formed from PbTe nanoparticles and p-type $Bi_{2-x}Sb_xTe_3$ as a function of temperature.

The TE transport properties of the resultant composites exhibited a similar trend as in our study and they concluded the increase in carrier concentration is due to doping associated with PbTe.[89] This doping was attributed to either the effect of PbTe as an inclusion, since PbTe is generally a p-type semiconductor, or from Pb^{2+} leaching from the incorporated nanoparticles and occupying Bi^{3+} sites within the matrix, generating a hole, and thus increasing the overall hole concentration.[89] Pb has also been used as a p-type dopant for both Bi_2Te_3 and Sb_2Te_3, as reported by Placháček et al. where they concluded that the increase of hole concentration arises from the interaction between Pb atoms and native point defects (antisite defects or Te vacancies) in Bi_2Te_3 and Sb_2Te_3.[90, 91]

To further elucidate the effect of PbTe nanoparticle incorporation on the properties of the $Bi_{2-x}Sb_xTe_3$ matrix, we plot the Pisarenko relation of p-type $Bi_{2-x}Sb_xTe_3$ and PbTe/$Bi_{2-x}Sb_xTe_3$ nanocomposites (**Figure 5.13**). The fit line is created from a number of $Bi_{0.4}Sb_{1.6}Te_3$ samples (also prepared at Michigan State University), each displaying a different carrier concentration. From the approximate equation 5.1 (based on a simplified one carrier model),[3] for a series of samples that share the same exponent of scattering, λ, and approximately the same effective mass, m*, the Seebeck coefficient is proportional to the logarithmic inverse of the carrier concentration (n_p) and should thus fall close to the fitted line in a Pisarenko relation plot.

$$S \alpha \frac{\kappa}{e} \left[\lambda + const + \ln \frac{2\,(2\pi m^* kT)^{3/2}}{h^3 n_p}\right] \qquad (5.1)$$

As shown in **Figure 5.13**, the points representing nanocomposites fall in the vicinity of the fitted line, suggesting that the charge carrier scattering mechanism for nanocomposites is the same as for matrix materials (if we assume m* is not affected by the low percentage of PbTe incorporation). Thus, the enhanced carrier concentration appears to be due to incorporation of

Pb^{2+} in the $Bi_{2-x}Sb_xTe_3$ matrix, resulting in a decreased Seebeck coefficient, decreased resistivity, and increased κ_e. The presence of Pb^{2+} ions within the $Bi_{2-x}Sb_xTe_3$ matrix may also contribute to reduced lattice conductivity; decreased κ_l in antimony telluride doped with lead telluride has been attributed to such an ion-doping effect.[92]

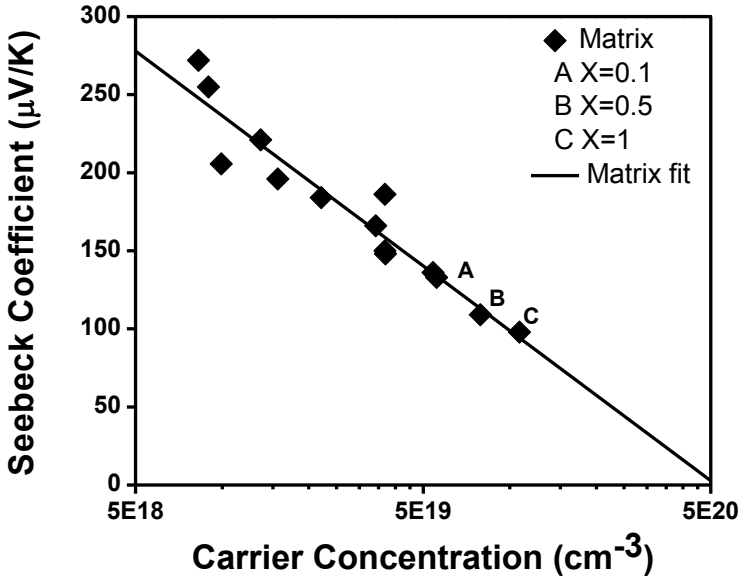

Figure 5-13. Pisarenko relation of nanocomposites formed from PbTe nanoparticles and p-type $Bi_{2-x}Sb_xTe_3$. The fitted line is constructed as an aid to guide the eye. All matrix bismuth antimony telluride with various carrier concentrations were synthesized at Michigan State University and are compared with nanocomposites formed from PbTe nanoparticles and p-type $Bi_{2-x}Sb_xTe_3$ (points A, B and C).

5.6 Conclusion

As a means to reduce lattice thermal conductivity in n and p-type bismuth telluride matrices, and thus improve thermoelectric performance, the incorporation of discrete, monodisperse 13-14 nm PbTe nanoparticle "scattering centers" was achieved using an incipient wetness approach.

Thermal-treatment of the resultant composite is effective at removing residual surface ligands from the nanoparticle preparation, and the presence of PbTe cubes within the matrix is evident after both the ligand removal (410 ºC) and hot-pressing (350-380 ºC) steps. Evaluation of the thermoelectric properties of PbTe/$Bi_2Te_{3-x}Se_x$ composites for PbTe nanoparticle loadings between 0.1 and 10 wt % showed a decrease in the magnitude of S and the electrical conductivity with a slight decrease in thermal conductivity with increase in wt % of PbTe incorporated, overall leading to decrease of ZT. This was attributed to carrier compensation from the introduction of p-type dopants from the PbTe nanoparticle in the n-type matrix. A back of the envelope calculation of the electronic contribution to the thermal conductivity suggests the slight decrease may not be due to a decrease in κ_e due to phonon scattering.

Composites of PbTe/$Bi_{2-x}Sb_xTe_3$, revealed a decrease in Seebeck coefficient and in electrical resistivity, also attributed to an increase in hole carrier concentration. Based on the behavior of the $Bi_{2-x}Sb_xTe_3$ matrix for different carrier concentrations (Pisarenko relation), relative to the nanocomposites, it can be concluded that the carrier scattering mechanism is the same in each, i.e., the electrical properties arise from incorporation of Pb^{2+} from the PbTe nanoparticles into the $Bi_{2-x}Sb_xTe_3$ matrix. Using a more rigorous calculation method, the lattice thermal conductivity is found to decrease with the addition of PbTe nanoparticles, but this effect is small and countermanded by the changes in Seebeck, and κ_e. Moreover, in the present system we cannot differentiate between phonon scattering at nanoparticle interfaces or at defects due to Pb incorporation within the $Bi_{2-x}Sb_xTe_3$ matrix.

Chapter 6

Conclusions and Prospectus

Thermoelectric devices are those that transform heat energy into electrical energy, or vice-versa. A good thermoelectric material possesses the property of a good electrical conductor (high electrical conductivity, σ) as well as the property of a poor thermal conductor (low thermal conductivity value, κ), but also should have a high Seebeck coefficient value (S), leading to high figure of merit, ZT, where $ZT = (S^2 \sigma) T / \kappa$.[2, 8] To be competitive with commercially operating generators or refrigerators, a thermoelectric material should have ZT > 3; unfortunately the ZT's of present known bulk materials have rarely exceeded unity.[2, 5] Strategies to improve ZT have been focused on either reducing the thermal conductivity κ, or increasing Seebeck coefficient S or electrical conductivity σ; however, as these parameters are highly correlated, this has proved to be a challenge. Recently, it has been suggested that the enhancement in ZT can potentially be achieved by the creation of nanostructures.[2] This can be ascribed to a number of factors, among them are (1) quantum confinement effects in nanostructured materials resulting in increased density of states at the Fermi level, which increases the thermopower S; and (2) reduction in thermal conductivity (κ) by the introduction of interfaces and pores in the material.

This dissertation research seeked to test the hypothesis that nanostructuring can lead to enhanced figure of merit in thermoelectric materials. To test this hypothesis, PbTe and Bi_2Te_3 systems were chosen as these are well known materials (in bulk) used for thermoelectric applications, and also are relatively easy to work with as they exist in single phase form. PbTe shows a high ZT of 0.8 at 773 K; and Bi_2Te_3, a ZT of 1.0 at 300 K in the bulk form.[8] Two approaches have been used in this dissertation for nanostructuring of these materials to enhance the ZT. The first approach was to employ the sol-gel nanoparticle assembly method, developed

in the Brock Group for lighter sulfides and selenides,[43, 45, 46] to desired PbTe and Bi_2Te_3 systems. The second approach was to synthesize heterostructured nanocomposites in which the PbTe nanoparticles were incorporated inside n- or p-doped bulk Bi_2Te_3 matrix.

(1) Nanostructuring via Aerogel Formation:

Despite the readily oxidizable nature of tellurides with respect to sulfides or selenides, the oxidative sol-gel assembly was successfully employed with tellurides, and specifically to state-of-the-art TE materials like PbTe and Bi_2Te_3 (and Bi_2Te_3-Sb_2Te_3 alloys) without degrading the crystallite size, structure and crystallanity of the resulting aerogel network as compared to the precursor nanoparticles. In general, these aerogels exhibited higher BET surface areas as compared to the precursor nanoparticles and more dense xerogels, and showed broad BJH pore size distributions, extending from the micro to the macropore region. The high surface area of aerogels and xerogels as compared to the precursor nanoparticles, indicated that the supercritical drying method, employed to generate aerogels, enables better access to the particle surface. Although aerogels can be obtained from both Bi_2Te_3 and PbTe, these systems differ in their propensity to generate free-standing monoliths, with the aerogels obtained from Bi_2Te_3 nanoparticles generating robust monoliths whereas the PbTe system only generated powders.

With respect to physical properties, PbTe aerogels were studied with respect to their thermal stability, whereas Bi_2Te_3 and a Bi_2Te_3-Sb_2Te_3 alloy were evaluated with respect to their thermoelectric properties. PbTe aerogels showed augmented thermal stability as compared to the nanoparticles, as suggested by the increased onset of sublimation temperature and broadening of the sublimation temperature range for aerogels relative to nanoparticles,. Both nanoparticles and aerogels melt at the bulk melting temperature of PbTe, which is 920 °C,[72] suggesting these materials could potentially be used for high temperature thermoelectric power generators.

Unfortunately, the synthesis did not yield sufficient material for thermoelectric property measurements.

The measurement of thermoelectric properties of the Bi_2Te_3 and $Bi_xSb_{2-x}Te_3$ aerogels suggested degraded electronic properties, as compared to their respective nanoparticles, owing to poor power factor values ($S^2\sigma$). Lattice thermal conductivities of the Bi_2Te_3 aerogels were comparable to those of the precursor nanoparticles, yet they were lower than for their respective bulk materials. The reduced lattice thermal conductivity in Bi_2Te_3 aerogels is attributed to the effect of nanostructuring, which effectively scatters heat carrying phonons, leading to lower lattice thermal conductivity values than for bulk counterparts. In the case of $Bi_xSb_{2-x}Te_3$, no such lattice thermal conductivity improvements were observed; presumably, the disordered Bi-Sb lattice is responsible for the inherently low lattice thermal conductivity in the alloy. The degraded electronic properties in both materials were attributed to doping effects, which in turn reduced the overall ZT of the system.

(2) Nanocomposite Formation

Recently, considerable focus has been given to the synthesis of hetero-nanocomposite materials[85] for improved figure of merit (ZT) in thermoelectric devices, as inclusion of nanoscale features in the bulk matrices dramatically reduces the thermal conductivity and hence improves the thermopower (S) of the system.[2, 25] In this dissertation research, in an effort to further enhance the ZT of an already established thermoelectric material, studies were done to synthesize heterostructured nanocomposites of PbTe nanoparticles incorporated inside bulk n-type and p-type Bi_2Te_3 matrices via a solution based approach called the incipient wetness method. The main motivation was the potential reduction in the lattice thermal conductivity by incorporating PbTe nanoparticles to act as phonon scattering centers. The solution based

approach gave us full control on the size of the nanoparticle incorporated inside the bulk matrix. Evaluation of the thermoelectric properties of samples where different weight percents of PbTe nanoparticles were incorporated in n- and p-type Bi_2Te_3 matrices showed that the power factor of these nanocomposites degraded with the incorporation of PbTe nanoparticles. This was attributed to the doping effect, which led to carrier compensation from the introduction of p-type dopants from the PbTe nanoparticles in the n-type matrix, or an increase in the overall hole concentration in the p-type nanocomposites. On the other hand, an improved thermal conductivity was seen as compared to the p-type bulk matrix when PbTe nanoparticles were incorporated, indicating that the incorporation of PbTe nanoparticles in the bulk matrix does help in scattering heat carrying phonons thereby reducing the lattice thermal conductivity of the system.

The results from both approaches (aerogel vs. heteronanocomposite) demonstrates that nanostructuring can reduce lattice thermal conductivity values relative to bulk materials, but also underscores the sensitivity of electronic properties to doping. Future studies need to address doping effects, maximize interfacial electronic conductivity, and preserve nanostructuring in order to obtain augmented ZT values. Several directions for future study are recommended.

To improve interfacial electronic conductivity, the surface capping (organic) ligands could be replaced by all-inorganic capping ligands like molecular metal chalcogenides (MCCs),[32] which could then be linked with metal cations like Pt^{2+} or Ni^{2+} via a metathesis reaction[39, 93] to lead to all-inorganic gel networks. This would also help in keeping the crystallite size of the precursor nanoparticles unaltered as annealing (used to remove surface organic ligands) does result in some degree of sintering. While processing the materials for thermoelectric property measurements, spark plasma sintering (where the heat is generated internally) could be more beneficial rather than hot pressing (where the heat is provided by external sources) as hot

pressing further increases the crystallite size, destroys the aerogel network, and volatilizes some components (resulting in different doping characteristics). Ideally, to avoid any destruction of the aerogel network, a solution based approach for preparing thin films of aerogel materials is desirable. This would retain the pore-matter interface as well as the nanoparticle connectivity in the aerogel network. This can be achieved using thin-film gelation technique currently being developed in the laboratory. Finally, with respect to hetero-nanocomposite formation, we would like to incorporate materials that can act as phonon scattering centers without altering the electronic properties of heterostructured nanocomposites. Initial efforts toward the preparation of heterostructured nanocomposites like PbS nanoparticles within a PbTe bulk matrix are underway.

APPENDIX

Nanoparticles Change The Ordering Pattern of *n*-carboxylic Acids into Nanorods on HOPG

In addition to my dissertation research, I also participated in a collaborative effort with the group of Dr. Guangzhou Mao from the Department of Chemical Engineering and Materials Science at Wayne State University. My role in this project was to prepare MUA-capped and MPA-capped CdSe nanoparticles (where MUA is 11-mercaptoundecanoic acid and MPA is 3-mercatopropropanoic acid) of different sizes, which were further used as seeds for nucleation of long chain carboxylic acids. This work has been published in *ACS Nano*, DOI:10.1021/nn102184y,[94] and has been appended to this dissertation, upon request of my committee members, in its original published form.

REFERENCES

1. T. M. Tritt and M. A. Subramanian, *MRS Bull.*, 2006, **31**, 188-198.
2. M. S. Dresselhaus, G. Chen, M. Y. Tang, R. Yang, H. Lee, D. Wang, Z. Ren, J.-P. Fleurial and P. Gogna, *Adv. Mater.* , 2007, **19**, 1043-1053.
3. A. F. Ioffe, *Semiconductor Thermoelements, and Thermoelectric Cooling*, Infosearch Ltd., 1957.
4. H. J. Goldsmid, *Applications of Thermoelectricity*, John Wiley & Sons Inc., New York, 1960.
5. G. J. Snyder and E. S. Toberer, *Nat. Mater.*, 2008, **7**, 105-114.
6. J. Yang and T. Caillat, *MRS Bull.*, 2006, **31**, 224-229.
7. A. Majumdar, *Science* 2004, **303**, 777-778.
8. T. M. Tritt and M. A. Subramanian, *MRS Bull.*, 2006, **31**, 188-198.
9. C. J. Vineis, A. Shakouri, A. Majumdar and M. G. Kanatzidis, *Adv. Mater.*, 2010, **22**, 3970-3980.
10. G. A. Slack, *CRC Handb. Thermoelectr.*, 1995, 407-440.
11. G. S. Nolas, J. Poon and M. Kanatzidis, *MRS Bull.*, 2006, **31**, 199-205.
12. B. C. Sales, D. Mandrus and R. K. Williams, *Science* 1996, **272**, 1325-1328.
13. T. He, J. Chen, H. D. Rosenfeld and M. A. Subramanian, *Chem. Mater.*, 2006, **18**, 759-762.
14. A. Saramat, G. Svensson, A. E. C. Palmqvist, C. Stiewe, E. Mueller, D. Platzek, S. G. K. Williams, D. M. Rowe, J. D. Bryan and G. D. Stucky, *J. Appl. Phys.*, 2006, **99**, 023708/1-5.

15. V. L. Kuznetsov, L. A. Kuznetsova, A. E. Kaliazin and D. M. Rowe, *J. Appl. Phys.*, 2000, **87**, 7871-7875.

16. L. D. Hicks and M. S. Dresselhaus, *Phys. Rev. B Condens. Matter*, 1993, **47**, 12727-12731.

17. L. D. Hicks and M. S. Dresselhaus, *Phys. Rev. B Condens. Matter*, 1993, **47**, 16631-16634.

18. V. Rotello, *Nanoparticles: Building Blocks for Nanotechnology*, Springer, 2004.

19. A. R. West, *Basic Solid State Chemistry*, John Wiley & Sons, 1998.

20. R. S. Yadav, P. Mishra, R. Mishra, M. Kumar and A. C. Pandey, *Ultrason. Sonochem.*, 2009, **17**, 116-122.

21. D. O. Banga, R. Vaidyanathan, X. Liang, J. L. Stickney, S. Cox and U. Happeck, *Electrochim. Acta*, 2008, **53**, 6988-6994.

22. T. Koga, S. B. Cronin, M. S. Dresselhaus, J. L. Liu and K. L. Wang, *Appl. Phys. Lett.*, 2000, **77**, 1490-1492.

23. T. C. Harman, P. J. Taylor, M. P. Walsh and B. E. LaForge, *Science*, 2002, **297**, 2229-2232.

24. J. R. Sootsman, D. Y. Chung and M. G. Kanatzidis, *Angew. Chem., Int. Ed.*, 2009, **48**, 8616-8639.

25. K. Biswas, J. He, Q. Zhang, G. Wang, C. Uher, V. P. Dravid and M. G. Kanatzidis, *Nat. Chem.*, 2011, **3**, 160-166.

26. R. F. C. Farrow, *Molecular Beam Epitaxy: Applications to Key Materials*, Noyes Publication, 1995.

27. W. Kim, J. Zide, A. Gossard, D. Klenov, S. Stemmer, A. Shakouri and A. Majumdar, *Phys Rev Lett*, 2006, **96**, 045901.

28. J. R. Sootsman, R. J. Pcionek, H. Kong, C. Uher and M. G. Kanatzidis, *Chem. Mater.*, 2006, **18**, 4993-4995.

29. J. P. Heremans, C. M. Thrush and D. T. Morelli, *Phys. Rev. B Condens. Matter Mater. Phys.*, 2004, **70**, 115334/1-5.

30. D. V. Talapin and C. B. Murray, *Science*, 2005, **310**, 86-89.

31. M. V. Kovalenko, M. Scheele and D. V. Talapin, *Science*, 2009, **324**, 1417-1420.

32. M. V. Kovalenko, B. Spokoyny, J.-S. Lee, M. Scheele, A. Weber, S. Perera, D. Landry and D. V. Talapin, *J. Am. Chem. Soc.*, 2010, **132**, 6686-6695.

33. N. Husing and U. Schubert, *Angew. Chem., Int. Ed.*, 1998, **37**, 22-45.

34. C. Brinker and G. Scherer, *Sol-Gel Science: The Physics and Chemistry of Sol-Gel Processing*, Academic press, 1990.

35. A. C. Pierre and G. M. Pajonk, *Chem. Rev.*, 2002, **102**, 4243-4265.

36. M. A. Aegerter, *Aerogel Handbook*, Springer, 2011.

37. J. E. Murphy, M. C. Beard, A. G. Norman, S. P. Ahrenkiel, J. C. Johnson, P. Yu, O. I. Micic, R. J. Ellingson and A. J. Nozik, *J. Am. Chem. Soc.*, 2006, **128**, 3241-3247.

38. K. K. Kalebaila, D. G. Georgiev and S. L. Brock, *J. Non-Cryst. Solids*, 2006, **352**, 232-240.

39. S. Bag, P. N. Trikalitis, P. J. Chupas, G. S. Armatas and M. G. Kanatzidis, *Science* 2007, **317**, 490-493.

40. T. Gacoin, K. Lahlil, P. Larregaray and J. P. Boilot, *J. Phys. Chem. B*, 2001, **105**, 10228-10235.

41. T. Gacoin, L. Malier and J.-P. Boilot, *J. Mater. Chem.*, 1997, **7**, 859-860.

42. S. Bag, A. F. Gaudette, M. E. Bussell and M. G. Kanatzidis, *Nat. Chem.*, 2009, **1**, 217-224.

43. J. L. Mohanan and S. L. Brock, *J. Non-Cryst. Solids*, 2004, **350**, 1-8.

44. I. U. Arachchige, J. L. Mohanan and S. L. Brock, *Chem. Mater.*, 2005, **17**, 6644-6650.

45. J. L. Mohanan, I. U. Arachchige and S. L. Brock, *Science* 2005, **307**, 397-400.

46. I. U. Arachchige and S. L. Brock, *J. Am. Chem. Soc.*, 2006, **128**, 7964-7971.

47. Z. Tang, N. A. Kotov and M. Giersig, *Science*, 2002, **297**, 237-240.

48. N. Gaponik, A. Wolf, R. Marx, V. Lesnyak, K. Schilling and A. Eychmueller, *Adv. Mater.* , 2008, **20**, 4257-4262.

49. D. V. Talapin and C. B. Murray, *Science*, 2005, **310**, 86-89.

50. W. Wang, B. Poudel, D. Wang and Z. F. Ren, *Adv. Mater.*, 2005, **17**, 2110-2114.

51. Y. Zhao, J. S. Dyck and C. Burda, *J. Mater. Chem.*, 2011, **21**, 17049-17058.

52. L. Zhang, J. C. Yu, M. Mo, L. Wu, K. W. Kwong and Q. Li, *Small*, 2005, **1**, 349-354.

53. X. Ji, B. Zhang, T. M. Tritt, J. W. Kolis and A. Kumbhar, *J. Electron. Mater.*, 2007, **36**, 721-726.

54. C.-J. Liu, G.-J. Liu, C.-W. Tsao and Y.-J. Huang, *J. Electron. Mater.*, 2009, **38**, 1499-1503.

55. W. Q. Ao, W. A. Sun, J. Q. Li, F. S. Liu and Y. Du, *J. Alloys Compd.*, 2009, **475**, L22-L24.

56. Q. Li, Y. Ding, M. Shao, J. Wu, G. Yu and Y. Qian, *MRS Bull.*, 2003, **38**, 539-543.

57. J.-P. Ge and Y.-D. Li, *J. Mater. Chem.*, 2003, **13**, 911-915.

58. J. J. Urban, D. V. Talapin, E. V. Shevchenko and C. B. Murray, *J. Am. Chem. Soc.*, 2006, **128**, 3248-3255.

59. M. R. Dirmyer, J. Martin, G. S. Nolas, A. Sen and J. V. Badding, *Small*, 2009, **5**, 933-937.

60. A. Purkayastha, S. Kim, D. D. Gandhi, P. G. Ganesan, T. Borca-Tasciuc and G. Ramanath, *Adv. Mater.*, 2006, **18**, 2958-2963.

61. M. Scheele, N. Oeschler, K. Meier, A. Kornowski, C. Klinke and H. Weller, *Adv. Funct. Mater.*, 2009, **19**, 3476-3483.

62. M. Scheele, N. Oeschler, I. Veremchuk, K.-G. Reinsberg, A.-M. Kreuziger, A. Kornowski, J. Broekaert, C. Klinke and H. Weller, *ACS Nano*, 2010, **4**, 4283-4291.

63. W. Kim, J. Zide, A. Gossard, D. Klenov, S. Stemmer, A. Shakouri and A. Majumdar, *Phys. Rev. Lett.*, 2006, **96**, 045901/1-4.

64. D. F. Shriver and M. A. drezdon, *The Manipulation of Air-Sensitive Compounds*, Wiley-Interscience Publication, 1969.

65. B. Fultz and J. M. Howe, *Transmission Electron Microscopy and Diffractometry of Materials*, Springer, 2002.

66. P. A. Webb, C. Orr, *Analytical Methods in Fine Particle Technology*, Micromeritics: Norcross (Georgia), 1997.

67. S. J. Gregg and K. S. W. Sing, *Adsorption, Surface Area, and Porosity 2nd Ed.*, Academic Press, 1982.

68. D. M. Rowe, *Thermoelectric Handbook, Macro to Nano*, CRC Press, 2008.

69. M. Fardy, A. I. Hochbaum, J. Goldberger, M. M. Zhang and P. Yang, *Adv. Mater.*, 2007, **19**, 3047-3051.

70. S. Ganguly and S. L. Brock, *J. Mater. Chem.*, 2011, **21**, 8800-8806.

71. H. Yu and S. L. Brock, *ACS Nano*, 2008, **2**, 1563-1570.

72. Z. H. Dughaish, *Physica B* 2002, **322**, 205-223.

73. R. Kerner, O. Palchik and A. Gedanken, *Chem. Mater.*, 2001, **13**, 1413-1419.

74. Y. Zhao and C. Burda, *ACS Appl. Mater. Interfaces*, 2009, **1**, 1259-1263.

75. Y. Zhao, J. S. Dyck, B. M. Hernandez and C. Burda, *J. Phys. Chem. C*, 2010, **114**, 11607-11613.

76. Q. Yao, Y. Zhu, L. Chen, Z. Sun and X. Chen, *J. Alloys Compd.*, 2009, **481**, 91-95.

77. I. R. Pala, I. U. Arachchige, D. G. Georgiev and S. L. Brock, *Angew Chem. Int. Ed. Engl.*, 2010, **49**, 3661-3665.

78. M. Law, J. M. Luther, Q. Song, B. K. Hughes, C. L. Perkins and A. J. Nozik, *J. Am. Chem. Soc.*, 2008, **130**, 5974-5985.

79. E. Muthuswamy and S. L. Brock, *Chem. Commun.* , 2011, **47**, 12334-12336.

80. S. K. Mishra, S. Satpathy and O. Jepsen, *J. Phys. Condens. Matter*, 1997, **9**, 461-470.

81. S. Ganguly, C. Zhou, D. Morelli, J. Sakamoto, C. Uher and S. L. Brock, *J. Solid State Chem.*, 2011, **184**, 3195-3201.

82. J. P. Fleurial, L. Gailliard, R. Triboulet, H. Scherrer and S. Scherrer, *J. Phys. Chem. Solids*, 1988, **49**, 1237-1247.

83. S. Cho, Y. Kim, A. DiVenere, G. K. Wong, J. B. Ketterson and J. R. Meyer, *Appl. Phys. Lett.*, 1999, **75**, 1401-1403.

84. W. Dong, W. Rhine, G. Caggiano, O. R. Evans, G. Gould, J. White, J. Sharp, P. Gilbert, S. Ganguly and S. L. Brock, *MRS Online Proc. Libr.*, 2011, **1306**, DOI: 10.1557/opl.2011.475

85. B. Poudel, Q. Hao, Y. Ma, Y. Lan, A. Minnich, B. Yu, X. Yan, D. Wang, A. Muto, D. Vashaee, X. Chen, J. Liu, M. S. Dresselhaus, G. Chen and Z. Ren, *Science*, 2008, **320**, 634-638.

86. L. Chen, J. Jiang and X. Shi, *Mater. Res. Soc. Symp. Proc.*, 2004, **793**, 365-373.

87. H.-C. Kim, S.-K. Lee, T.-S. Oh and D.-B. Hyun, *17th Int. Conf. Thermoelectr.*, 1998, 174-177.

88. S. Yoneda, M. Kato and I. J. Ohsugi, *J. Appl. Phys.*, 2010, **107**, 074901/1-6.

89. D. Kusano and Y. Hori, *21st Int. Conf. Thermoelectr.*, 2002, 13-16.

90. T. Plecháček and J. Horák, *J. Solid State Chem.*, 1999, **145**, 197-203.

91. T. Plecháček, J. Navrátil, J. Horák and P. Lošták, *Philos. Mag.*, 2004, **84**, 2217-2228.

92. P.-W. Zhu, Y. Imai, Y. Isoda, Y. Shinohara, X.-P. Jia and G.-T. Zou, *Chin. Phys. Lett.*, 2005, **22**, 2103-2105.

93. S. Bag and M. G. Kanatzidis, *J. Am. Chem. Soc.*, 2010, **132**, 14951-14959.

94. R. Wang, L. Li, I. Arachchige, S. Ganguly, S. L. Brock and G. Mao, *ACS Nano*, 2010, **4**, 6687-6696.

ABSTRACT

SYNTHESIS AND CHARACTERIZATION OF METAL CHALCOGENIDE NANOSTRUCTURED MATERIALS FOR THERMOELECTRIC APPLICATIONS

by

SHREYASHI GANGULY

May 2012

Advisor: Dr. Stephanie L. Brock

Major: Chemistry

Degree: Doctor of Philosophy

The synthesis and characterization of metal chalcogenide nanostructured materials with the potential to exhibit enhanced thermoelectric (TE) properties is reported. The tellurides, specifically PbTe and Bi_2Te_3 (Bi_2Te_3-Sb_2Te_3 alloys) were selected as these are well established TE materials in bulk form. The approaches used for nanostructuring are (1) sol-gel assembly of discrete nanoparticles of PbTe, Bi_2Te_3, and Bi_2Te_3-Sb_2Te_3 alloys, and (2) formation of heterostructured nanocomposites of PbTe nanoparticles in bulk Bi_2Te_3 (p- or n-doped) matrices.

Aerogels and xerogels of PbTe nanoparticles were synthesized by sol-gel assembly of discrete nanoparticles, leading to interconnected networks of nanoparticles and pores. The PbTe aerogel exhibited a high surface area and was more thermally stable to sublimation than the precursor nanoparticles, as indicated by *in-situ* heating experiments in transmission electron microscopy (conducted under vacuum). In contrast, both the nanoparticles and aerogels of PbTe melted at the same temperature as the bulk material, as indicated by differential scanning calorimetry experiments.

The oxidative sol-gel assembly, when employed to thiolate capped Bi_2Te_3 and Bi_2Te_3-Sb_2Te_3 alloy nanoparticles, led to aerogels with similar microscale morphological features to the PbTe aerogel network, but Bi_2Te_3 aerogels were more robust than the PbTe aerogels, yielding self-supporting monoliths. TE property measurement on hot-pressed pellets of Bi_2Te_3 and $Bi_xSb_{2-x}Te_3$ aerogels showed degraded electronic properties (Seebeck coefficient (S), electrical conductivity (σ) and power factor ($S^2\sigma$)) as compared to the nanoparticles, suggesting a doping effect in these materials. The nanoparticles themselves showed degraded electronic properties when compared to the bulk counterparts. In contrast, the lattice thermal conductivities (κ_l) of the nanoparticles and aerogels of Bi_2Te_3 had improved as compared to the bulk counterparts showing that nanostructuring was effective in scattering heat carrying phonons, thereby reducing the κ_l. In contrast, in $Bi_xSb_{2-x}Te_3$, there is little change in k_l, presumably because it is already so low due to the disorder on the cationic lattice. Overall, the degraded electronic properties made the efficiency of these materials (ZT) lower than the bulk counterparts.

Heterostructured nanocomposites of PbTe nanoparticles (different weight %) inside n- or p-doped bulk Bi_2Te_3 matrices were prepared using an incipient wetness impregnation approach. However, the thermoelectric properties of these nanocomposites again indicated a significant doping effect associated with incorporation of PbTe nanoparticles inside the bulk Bi_2Te_3 matrices. This doping effect causes an increase in hole concentration in p-type nanocomposites, leading to a decrease in power factor ($S^2\sigma$) as compared to the bulk p-type matrix, whereas the same doping effect in n-type nanocomposites resulted in compensation of the majority charge carriers (electrons), again resulting in a decrease in power factor ($S^2\sigma$). However, at least for p-type nanocomposites, the lattice thermal conductivities were found to be reduced relative to bulk counterparts, suggesting that incorporation of PbTe nanoparticles does scatter the heat carrying

phonons effectively, reducing the κ_l of the system. The overall lower ZT in these nanocomposites as compared to the bulk counterparts highlights the need for proper optimization of carrier concentration in nanostructured thermoelectrics.

AUTOBIOGRAPHICAL STATEMENT

SHREYASHI GANGULY

Education:

- **August 2006 to February 2012**: Ph.D., Inorganic Chemistry, Wayne State University, Detroit, Michigan, USA. Dissertation: "Synthesis and Characterization of Nanostructured Materials for Thermoelectric Applications". Advisor: Prof. Stephanie L. Brock.
- **July 2004 to July 2006:** Master of Science (M.Sc.) from Indian Institute of Technology (IIT), Roorkee, Uttaranchal, India.
- **July 2001 to July 2004:** Bachelor of Science (B.Sc.) in Chemistry (Hons.) from St. Stephen's College, Delhi, India.

Affiliations and Awards

- Member-American Chemical Society
- Member-Materials Research Society
- Summer Dissertation Fellowship, 2010, Graduate School, Wayne State University, Detroit, Michigan.
- Graduate Teaching Assistant Award, 2008, Wayne State University, Detroit, Michigan.

Presentations:

- Talk**:North American Solid State Conference**, June 2011, Hamilton, Ontario, Canada.
- Poster**: International Conference on Thermoelectrics,** July 2011, Traverse City, Michigan, US.
- Poster**: MRS Fall meeting 2010**, Boston, MA, US.
- Poster**: CORE-Complex Materials Summer 2010 Conference on Complex Materials for Energy Applications , June 2010,** East Lansing, MI, US.
- Poster**: North American Solid State Conference**, June 2009, Columbus, OH, US.
- Poster: **MRS Fall meeting 2008**, Boston, MA, US

Publications

- Wang, R., Li, L., Arachchige, I. U., **Ganguly, S.**, Brock, S. L. and Mao, G., " Nanoparticles change the ordering pattern of n-carboxylic acids into nanorods on HOPG", *ACS Nano*, **2010,** *4*, 6687-6696.
- Dong, W., Rhine, W., Caggiano, G., Evans, O. R., Gould, G., White, J., Sharp, J., Gilbert, P., **Ganguly, S.**, Brock, S. L., " Characterization of bismuth telluride aerogels for thermoelectric applications", *Material Research Society symposium proceedings (2011)*, **2010**, 1306 (Aerogels and Aerogel-Inspired Materials).
- **Ganguly, S.** and Brock, S. L, " Toward nanostructured thermoelectrics: synthesis and characterization of lead telluride gels and aerogels", *J. Mater. Chem.*, **2011**, *21*, 8800-8806.
- **Ganguly, S.**, Zhou, C., Morelli, D., Sakamoto, J., Uher, C. and Brock, S. L., " Synthesis and evaluation of lead telluride/bismuth antimony telluride nanocomposites for thermoelectric applications", *Journal of Solid State Chem.*, **2011**, *12*, 3195-3201.
- **Ganguly, S.**, Zhou, C., Morelli, D., Sakamoto, J., and Brock, S. L., " Synthesis and characterization of porous telluride nanostructures for thermoelectrics applications", manuscript in prepration